



Max-Planck-Institut für Festkörperforschung

**Oxidation Kinetics of Metal Films and
Diffusion in NiO for Data Storage**

Yeliz Unutulmazsoy

Dissertation
an der
Universität Stuttgart

Oxidation Kinetics of Metal Films and Diffusion in NiO for Data Storage

Von der Fakultät Chemie der Universität Stuttgart
zur Erlangung der Würde eines

Doktors der Naturwissenschaften
(Dr. rer. nat.) genehmigte Abhandlung

Vorgelegt von

Yeliz Unutulmazsoy

aus Susehri, Türkei

Hauptberichter:	Prof. Dr. Joachim Maier
Mitberichter:	Prof. Dr. Anke Weidenkaff
Prüfungsvorsitzender:	Prof. Dr. Rainer Niewa

Tag der Einreichung: 31.03.2016

Tag der mündlichen Prüfung: 08.06.2016

Max-Planck-Institut für Festkörperforschung

Stuttgart

2016

Erklärung über die Eigenständigkeit der Dissertation

Ich versichere, dass ich die vorliegende Arbeit mit dem Titel *Oxidation Kinetics of Metal Films and Diffusion in NiO for Data Storage* selbständig verfasst und keine anderen als die angegebenen Quellen und Hilfsmittel benutzt habe; aus fremden Quellen entnommene Passagen und Gedanken sind als solche kenntlich gemacht.

Declaration of Authorship

I hereby certify that the dissertation entitled *Oxidation Kinetics of Metal Films and Diffusion in NiO for Data Storage* is entirely my own work except where otherwise indicated. Passages and ideas from other sources have been clearly indicated.

Name/Name: Yeliz Unutulmazsoy

Unterschrift/Signed: _____

Datum/Date: 31.03.2016

To my family.

Content

Content	xiii
Zusammenfassung	i
Abstract	v
1. Introduction	1
1.1. Motivation – Irreversible Data Storage	2
2. Theoretical Background	9
2.1. Defect Chemistry of NiO	9
2.1.1. Defect Equilibrium of Undoped and Doped-NiO	9
2.1.2. Chemical Diffusion Coefficient and Conductivity of Undoped and Doped NiO	15
2.1.3. Tracer Diffusion Coefficient of Ni in NiO	20
2.2. Oxidation Kinetics of Metals	21
2.2.1. Wagner Theory of Oxidation	22
2.2.2. Cabrera - Mott Theory of Oxidation	25
2.2.3. Surface Reaction Controlled Oxidation	28
3. Experimental Methods	29
3.1. <i>In-situ</i> Oxidation Measurements of Metal Films	29
3.1.1. Sample preparation	29
3.1.2. Electrochemical Impedance Spectroscopy (EIS)	31
3.1.3. Experimental Conditions	32
3.1.4. Experimental Set-Up	32
3.2. Conductivity Relaxation Measurements (ECR)	35
3.2.1. Sample Preparation	35
3.2.2. Conductivity Measurements	39
3.3. Sample Characterization	41
3.3.1. Inductively Coupled Plasma-Optical Emission Spectroscopy (ICP-OES)	41
3.3.2. X-Ray Diffraction (XRD)	41
3.3.3. X-Ray Photoelectron Spectroscopy (XPS)	41

3.3.4. SEM-FIB-TEM/EDX	42
3.3.5. Raman Spectroscopy	43
4. Results and Discussion.....	45
4.1. Oxidation Kinetics of Metal Films.....	45
4.1.1. Oxidation Kinetics of Different Metal Films	47
4.1.2. Oxidation Kinetics of Nickel at Different Conditions.....	51
4.1.3. Literature on Cation Diffusion in Oxides	53
4.1.4. Grain Size Effect on Oxidation Rate & Diffusion.....	56
4.2. Oxidation Kinetics of Cr-doped Ni films.....	62
4.2.1. Oxidation Kinetics of e-Beam Evaporated Cr-doped Ni Films.....	62
4.2.2. Oxidation Kinetics of Magnetron Sputtered Cr-doped Ni films	66
4.2.3. Oxidation Kinetics of PLD Grown Cr-doped Ni films.....	67
4.2.4. Concluding Discussion on the Ni Film Oxidation.....	69
4.3. Chemical Diffusion Coefficient of Undoped and Cr-doped NiO Ceramics (Conductivity Relaxation Measurements).....	71
4.3.1. XRD Analyses of Undoped and Cr-doped NiO Ceramics	71
4.3.2. Grain Boundary Blocking Effect.....	74
4.3.3. Partial Pressure and Temperature Dependence of σ and D^δ	75
4.3.4. Donor Dopant Concentration Effect.....	83
4.3.5. Literature on Conductivity & Chemical Diffusion Coefficient.....	85
4.3.6. Raman Spectroscopy on Pellets and Powders	89
4.3.7. TEM/EDX Analysis on Pellets.....	93
4.3.8. Concluding Discussion on the Chemical Diffusion Coefficient of NiO	97
5. Summary and Conclusions	101
Appendix.....	105
Symbols and Abbreviations	113
References	117
Acknowledgements	125
Curriculum vitae.....	127

Zusammenfassung

Das Wachstum porenfreier Oxidschichten auf Metallen wird durch die Bildung und Wanderung von Punktdefekten bestimmt und ist daher eine Frage von fundamentaler Bedeutung. Bisher wurde in der Literatur die Oxidationskinetik von dicken Metallschichten, Einkristallen und polykristallinen Proben untersucht. Die Oxidation dünner Metallschichten auf isolierenden Substraten kann durch Messung der Leitfähigkeit des verbleibenden Metalls leicht verfolgt werden. Diese Dissertation konzentriert sich darauf, die Prozesse zu verstehen, welche die Wachstumsrate des Oxids bestimmen (entweder Oberflächenkinetik oder chemische Diffusion), und versucht des Weiteren, die Wachstumsrate im Hinblick auf potentielle Anwendungen in der irreversiblen Datenspeicherung zu erhöhen.

In der vorliegenden Arbeit wurde die Änderung des Widerstands dünner Metallfilme auf Al_2O_3 -Substraten während der Oxidation mittels elektrischer Impedanzspektroskopie gemessen und die Oxidschichtdicke berechnet. Das Oxidwachstum folgt einem parabolischen Geschwindigkeitsgesetz für Cr, Al, Ti, V, Zn, Ni und Co-Filme mit einer typischen Dicke von 10 bis 150 nm. Daher ist der die Kinetik bestimmende Prozess, trotz der geringen Schichtdicken, die Diffusion durch die Oxidschicht wie von Wagner beschrieben. Ni und Co zeigen eine höhere Wachstumsrate des Oxids als Cr, Al, Ti, V und Zn. Die Geschwindigkeitskonstante von Ni wird durch Variation der äußeren Bedingungen wie $p\text{O}_2$, UV-Einstrahlung, Einwirkung von Ozon und Variation der Schichtdicke nicht wesentlich beeinflusst. Dies bestätigt die Gültigkeit des parabolischen Geschwindigkeitsgesetzes für Proben mit einer Dicke von 100 bis 150 nm im Temperaturbereich von 250-500 °C. Ein Vergleich der Literaturwerte von Ni-

Tracerdiffusionskoeffizienten zwischen einkristallinem und polykristallinem NiO und der Werte der vorliegenden Arbeit zeigt, dass eine Verringerung der Korngröße den effektiven Diffusionskoeffizienten um Größenordnungen erhöht, was auf schnelle Diffusion von Ni entlang der Korngrenzen in NiO schließen lässt.

NiO wurde als Beispiel für eine detailliertere Untersuchung der Oxidationskinetik und Diffusion ausgewählt. Die Diffusion von Ni in NiO wird hauptsächlich durch Ni-Fehlstellen bestimmt und diese Fehlstellen werden im intrinsischen Material durch Elektronenfehlstellen kompensiert. Daher wäre zu erwarten, dass die Dotierung von NiO mit Donatoren (z.B. mit Al^{3+} , Cr^{3+} , etc.) die Reaktionsrate erhöht, indem die Ni-Fehlstellenkonzentration erhöht wird. Jedoch zeigte die Oxidationsrate Cr-dotierter Ni-Filme mit verschiedener Dicke und verschiedener Cr-Konzentration (0.1 und 1 %) keinen signifikanten Unterschied zu undotiertem Ni. Tiefenprofile der Cr-Konzentration in Cr-dotierten Ni-Filmen vor und nach der Oxidation wurden mit XPS gemessen. Die Ergebnisse ließen darauf schließen, dass Cr nicht homogen in den Filmen verteilt war. Während im Metall eine chromreiche Schicht an der Oberfläche und eine fast homogene Verteilung von Cr über den Rest der Probe vorliegt, verblieb im Oxid der Großteil des Cr an der Grenzfläche zum Substrat. Daher verhinderte die inhomogene Verteilung von Cr im wachsenden Oxidfilm eine schnellere Oxidation.

Da es schwierig ist, die Korngröße gezielt zu verringern und eine homogene Verteilung der Donatoren im wachsenden Oxidfilmen zu erreichen, wurden die Transporteigenschaften von undotierten und Donator-dotierten keramischen NiO-Proben mittels Leitfähigkeitsrelaxations-Messungen untersucht. NiO-Pulver wurden mit Nitrat-Glyzin-Methode hergestellt und mittels Spark Plasma Sintering zu dichten keramischen Proben kompaktiert. Die Korngröße der keramischen Proben wurde durch weiteres Tempern eingestellt. Leitfähigkeit (σ) und chemischer Diffusionskoeffizient (D^δ) wurden in Abhängigkeit des Sauerstoffpartialdrucks und der Temperatur bestimmt. Es zeigte sich, dass diese Werte in nichttrivialer Weise vom Cr-Anteil (0.1, 0.3 und 1 %), der Korngröße und der thermischen Vorgeschichte abhingen. Der Vergleich von σ und D^δ zwischen

unbehandelten (Heißpressen für 5 min bei 1000 °C) und getemperten (8h bei 1500 °C) Proben zeigt, dass die Cr-Donatoren in den unbehandelten Keramiken elektrochemisch inaktiv sind. Für die getemperten Proben zeigte 0.1 % Cr-dotiertes NiO einen signifikanten Abfall von σ und Anstieg von D^δ im Vergleich zu undotiertem NiO, was auf aktivierte Donatoren hinweist. Jedoch bewirkte eine weitere Erhöhung des Cr-Anteils eine Verringerung des chemischen Diffusionskoeffizienten für getemperte Proben. Die inhomogene Verteilung von Cr und Bildung unerwünschten NiCr₂O₄-Spinels wurde mittels TEM/EDX an Korngrenzen in nahezu allen Proben nachgewiesen, für hohe Konzentrationen von Cr sogar im Korninneren. Die gemessenen Leitfähigkeiten und chemischen Diffusionskoeffizienten weisen auf eine weit geringere Löslichkeit von Cr als bisher in der Literatur bekannt hin. Die höchste erreichbare Erhöhung des chemischen Diffusionskoeffizienten durch Dotierung mit Donatoren beträgt mehr als eine Größenordnung bei 700 °C.

In-situ-Messungen der Oxidationskinetik von Metallen zeigten, dass Co die höchste Reaktionsrate der untersuchten Metalle aufweist; Extrapolation ergibt eine Oxidationszeit von Millisekunden bei einer moderaten Temperatur von 540 °C. Die Dünnschichten zeigen ebenfalls eine wesentlich höhere Oxidationsrate als die Literaturwerte aufgrund ihrer sehr kleinen Korngrößen. Die Oxidationsrate ist jedoch trotzdem nicht im erwünschten Bereich für Anwendungen zur routinemäßigen langfristigen Datenspeicherung, für welche eine Oxidationszeit von Mikrosekunden notwendig ist. Nichtsdestoweniger könnten Co-Dünnschichten wegen der äußerst geringen Oxidationsrate bei Raumtemperatur für besondere Einsatzgebiete zur irreversiblen Datenspeicherung eingesetzt werden.

Abstract

The growth of pore-free oxide layers on metals is determined by formation and migration of point defects and thus is an issue of fundamental importance. So far, mainly oxidation kinetics of thick metal films, crystals, and bulk samples were investigated in the literature. The oxidation of thin metal films on insulating substrates can easily be monitored by measuring the conductivity of the remaining metal. This dissertation focuses on understanding the processes that determine the oxide growth rate (*e.g.*, surface reaction or chemical diffusion) in thin films, and also attempts to increase the reaction rate constant for potential applications in irreversible data storage systems.

In this work, the resistance changes upon oxidation were measured by electrical impedance spectroscopy during the oxidation of metal films on Al₂O₃ substrates, and the oxide thicknesses were calculated. The oxide growth follows the parabolic rate law of oxidation for Cr, Al, Ti, V, Zn, Ni and Co films with a thickness typically ranging from 10 to 150 nm. Thus, in spite of their small thicknesses, the rate determining process of the oxidation of these metal films is found to be diffusion through the oxide layer according to the Wagner theory. Ni and Co exhibit a higher oxide growth rate than Cr, Al, Ti, V, and Zn. The oxidation rate constant of Ni is not significantly changed by applying different conditions such as different pO_2 , UV illumination, ozone exposure, and varying metal film thickness. This confirms the validity of the parabolic rate law of oxidation for the samples with 10-150 nm thickness in the temperature range of 250-500 °C. A comparison of Ni tracer diffusion coefficients between single- and polycrystalline NiO from literature studies and the present work with polycrystalline films (grain size: 10-30 nm) shows that a

decreased grain size increases the effective diffusion coefficient by orders of magnitude pointing towards fast Ni diffusion along the grain boundaries in NiO.

NiO was chosen as an example for a more detailed investigation of oxidation kinetics and diffusion. Ni diffusion in NiO is mainly controlled by Ni vacancies, and the vacancies are compensated by electron holes in undoped NiO. Thus, donor doping of NiO (*e.g.*, with Al^{3+} , Cr^{3+} , etc.) is expected to increase the reaction rate constant by increasing the Ni vacancy concentration. However, the oxidation rate constant of Cr-doped Ni films with different thicknesses and different Cr concentrations (0.1 and 1 %) showed no significant change compared to undoped NiO. Depth profiles of Cr concentration in Cr-doped Ni films before and after oxidation were obtained by X-ray photoelectron spectroscopy (XPS). The results indicated that Cr was not homogeneously distributed in the films. While there is a Cr-rich surface layer in the metal form and almost homogenous distribution of Cr over the rest of the metal film, in the oxide form of the sample most of the Cr remained at the interface of the oxide and the substrate. Therefore the inhomogeneous Cr distribution in the growing oxide film prevented a faster oxidation.

Since it is difficult to precisely control the grain size and to obtain a homogenous dopant distribution in the growing oxide films, the transport properties of undoped and donor-doped NiO ceramic samples were studied by conductivity relaxation measurements. NiO powders were synthesized by nitrate-glycine synthesis method and compacted to dense ceramic samples by spark plasma sintering (SPS). The grain size of the ceramic samples was controlled by additional annealing. Conductivity (σ) and chemical diffusion coefficient (D^δ) values were obtained as a function of oxygen partial pressure and temperature. These values were found to depend in a nontrivial way on Cr content (0.1, 0.3 and 1 %), grain size and thermal history of the samples. The comparison of σ and D^δ values of as-prepared (SPS, 5 min at 1000 °C) and annealed (8 h at 1500 °C) samples showed that the Cr dopants seem to be electrochemically inactive for the as-prepared ceramics. For annealed samples, 0.1 % Cr-doped NiO showed a significant decrease in σ and increase in D^δ compared to undoped NiO, indicating that the dopants are activated. However, a further increase in Cr content

caused a decrease in chemical diffusion coefficient for annealed samples. The reason for this unexpected behavior is an inhomogeneous Cr distribution in the samples. The inhomogeneous Cr distribution and formation of undesired NiCr_2O_4 spinel is detected by transmission electron microscopy/energy dispersive X-ray spectroscopy (TEM/EDX) at grain boundaries for almost all samples, and for high Cr concentrations even in the grains. The obtained conductivities and chemical diffusion coefficients indicate a much lower solubility limit for Cr than reported in the literature. The maximum achievable increase of the chemical diffusion coefficient by donor doping is more than one order of magnitude at 700 °C.

In-situ oxidation kinetics measurements of metals revealed that Co films show the highest reaction rate constants within the studied metals; extrapolation yields a millisecond oxidation time at a temperature of 540 °C. The thin films in this study also showed much higher oxidation rate constant than the literature values because of their very small grain size. However, the oxidation rate constant is still not in the desired range for a routine long-term data storage application, which requires microsecond oxidation time. Nonetheless, for special purposes, Co thin films could be candidates for a long-time data archiving system owing to the very low oxidation rate constants at room temperature.

1. Introduction

The oxidation kinetics of metals was studied intensively in the literature [1-8] not only for pure metals but also for alloys. In the literature, great attention was paid to avoiding metal corrosion for engineering purposes for high-temperature applications [9]. To test corrosion resistant metals and alloys, the studies were mostly performed on thick metal films or bulk samples at relatively high temperatures (>500 °C). However, there are only limited studies on thin film oxidation kinetics [3, 10, 11]. During the present work, the oxidation kinetics of thin films is systematically studied for 10 to 150 nm films between 200 and 500 °C for different metals (mostly transition metals) and different experimental conditions (*e.g.*, under UV illumination, different oxygen partial pressures). The main interest in this work is to understand the processes that limit the growth of dense oxide layers (*e.g.*, surface reaction or diffusion), and also to increase the reaction rate constant for potential long-term data storage applications (data archiving materials). A high corrosion resistance is required for data-archiving materials. This is found in oxides such as Cr_2O_3 , Al_2O_3 , TiO_2 , CoO , NiO which form dense and well-adhering oxide layers on the metals, and at the same time, they are chemically stable. For these reasons, NiO has a particular attention both in literature and in this work.

The goals of this research are: (i) to understand the transport processes in the growing oxide films by thermal oxidation, (ii) to search for possibilities to control the growth rate of the films, (iii) to understand the transport properties in oxide-ceramics samples and (iv) to modify the defect concentrations of the films and ceramics for enhanced diffusion with the

objective of finding a chemically stable data storage material. Desired long-term data storage materials require not only fast oxidation at moderately elevated temperatures (~500 to 600 °C) but also high corrosion resistance at room temperature. This study is distinct from literature because oxidation kinetics of thin metal films is studied for a relatively low-temperature range (<500 °C), and attempts were made to increase the oxidation rate constant of thin films by donor-doping.

1.1. Motivation – Irreversible Data Storage

Data storage technology is well-developed in terms of high storage capacity and fast-read/write options, but still, has limitations for data durability. The meaning of data durability here is the stability and the protection of digitally stored data for a very long time such as 1000 years. Today's common digital data durability is limited to a maximum of 50 years. The question "*How digitally stored data can be protected for more than a thousand of years?*" brings to the mind "*irreversible structures*" or in other words "*stable oxides*". If digital data can be stored on a stable material such as binary oxides/corrosion resistant metals, then such a system can provide "*digital libraries*" for the future generations.

There are three basic technologies available for storing digital information: magnetic, solid state, and optical data storage. The most common failure of these materials is due to degradation with time because of chemical reactions such as corrosion, oxidation, and breaking of chemical bonds [12, 13]. The failures are accelerated at elevated temperatures, humidity, and UV light [12, 13]. For common available technologies (see Table 1.1), the life expectancy of a magnetic tape is maximum 50 years which is rarely attainable. Therefore rather than the maximum limits, the lower limits of data storage materials are important. One of the studies [14] showed that magnetization decreases dramatically because of environmental conditions such as elevated temperatures (*e.g.*, from 30 to 60 °C) and humidity (*e.g.*, from 20 % to 50 %). Delamination of the recording layer is another reason of data loss in magnetic data storage materials [13]. Also, optical discs are very sensitive to light because the data recording material "dye" is photosensitive [12]. Therefore, paper is still an appealing data-storage material with the life expectancy of at

least several centuries, if produced and stored in good conditions. Even alkaline paper has a life expectancy of over a 1000 years at best, and 500 years for average qualities [15].

Table 1.1: Life expectancy of data storage materials for common available technology and some exceptions. The table is taken from reference [12] and modified.

data storage material	life expectancy (year)
magnetic tape	10-50
magnetic hard disc drives	1-7
flash drives and solid state drives	10-12
recordable optical disc	1-25
Delin Devices-Archival Gold Disc	300
Milleniata - M-DISC™	~1000 (advertised)
Hitachi - silica glass	2.5 million
this work - thin metal/oxide compound	~1000

Today's data density and data-writing/reading speeds are already much higher than what a standard user usually needs. However, the durability of the digitally stored data is a key question for a further development. There are several inventions on long-term data storage materials for which researchers claimed that it is possible to keep the data from 100 to 300 years [16], 1000 years [17] and even around several hundred million years [18]. Milleniata and Hitachi claimed that the recorded data on the disc survives for a very long time under elevated environmental conditions, thus these two inventions are particularly important.

Archival Gold Discs offer a life expectancy of 100, 200 and 300 years for different products by using protective coatings on the disc surfaces such as sputtered gold to prevent oxidation and data degradation, or polymer hard coatings to avoid scratches and stains [16]. When the lifetime increases from 100 years to 300 years, the disc capacity decreases from 4.7 GB to 700 MB, respectively [16]. Unfortunately available information on Archival Gold Discs is limited.

Hitachi has developed a long-term data storage material using fused silica glass which is known to have excellent heat and water resistance [18]. The data is recorded on the silica glass by creating altered regions (dots) by changing the refractive index of the laser-focused area. By using 4 layers of data recording by femtosecond laser, Hitachi could obtain a compact disc data density of about 35 MB/inch² and the data reading is possible via using an optical microscope with LED light [18, 19]. It is claimed that the data can still be read even after heating the material for 2 hours at 1000 °C [18]. Lately, the company released that they could increase the data density by 100 layers of data recording on fused silica glass [20]. Although the data on fused silica glass can last for a million years under drastic environmental conditions, data recording requires ultrahigh light intensity (*e.g.*, 8×10^{14} W/cm²) [21, 22]. Since data recording requires very high laser power which is not practical for the end user, there is no Hitachi product in the market that can serve as a long-time data archiving material.

Milleniata has developed a commercially available disc (M-DISC™) which is claimed to endure for 1000 years in extreme environmental conditions. It has a capacity of 4.77 GB and relatively low data-writing speed (5.28 MB/s) [17]. Milleniata uses an inorganic-composite data recording layer instead of an organic dye. Although the data on Milleniata's disc is readable by a regular DVD-reader, the end user needs an external data writer to record because a high power laser is required to burn the inorganic-composite layer. The M-DISC™ data recording layer consists of a multilayer structure which has mainly inorganic materials such as metal oxides, metals, and also contains some silicon oxides and rare-earth metals [23]. The layer is solid up to 500 °C and stable against oxygen, water, and other corrosive chemicals. The layer undergoes a permanent physical change during the writing process by a high-power laser. The generated heat of the focused laser causes the innermost layers to melt and creates a hole in the data layer [23]. The material surrounding the written voids forms a polycrystalline structure.

Present Thesis

Although these inventions offer relative long times for reliable data storage, the main principles are complex. In this dissertation the approach for data archiving materials is very simple: storing a bit in a spot by laser oxidation of a corrosion resistant metal which requires only one starting material. This simple starting material needs to be oxidized very fast to overcome slow data writing issue. For these reasons, one should understand the fundamentals of oxidation kinetics of thin metal films and control the oxidation kinetics to achieve the requirements. For this purpose, during this research: the oxidation kinetics of thin metal films is investigated, rate determining steps are attempted to change from diffusion to surface reaction, donor doping is used to obtain a faster oxidation, and transport properties of thin films and ceramic samples are studied for undoped and Cr-doped NiO.

Thus this dissertation is motivated by the search for *a possible data-archiving material* using thin metal film oxidation. The desired solution for a long-term data storage material is the fast and local oxidation of the corrosion resistant metal at moderate temperatures (which could be applied in a regular computer). The chosen corrosion resistant metal and its oxide form should be stable for at least 1000 years, once the data is written. Reading the data, stored by local oxidation of a thin metal film, can be easy, either by using optical reading techniques (*e.g.*, reflectivity difference of oxide and metal) or by measuring the resistance of these two different structures. In order to obtain stability for more than 1000 years and to have a data writing speed (oxidation time) of order nanoseconds, the oxidation rate constant of the metal should be around 10^{-4} cm²/s at 627 °C and 10^{-22} cm²/s at 25 °C, as illustrated in Figure 1.1. This means that the activation energy of the oxidation should be at least 1.6 eV.

The analysis of the oxidation experiments in this work made clear that CoO and NiO are the candidates for which the requirements for data archiving are within realistic reach. For instance, for a 10 nm Co thin film, millisecond oxidation time constant could be extrapolated at 540 °C which corresponds roughly to kB/s data writing speed. Although it is not fast enough for routine data storage, Co films might be candidates for data archiving via “thin film oxidation”, for specific purposes.

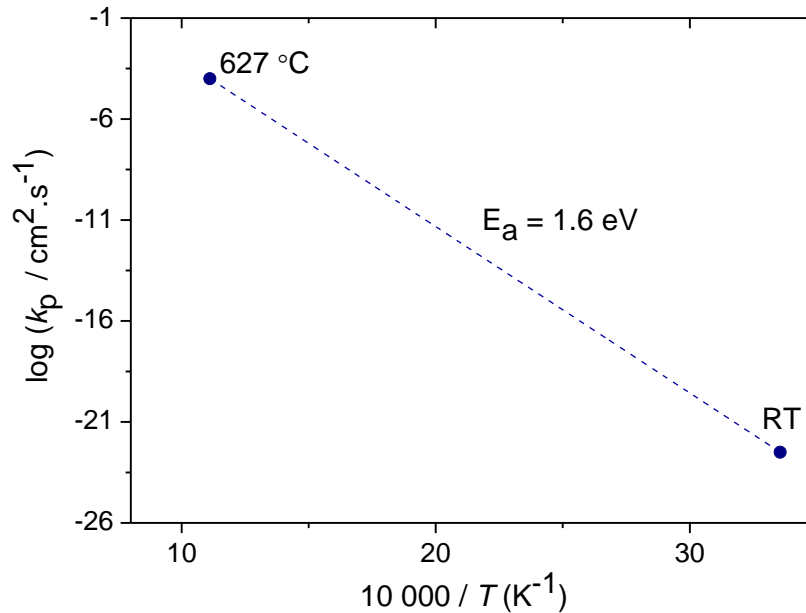


Figure 1.1: Oxidation rate constants and activation energy required for the desired long-term data storage material at 25 °C and at 627 °C to obtain stable structures for ≥ 1000 years.

Driven to find the desired data storage material the following steps are undertaken in the current thesis: (i) the oxidation kinetics of different thin metal films is investigated at relatively low temperatures for different thicknesses, (ii) attempts are made to increase the oxidation rate constant of the metal films by appropriate doping, and (iii) ceramic oxide samples (NiO) are studied to understand the transport properties and doping effects in bulk oxides in detail. Although creating a data spot on a metal film requires local oxidation by a laser for application purposes, for the fundamental research, the thermal oxidation of the entire film is studied.

This thesis is presented in the following way: (i) brief information on defect chemistry and transport properties of NiO, oxidation phenomena and theories on oxidation kinetics for thin metal films are given in the section of theoretical background, (ii) principles of experiments, sample preparation and analysis techniques are explained for thin films and for bulk samples in the section of experimental methods, (iii) the main results and understanding on oxidation kinetics of thin films and transport properties of NiO ceramic

samples are presented with a concluding discussions individually in the section of results and discussion, and finally (iv) the research is summarized and concluded in the last section.

2. Theoretical Background

2.1. Defect Chemistry of NiO

2.1.1. Defect Equilibrium of Undoped and Doped-NiO

2.1.1.1. Undoped NiO

Nickel oxide is a metal-deficient p-type semiconductor with a small deviation from stoichiometry ($\text{Ni}_{1-\delta}\text{O}$). It is thermodynamically stable in a large temperature (T) and oxygen partial pressure ($p\text{O}_2$) range [24]. It is well known from the previous studies that nickel vacancies and electron holes (h^\bullet) are predominant defects, but the ionization degree of nickel vacancies is still unclear [24]. The ratio of the vacancies might depend on conditions such as T and $p\text{O}_2$. According to reference [25] doubly ionized vacancies are mostly present at relatively high temperatures and low $p\text{O}_2$, while singly ionized vacancies are predominant at low temperatures and high $p\text{O}_2$.

The reaction for the incorporation of oxygen from the gas phase into the lattice is:



where the Kröger-Vink notation [26] is used. In this notation the type of defect is represented by a major symbol (*e.g.*, V: vacancy), the site is indicated by a subscript (*e.g.*, O_o or V_{Ni}) and the relative charge of defects is indicated by a superscript (negative charge: \prime and positive charge: \bullet). In Eq. 1, O_o^\times represents an oxygen ion on its regular lattice site, α is the ionization degree of nickel vacancies (either 1 or 2), $V_{\text{Ni}}^{\prime\alpha}$ is a nickel vacancy on a nickel site which can be singly or doubly ionized (V_{Ni}^\prime or $V_{\text{Ni}}^{\prime\prime}$).

According to the mass action law for the nickel vacancy formation reaction, the mass action constant (K) is written

$$K = \frac{[V_{Ni}^{\alpha'}][h^{\bullet}]^{\alpha}}{\sqrt{pO_2}} = \exp\left(-\frac{\Delta H^{\circ}}{kT} + \frac{\Delta S^{\circ}}{k}\right) \quad (2)$$

where k is the Boltzmann constant, and ΔH° and ΔS° are the standard reaction enthalpy and entropy, respectively. Square brackets represent the concentration of the related species (molar fraction; number of defects per NiO formula unit). Since the nickel vacancies are compensated by the electron holes in NiO (intrinsic case), the electroneutrality condition is

$$\alpha[V_{Ni}^{\alpha'}] = [h^{\bullet}] \quad (3).$$

As there is an ambiguity with respect to the ionization degree of Ni vacancies in prior studies, here both possibilities are considered. When doubly ionized nickel vacancies are the majority defects in NiO ($[V_{Ni}^{\prime\prime}] > [V_{Ni}^{\prime}]$), one obtains



$$K_1 = \frac{[V_{Ni}^{\prime\prime}][h^{\bullet}]^2}{\sqrt{pO_2}} = \exp\left(-\frac{\Delta H_1^{\circ}}{kT} + \frac{\Delta S_1^{\circ}}{k}\right) \quad (5)$$

with the electroneutrality condition

$$2[V_{Ni}^{\prime\prime}] = [h^{\bullet}] \quad (6).$$

Inserting Eq. 6 into 5 yields the hole concentration

$$[h^{\bullet}] = 2^{1/3} K_1^{1/3} pO_2^{1/6} \quad (7).$$

For the case of singly ionized nickel vacancies compensated by electron holes in NiO, the expressions are



$$K_2 = \frac{[V'_{Ni}][h^\bullet]}{\sqrt{pO_2}} = \exp\left(-\frac{\Delta H_2^0}{kT} + \frac{\Delta S_2^0}{k}\right) \quad (9)$$

$$[V'_{Ni}] = [h^\bullet] \quad (10)$$

leading to

$$[h^\bullet] = K_2^{1/2} pO_2^{1/4} \quad (11).$$

The nickel vacancy concentrations can be easily calculated through the electroneutrality conditions by using the hole concentrations.

2.1.1.2. Donor-doped NiO

Doping of the metal oxide is an important tool to change point defect concentrations significantly. When the Ni site is substituted by a trivalent cation such as Cr^{3+} , Al^{3+} , Fe^{3+} in NiO, the defect D^\bullet_{Ni} (donor dopant) has an effective single positive charge which increases the nickel vacancy concentration by modifying the electroneutrality condition:

$$\alpha[V_{Ni}^{\alpha}] = [h^\bullet] + [D^\bullet_{Ni}] \quad (12)$$

where $[D^\bullet_{Ni}]$ represents donor concentration. When $[D^\bullet_{Ni}]$ largely exceeds $[h^\bullet]$, the electroneutrality condition yields $\alpha[V_{Ni}^{\alpha}] = [D^\bullet_{Ni}]$ and the mass action constant is

$$K = \frac{[D^\bullet_{Ni}][h^\bullet]^\alpha}{\sqrt{pO_2}} = \exp\left(-\frac{\Delta H^\circ}{kT} + \frac{\Delta S^\circ}{k}\right) \quad (13).$$

Therefore, the electroneutrality condition for doubly ionized nickel vacancies

$$2[V''_{Ni}] = [D^\bullet_{Ni}] \quad (14)$$

and

$$K_1 = \frac{[D^\bullet_{Ni}][h^\bullet]^2}{2\sqrt{pO_2}} \quad (15)$$

$$[h^\bullet] = 2^{1/2} K_1^{1/2} \frac{pO_2^{1/4}}{[D_{Ni}^\bullet]^{1/2}} \quad (16)$$

are obtained. If it is assumed that singly ionized vacancies are the predominant defects, then the expressions

$$[V'_{Ni}] = [D_{Ni}^\bullet] \quad (17)$$

$$K_2 = \frac{[D_{Ni}^\bullet][h^\bullet]}{\sqrt{pO_2}} \quad (18)$$

$$[h^\bullet] = K_2 \frac{pO_2^{1/2}}{[D_{Ni}^\bullet]} \quad (19)$$

are obtained.

2.1.1.3. Acceptor doped NiO

Acceptor doping in NiO (*e.g.*, K^+ , Li^+ on a Ni^{2+} site) changes the electroneutrality condition to $[A'_{Ni}] + \alpha[V_{Ni}^{\alpha'}] = [h^\bullet]$ and thus increases the hole concentration. For $[A'_{Ni}] \approx [h^\bullet] > \alpha[V_{Ni}^{\alpha'}]$, the mass action constant is

$$K = \frac{[A'_{Ni}]^\alpha [V_{Ni}^{\alpha'}]}{\sqrt{pO_2}} = \exp\left(-\frac{\Delta H^\circ}{kT} + \frac{\Delta S^\circ}{k}\right) \quad (20)$$

where A'_{Ni} represents the acceptor dopant. For doubly and singly ionized vacancies, this yields

$$K_1 = \frac{[A'_{Ni}]^2 [V_{Ni}^{\alpha'}]}{\sqrt{pO_2}} \quad (21)$$

$$K_2 = \frac{[A'_{Ni}] [V_{Ni}^{\alpha'}]}{\sqrt{pO_2}} \quad (22).$$

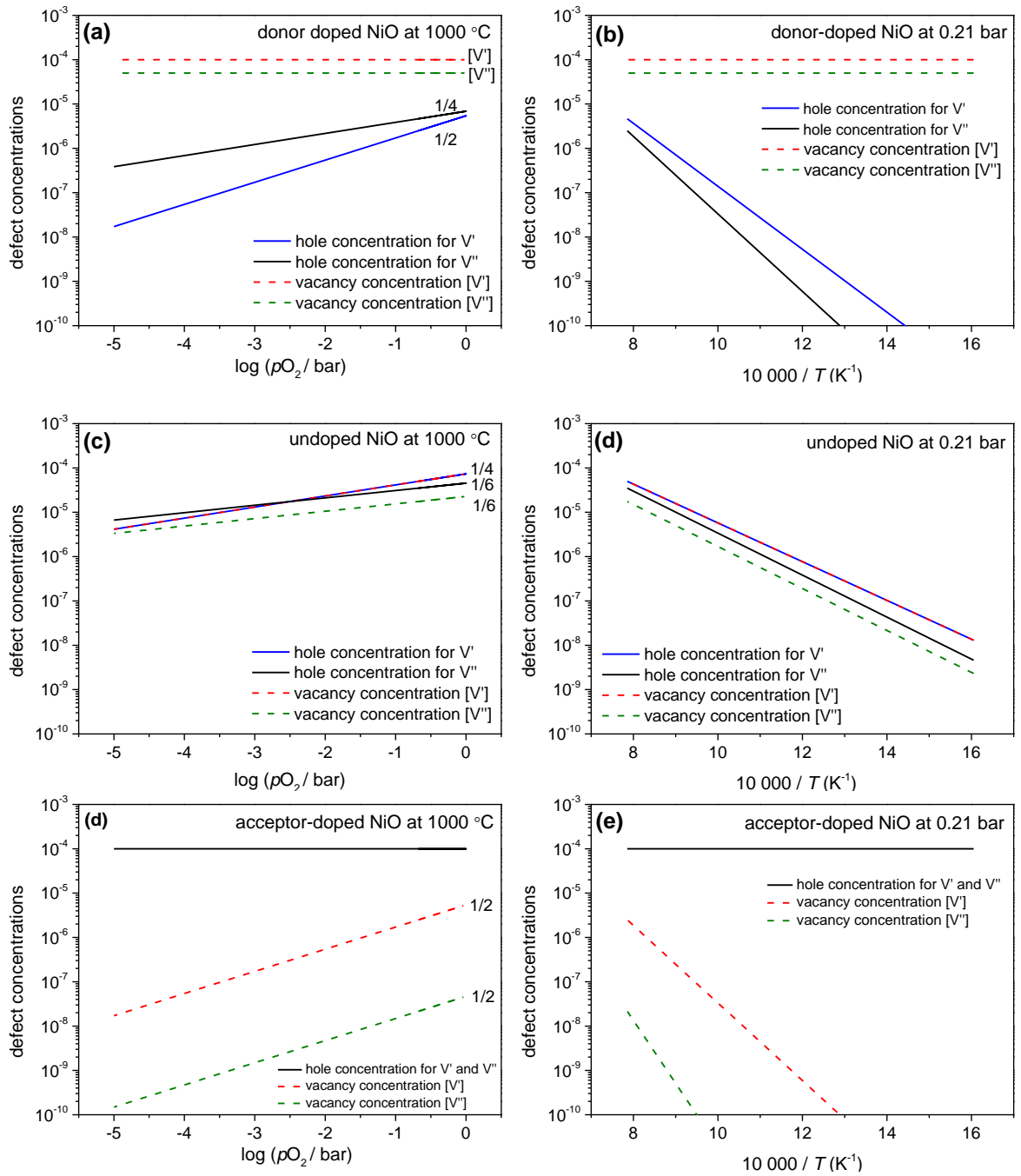


Figure 2.1: pO_2 (at 1000 °C) and temperature (at 0.21 bar) dependences of the vacancy and hole concentrations in NiO. (a) and (b) for donor-doped NiO ($[D_{Ni}^{\bullet}] = 10^{-4}$), (c) and (d) for undoped NiO, (e) and (f) for acceptor-doped NiO ($[A'_{Ni}] = 10^{-4}$). The thermodynamic data of Koel and Gellings [27] were used for the calculations of the related defects. Unit of defect concentration is the molar fraction (number of defects per NiO formula unit).

The results of Koel and Gellings [27] were used to calculate the defect concentrations in NiO (for doubly ionized vacancies: $\Delta H^\circ = 272 \text{ kJ}\cdot\text{K}^{-1}\cdot\text{mol}^{-1}$, and $\Delta S^\circ = -41.4 \text{ J}\cdot\text{K}^{-1}\cdot\text{mol}^{-1}$). Figure 2.1 shows the temperature (at 0.21 bar) and the $p\text{O}_2$ (at 1000 °C) dependence of the vacancies (for the cases of V'_{Ni} or V''_{Ni} being the predominant defect) and the hole concentrations for undoped, donor-doped, and acceptor doped NiO.

As explained above, the defect concentrations can be modified by doping. When the defects are not fixed by the dopant, they are $p\text{O}_2$ dependent. The exponent of the $p\text{O}_2$ dependence differs according to predominant defect type (V'_{Ni} or V''_{Ni}) and dopant type (donor or acceptor). The defect concentrations increase by increasing temperature, $p\text{O}_2$ and dopant concentration. Some of this information can be easily seen in Figure 2.1. Also, $p\text{O}_2$ dependences of defects are indicated in Figure 2.1, which are already seen in the mass action constants (Equation 5, 9, 15, 18, 21, and 22). While nickel vacancy concentration is increased and the hole concentration is decreased by donor-doping, the hole concentration is increased and the vacancy concentration is decreased by acceptor-doping.

The defect concentrations for donor- and acceptor-doped NiO are calculated for the dopant concentration (number of defects per cation sublattice site) of 10^{-4} . The calculations show that the vacancy concentration $[V'_{\text{Ni}}]$ is around 10^{-6} for undoped NiO, while it is 10^{-4} for donor-doped NiO at 700 °C at 0.21 bar (see Figure 2.1b). This indicates that even a small amount of dopant such as 10^{-4} influences the defect concentrations by several orders of magnitude, and the influence increases at low temperatures.

2.1.2. Chemical Diffusion Coefficient and Conductivity of Undoped and Doped NiO

2.1.2.1. Chemical Diffusion Coefficient

The chemical diffusion coefficient determines the kinetics of stoichiometry changes (uptake or release of a neutral component) in the case of transport control. While the ionic tracer (~self-diffusion) and defect diffusion coefficients consider only ionic transport, the chemical diffusion coefficient is the result of both ionic and electronic transport.

Here, the chemical diffusion coefficient is considered for NiO, for the case of doubly ionized vacancies. The more general formula and the detailed derivation can be found in ref. [28].

The flux of Ni ions (j_{Ni}) follows from the electroneutrality condition ($2j_{V_{\text{Ni}}''} = j_{h^{\bullet}}$) in NiO as

$$j_{\text{Ni}} = -\frac{1}{4F^2} \sigma_{\text{Ni}}^{\delta} \nabla \mu_{\text{Ni}} = -\left(\frac{1}{4F^2} \sigma_{\text{Ni}}^{\delta} \frac{\partial \mu_{\text{Ni}}}{\partial c_{\text{Ni}}} \right) \nabla c_{\text{Ni}} \quad (23)$$

where $\sigma^{\delta} = \sigma_{ion} \sigma_{eon} / (\sigma_{ion} + \sigma_{eon})$ is the ambipolar conductivity ($\sigma_{\text{Ni}}^{\delta} = \sigma_{V_{\text{Ni}}''} \sigma_{h^{\bullet}} / (\sigma_{V_{\text{Ni}}''} + \sigma_{h^{\bullet}})$), F the Faraday constant, μ_{Ni} the chemical potential of Ni and c_{Ni} the concentration of Ni ions ($\nabla \mu_{\text{Ni}}$: chemical potential gradient in the oxide film, and ∇c_{Ni} : Ni concentration gradient in the film). The expression in the brackets (in Eq. 23) gives the chemical diffusion coefficient of Ni in NiO, when the driving force is expressed in terms of a concentration gradient ∇c_{Ni} . Then, the chemical diffusion coefficient of NiO can be written as

$$D_{\text{Ni}}^{\delta} = \frac{1}{4F^2} \sigma_{\text{Ni}}^{\delta} \frac{\partial \mu_{\text{Ni}}}{\partial c_{\text{Ni}}} = \frac{kN_A T}{4F^2} \frac{\sigma_{\text{Ni}}^{\delta}}{c_{\text{Ni}}} \frac{\partial \ln a_{\text{Ni}}}{\partial \ln c_{\text{Ni}}} \quad (24)$$

where a_{Ni} is the Ni activity ($\partial \mu_{\text{Ni}} = RT \partial \ln a_{\text{Ni}}$), $\partial \ln a_{\text{Ni}} / \partial \ln c_{\text{Ni}} = w_{\text{Ni}}$ the thermodynamic factor and N_A the Avogadro number. The chemical diffusion coefficient can be further rewritten in terms of ionic and electronic defects, since $\partial \mu_{\text{Ni}} = \partial \mu_{V_{\text{Ni}}''} - 2\partial \mu_{h^{\bullet}}$ and $\partial c_{\text{Ni}} = \partial c_{V_{\text{Ni}}''} = -1/2 \partial c_{h^{\bullet}}$,

$$D_{\text{Ni}}^{\delta} = \frac{kN_{\text{A}}T}{4F^2} \frac{\sigma_{\text{V}_{\text{Ni}}}'' \sigma_{\text{h}^{\bullet}}}{\sigma_{\text{V}_{\text{Ni}}}'' + \sigma_{\text{h}^{\bullet}}} \left(\frac{1}{c_{\text{V}_{\text{Ni}}}''} \frac{\partial \ln a_{\text{V}_{\text{Ni}}}''}{\partial \ln c_{\text{V}_{\text{Ni}}}''} + \frac{4}{c_{\text{h}^{\bullet}}} \frac{\partial \ln a_{\text{h}^{\bullet}}}{\partial \ln c_{\text{h}^{\bullet}}} \right) \quad (25).$$

The thermodynamic factor is 1 for ideally dilute defects such as in NiO, thus

$$D_{\text{Ni}}^{\delta} = \frac{kN_{\text{A}}T}{4F^2} \frac{\sigma_{\text{V}_{\text{Ni}}}'' \sigma_{\text{h}^{\bullet}}}{\sigma_{\text{V}_{\text{Ni}}}'' + \sigma_{\text{h}^{\bullet}}} \left(\frac{1}{c_{\text{V}_{\text{Ni}}}''} + \frac{4}{c_{\text{h}^{\bullet}}} \right) = \frac{kN_{\text{A}}T}{4F^2} \sigma_{\text{V}_{\text{Ni}}}'' \left(\frac{1}{c_{\text{V}_{\text{Ni}}}''} + \frac{4}{c_{\text{h}^{\bullet}}} \right) \quad (26).$$

The ambipolar conductivity in Eq. 26 can be simplified to $\sigma_{\text{V}_{\text{Ni}}}''$ because in NiO the hole conductivity is much higher than the conductivity of vacancies ($\sigma_{\text{V}_{\text{Ni}}}'' + \sigma_{\text{h}^{\bullet}} \approx \sigma_{\text{h}^{\bullet}}$). One has to note that this equation is written for doubly ionized vacancies; for singly ionized vacancies the last term would be $1/c_{\text{h}^{\bullet}}$ (the difference stems from the ionization degree of Ni vacancies).

Here, the chemical diffusion coefficient is written only for doubly ionized vacancies by implementing the electroneutrality conditions for each case (undoped, donor- and acceptor-doped) into Eq. 26. In the same way, the chemical diffusion coefficients for the singly ionized vacancies could be obtained, as in Table 2.1. For undoped NiO, this yields D_{Ni}^{δ} as being $p\text{O}_2$ independent

$$D_{\text{Ni}}^{\delta} = 3D_{\text{V}_{\text{Ni}}}'' \quad (27).$$

For donor-doped NiO, one obtains

$$D_{\text{Ni}}^{\delta} = D_{\text{V}_{\text{Ni}}}'' \left(1 + \frac{2[\text{D}_{\text{Ni}}^{\bullet}]}{[\text{h}^{\bullet}]} \right) \quad (28).$$

This shows that the chemical diffusion coefficient of donor-doped NiO is negatively $p\text{O}_2$ dependent because the hole concentration (Eq. 16) is proportional to $p\text{O}_2^{1/4}$. Also, the chemical diffusion coefficient is increased by increasing the dopant concentration.

The combination of Eq. 26 and the electroneutrality condition ($[\text{h}^{\bullet}] = [\text{A}'_{\text{Ni}}]$) gives the chemical diffusion coefficient for acceptor-doped NiO as

$$D_{\text{Ni}}^{\delta} = D_{V_{\text{Ni}}}'' \quad (29)$$

which is $p\text{O}_2$ independent and equals the cation vacancy diffusion coefficient.

2.1.2.2. Conductivity of NiO

The electrical conductivity of the species (σ_i) is defined as in Eq. 30 where z_i is the valence number, u_i the mobility of species, and c_i the concentration of charged species

$$\sigma_i = z_i F u_i c_i = z_i F u_i^0 T^{-1} \exp\left(-\frac{\Delta H_i^m}{kT}\right) c_i \quad (30)$$

and ΔH_i^m is the activation enthalpy for defect migration.

In NiO, the conductivity is predominantly electronic and p-type. Consequently, the hole concentration is used in Eq. 30.

Also here, the hole conductivity is given only for the case of doubly ionized vacancies by implementing the electroneutrality conditions for each case (undoped, donor- and acceptor-doped) into Eq. 30. The conductivities and the activation energies for the singly ionized vacancies can be obtained similarly (see Table 2.1).

The combination of Eq. 7 and 30 gives the conductivity for undoped NiO as

$$\sigma_{h^{\bullet}} = 2^{4/3} F u_p^0 T^{-1} \exp\left(-\frac{\Delta H_1^0/3 + \Delta H_p^m}{kT}\right) \exp\left(\frac{\Delta S_1^0}{3k}\right) p\text{O}_2^{1/6} \quad (31)$$

and the activation energy in the case of doubly ionized vacancies as

$$E_{\sigma} = \Delta H_1^0/3 + \Delta H_p^m \quad (32).$$

The electronic conductivity of undoped NiO is proportional to $p\text{O}_2^{1/6}$ for doubly ionized vacancies and it is proportional to $p\text{O}_2^{1/4}$ for singly ionized vacancies (see Table 2.1).

The substitution of Eq. 16 into 30 gives the hole conductivity for donor-doped NiO with the assumption that the doubly ionized vacancies are predominant defects:

$$\sigma_{h^\bullet} = 2^{3/2} F u_p^0 T^{-1} \exp\left(-\frac{\Delta H_1^0/2 + \Delta H_p^m}{kT}\right) \exp\left(\frac{\Delta S_1^0}{2k}\right) \frac{pO_2^{1/4}}{[D_{Ni}^\bullet]^{1/2}} \quad (33).$$

The activation energy for conductivity of donor-doped NiO is

$$E_\sigma = \Delta H_1^0/2 + \Delta H_p^m \quad (34).$$

For the acceptor-doped NiO, substitution of the electroneutrality condition ($[h^\bullet] = [A'_{Ni}]$) into Eq. 30 yields

$$\sigma_{h^\bullet} = 2F u_p^0 T^{-1} \exp\left(-\frac{\Delta H_p^m}{kT}\right) [h^\bullet] \quad (35)$$

which shows that the conductivity activation energy is equal to the activation enthalpy for hole migration

$$E_\sigma = \Delta H_p^m \quad (36).$$

All equations for defect concentrations, conductivities and chemical diffusion coefficients, together with the equations for singly ionized vacancies, are summarized in Table 2.1.

Table 2.1: Summary of defect chemical model of undoped and doped-NiO

	if $[V''_{Ni}]$ is predominant	if $[V'_{Ni}]$ is predominant
undoped NiO	$2[V''_{Ni}] = [h^\bullet]$	$[V'_{Ni}] = [h^\bullet]$
	$K_1 = [V''_{Ni}][h^\bullet]^2/pO_2^{1/2}$	$K_2 = [V'_{Ni}][h^\bullet]/pO_2^{1/2}$
	$\sigma_{h^\bullet} = 2^{4/3}Fu_p^0T^{-1}\exp\left(-\frac{\Delta H_1^0/3 + \Delta H_p^m}{kT}\right)\exp\left(\frac{\Delta S_1^0}{3k}\right)pO_2^{1/6}$	$\sigma_{h^\bullet} = 2Fu_p^0T^{-1}\exp\left(-\frac{\Delta H_2^0/2 + \Delta H_p^m}{kT}\right)\exp\left(\frac{\Delta S_2^0}{2k}\right)pO_2^{1/4}$
	$E_\sigma = \Delta H_1^0/3 + \Delta H_p^m$	$E_\sigma = \Delta H_2^0/2 + \Delta H_p^m$
	$D_{Ni}^\delta = 3D_{V''_{Ni}}$	$D_{Ni}^\delta = 2D_{V'_{Ni}}$
	$[V''_{Ni}] \propto [h^\bullet] \propto pO_2^{1/6}$	$[V'_{Ni}] = [h^\bullet] \propto pO_2^{1/4}$
donor-doped NiO	$2[V''_{Ni}] = [D_{Ni}^\bullet]$	$[V'_{Ni}] = [D_{Ni}^\bullet]$
	$K_1 = [D_{Ni}^\bullet][h^\bullet]^2/2pO_2^{1/2}$	$K_2 = [D_{Ni}^\bullet][h^\bullet]/pO_2^{1/2}$
	$\sigma_{h^\bullet} = 2^{3/2}Fu_p^0T^{-1}\exp\left(-\frac{\Delta H_1^0/2 + \Delta H_p^m}{kT}\right)\exp\left(\frac{\Delta S_1^0}{2k}\right)\frac{pO_2^{1/4}}{[D_{Ni}^\bullet]^{1/2}}$	$\sigma_{h^\bullet} = 2Fu_p^0T^{-1}\exp\left(-\frac{\Delta H_2^0 + \Delta H_p^m}{kT}\right)\exp\left(\frac{\Delta S_2^0}{k}\right)\frac{pO_2^{1/2}}{[D_{Ni}^\bullet]}$
	$E_\sigma = \Delta H_1^0/2 + \Delta H_p^m$	$E_\sigma = \Delta H_2^0 + \Delta H_p^m$
	$D_{Ni}^\delta = D_{V''_{Ni}} \cdot \left(1 + \frac{2[D_{Ni}^\bullet]}{[h^\bullet]}\right)$	$D_{Ni}^\delta = D_{V'_{Ni}} \cdot \left(1 + \frac{[D_{Ni}^\bullet]}{[h^\bullet]}\right)$
$[h^\bullet] \propto pO_2^{1/4}$ and $D_{Ni}^\delta \propto pO_2^{-1/4} *$	$[h^\bullet] \propto pO_2^{1/2}$ and $D_{Ni}^\delta \propto pO_2^{-1/2} *$	
acceptor-doped NiO	$[h^\bullet] = [A'_{Ni}] = \text{constant}$	$[h^\bullet] = [A'_{Ni}] = \text{constant}$
	$K_1 = [A'_{Ni}]^2[V''_{Ni}]/pO_2^{1/2}$	$K_2 = [A'_{Ni}][V'_{Ni}]/pO_2^{1/2}$
	$\sigma_{h^\bullet} = 2Fu_p^0T^{-1}\exp\left(-\frac{\Delta H_p^m}{kT}\right)[h^\bullet]$	$\sigma_{h^\bullet} = 2Fu_p^0T^{-1}\exp\left(-\frac{\Delta H_p^m}{kT}\right)[h^\bullet]$
	$E_\sigma = \Delta H_p^m$	$E_\sigma = \Delta H_p^m$
	$D_{Ni}^\delta = D_{V''_{Ni}}$	$D_{Ni}^\delta = D_{V'_{Ni}}$
	$[V''_{Ni}] \propto pO_2^{1/2}$	$[V'_{Ni}] \propto pO_2^{1/2}$

*: the relation is only valid for $[D_{Ni}^\bullet] \gg [h^\bullet]$

2.1.3. Tracer Diffusion Coefficient of Ni in NiO

The tracer diffusion coefficient considers only ionic transport, without any chemical composition change, whereby the driving force is the configurational entropy. The tracer diffusion coefficient is similar to the self-diffusion coefficient ($D_{\text{Ni}}^* = f \cdot D_{\text{self}}$, where f is the correlation factor which is 0.78 for Ni [24]). From the Nernst-Einstein relation one obtains

$$\sigma_{V_{\text{Ni}}''} = \frac{D_{V_{\text{Ni}}''} [c_{V_{\text{Ni}}''}] 4F^2}{kN_A T} = \frac{D_{\text{Ni}}^* [c_{\text{Ni}}] 4F^2}{kN_A T} \quad (37)$$

with the tracer diffusion coefficient of Ni in NiO (D_{Ni}^*) being

$$D_{\text{Ni}}^* = [V_{\text{Ni}}''] D_{V_{\text{Ni}}''} \quad (38)$$

because $[c_{V_{\text{Ni}}''}]/[c_{\text{Ni}}] = [V_{\text{Ni}}'']$. In contrast to D_{Ni}^δ , D_{Ni}^* is $p\text{O}_2$ dependent because of the $p\text{O}_2$ dependence of $[V_{\text{Ni}}'']$. Since the $p\text{O}_2$ dependence of the doubly ionized vacancy concentration is 1/6 and $D_{V_{\text{Ni}}''}$ is $p\text{O}_2$ independent, D_{Ni}^* also shows $p\text{O}_2$ dependence of 1/6. Here, the tracer diffusion coefficient is given only for doubly ionized vacancies in undoped NiO.

2.2. Oxidation Kinetics of Metals

The oxidation reaction is



The growth of an oxide film starts with adsorption and ionization of oxygen molecules from the gas phase, followed by dissociation and incorporation into the first layer of the oxide. In the frame of this work, oxide nuclei formation or initial oxide layer growth will not be discussed in detail. All non-noble metals come with a native oxide layer, *i.e.*, the nuclei are formed when the metal is exposed to air even at room temperature. The oxidation of the first monolayer is very rapid and may form a protective layer on the metals against further corrosion (*e.g.*, Al₂O₃, Cr₂O₃, NiO). This applies also to formation of other binary compounds such as chlorides, sulfides, nitrides etc., by a solid-state reaction. Here, the further growth of the oxide layer will be discussed in detail. After the formation of a dense native oxide layer, further oxidation of corrosion-resistant metals requires transport of ionic and electronic species through the layer and hence elevated temperatures.

There are two main theories to describe the oxidation kinetics of metals and metal films [3]: (i) the Wagner theory [1] for thicker films and higher temperatures where the oxidation is limited by the chemical diffusion through the oxide (*i.e.*, field effects are negligible), leading to a parabolic rate law. The transport of the species is controlled by the diffusion law and is related to the defect structure of the oxide [29]. Defect concentrations in the oxide structure can be modified by temperature, oxygen partial pressure, and doping. (ii) The Cabrera-Mott theory [2] is described for the formation of very thin oxide films at relatively low temperatures. Here, the electric field resulting from tunneling of electrons from the metal to chemisorbed oxygen species at the oxide surface accelerates the overall (slow) ionic transport across the film, by increasing the defect injection rate at the interface (metal-oxide or oxide-gas). Its decrease with increasing film thickness leads to a negligible growth rate once a "limiting thickness" of a few nm is reached.

2.2.1. Wagner Theory of Oxidation

First observations of a parabolic rate law were reported by Tammann [30], and Pilling and Bedworth [31] for heterogeneous reactions such as formation of oxides, sulfides, fluorides, etc.,

$$X^2 = k_p t \quad (40)$$

where k_p is the parabolic rate constant (referred to the text as reaction rate or oxidation rate constant), X the film thickness and t time.

The principles of Wagner theory [1] are outlined by different authors, *e.g.*, [3, 28, 29, 32], and a brief summary of the thick film oxidation kinetics is given hereby according to Wagner's assumptions. Wagner describes the oxidation kinetics of a metal for a relatively thick oxide layer formation at relatively high temperatures [1]. The theory considers the formation of a compact oxide layer and assumes that the oxidation is diffusion controlled [1, 28, 32, 33]. If the molar volume of the growing oxide layer and the metal does not differ extremely, the initial oxidation layer will be compact [31, 33]. After the formation of a gas-tight initial oxide layer, chemical transport through the oxide layer is essential for the further oxidation reaction. The metal has to diffuse outwards by ambipolar (chemical) diffusion of metal ions and electronic carriers, and/or the oxygen must diffuse inwards. Since the diffusion of ionic and electronic species is essential for the oxidation reaction, the oxide layer should be ionically and electronically conductive.

The flux of the metal ions through the oxide layer is already described in Eq. 23 for the chemical diffusion of Ni in NiO. The oxidation process is determined by ambipolar conductivity (σ_o^δ or σ_{Me}^δ) together with the chemical potential gradient. Depending on defect chemistry and electronic structure of the oxide, metal or oxygen ions can dominate the ion diffusion, and the electronic current is carried by electrons or holes. The flux equation is repeated here for the flux of metal, to be consistent with section 2.1.2, to obtain an expression for k_p

$$j_{\text{Me}} = -\frac{1}{4F^2} \sigma_{\text{Me}}^{\delta} \nabla \mu_{\text{Me}} = -\frac{1}{4F^2} \bar{\sigma}_{\text{Me}}^{\delta} \frac{\Delta \mu_{\text{Me}}}{X} \quad (41)$$

where $\sigma_{\text{Me}}^{\delta}$ is approximately equal to the ionic conductivity (for $t_{e_{on}} \gg t_{i_{on}}$), and the bar indicates the ambipolar conductivity averaged over the oxide film with a chemical potential gradient. For predominant cation diffusion, metal ions diffuse outwards to the surface and are converted to metal oxide. Accordingly, the flux of metal ions is directly related to the growth in oxide thickness dX/dt and therefore to the reaction rate constant k_p . Since $\partial n_{\text{Me}}/\partial t = \partial n_{\text{MeO}}/\partial t = \partial V_{\text{MeO}}/\partial t \cdot v_{\text{MeO}}$ (n : mole number, V_{MeO} : volume of metal oxide and v_{MeO} : molar volume of metal oxide), $V(t)=X(t) \cdot \text{area}$, and $dX/dt = k_p/2X$ one obtains

$$\frac{k_p}{2X} = j_{\text{Me}} \cdot v_{\text{MeO}} = -\frac{1}{4F^2} \frac{V_{\text{M}}}{X} \int_{\mu_{\text{Me(O}_2)}}^{\mu_{\text{Me}}} t_{i_{on}} t_{e_{on}} \sigma_{\text{Me}} \cdot d\mu_{\text{Me}} \quad (42)$$

where σ_{Me} is the total electronic conductivity, $t_{i_{on}} = \sigma_{i_{on}}/(\sigma_{i_{on}} + \sigma_{e_{on}})$ the transference number of ions, and $t_{e_{on}} = \sigma_{e_{on}}/(\sigma_{i_{on}} + \sigma_{e_{on}})$ the transference number of electrons. The limits of integration in Eq. 42 are the metal activities at the oxide-gas interface ($\mu_{\text{Me(O}_2)}$) and the metal-oxide interface (μ_{Me}). Eq. 42 shows that the growth rate of an oxide film is controlled by the chemical potential gradient over the film, which becomes smaller with increasing film thickness, slowing down the oxidation process.

Figure 2.2 illustrates the ambipolar diffusion in a growing oxide film. μ_{Me} is the chemical potential of the metal. The difference between μ_{Me} in MeO in equilibrium with O_2 (at the gas-oxide interface) and μ_{Me} in MeO in equilibrium with metal (at the metal-oxide interface) gives the chemical potential difference of the metal ($\Delta \mu_{\text{Me}}$). Similarly, $\Delta \mu_{\text{O}}$ is the difference between μ_{O} in MeO in equilibrium with O_2 (at the gas-oxide interface) and μ_{O} in MeO in equilibrium with metal (at the metal-oxide interface), and $\Delta \mu_{\text{O}} = -\Delta \mu_{\text{Me}}$.

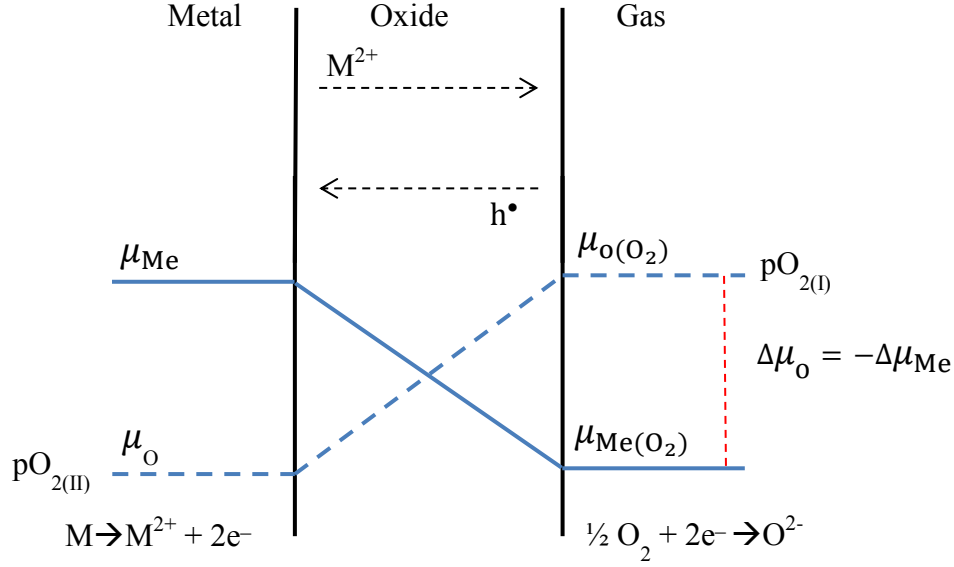


Figure 2.2: Transport of ions and holes in the chemical potential gradient in a growing oxide film according to Wagner's oxidation theory, exemplified for an oxide with predominant metal diffusion via M^{2+} and h^\bullet .

It is clear that the conductivity of point defects is directly related to the reaction rate constant in Eq. 42. Replacing the conductivities in Eq. 42 by diffusion coefficients through the Nernst-Einstein relation, and using $c_i = 1/v_{MeO}$, one obtains

$$k_p = \frac{1}{k_{NA}T} \int_{\mu_{Me(O_2)}}^{\mu_{Me}} t_{eon} (D_{Me}^* + D_O^*) \cdot d\mu_{Me} = \bar{t}_{eon} (\bar{D}_{Me}^* + \bar{D}_O^*) \frac{\Delta\mu_{Me}}{k_{NA}T} \quad (43).$$

The tracer diffusion coefficient (D_{Me}^*) depends on the chemical potential and the bar indicates the average diffusion coefficient. For the transition metal oxides such as CoO, NiO, FeO, etc., $t_{eon} \sim 1$, and $D_O \ll D_{Me}$, consequently the relation becomes simpler, namely

$$k_p = \frac{\bar{D}_{Me}^*}{k_{NA}T} \Delta\mu_{Me} \quad (44)$$

where $\Delta\mu_{Me}$ is the chemical potential difference on both sides. For $pO_2=1$

$$\Delta\mu_{Me} = \Delta G^\circ = \Delta H^\circ - T\Delta S^\circ \quad (45)$$

where ΔG° is the standard molar Gibbs energy for the oxide formation. ΔH° is the standard molar enthalpy of the oxide formation and ΔS° is the standard molar entropy of the oxidation reaction and both are assumed to be temperature independent.

Since \bar{D}_{Me}^* is weakly pO_2 dependent as explained in section 2.1.3, k_p is also weakly pO_2 dependent.

2.2.2. Cabrera - Mott Theory of Oxidation

When an electric field is present and not negligible in a thin film, and has an influence on the migration of ions, the kinetics of metal oxidation does not obey the parabolic rate law. To describe such cases, other theories were introduced by different authors [6, 8]. The most important theory was given by Cabrera and Mott [2].

Cabrera and Mott assumed that the electrons can tunnel through the thin oxide film from the metal and ionize the adsorbed oxygen molecules at the gas-oxide interface. A uniform electric field in the growing oxide film is created by charges at the two interfaces: a positive charge at the metal-oxide interface and a negative charge at the gas-oxide surface (Figure 2.3 taken from ref. [3]). This electric field accelerates the overall ion transport through the oxide film by decreasing defect-injection barrier into the oxide at the interfaces. According to Cabrera and Mott, one of two scenarios can be the limiting factor for the reaction kinetics: (i) injection of oxygen vacancies or metal interstitials into the oxide at the metal-oxide interface, (ii) injection of metal vacancies or oxygen interstitials into the oxide at the oxide-gas interface. The transfer (injection) of these defects at the interfaces is accelerated by the electric field. The oxide growth rate for these two scenarios is explained by slightly different relations that show similar temperature limits and slightly different thickness limits for the validity of Cabrera - Mott theory. A brief summary of both scenarios can be found in Atkinson's review on oxidation kinetics [3]. Here only one of the possibilities is discussed.

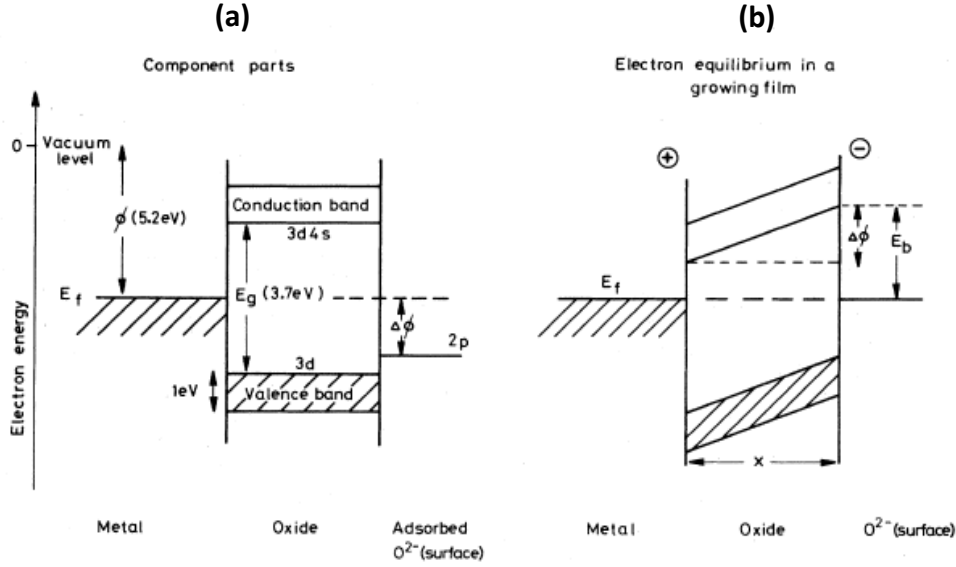


Figure 2.3: Energy levels (a) before and (b) after the initial transfer of electrons for Ni. The figure is taken from [3] with permission of the copyright.

For the case of injection of oxygen vacancies or metal interstitials into the oxide at the metal-oxide interface, the growth rate is given by

$$\frac{dX}{dt} = av \exp\left(-\frac{W}{kT}\right) \exp\left(\frac{qa\Delta\phi}{2kTX}\right) \quad (46)$$

where v is the vibrational frequency of atoms at the interface, a the atomic jump distance, $\Delta\phi$ the electrical potential difference across the oxide film, and W the barrier for an atomic jump. This equation can be simplified by using $X_1 = qa\Delta\phi/2kT$ (X_1 : upper limit of validity of underlying assumptions) and bulk diffusivity, $D_i = a^2 v \exp(-W/kT)$ (D_i : bulk diffusivity):

$$\frac{dX}{dt} = \frac{D_i}{a} \exp\left(\frac{X_1}{X}\right) \quad (47).$$

Eq. 47 predicts an oxidation rate constant that exponentially decreases with the thickness of the growing oxide film. When $X \ll X_1$, Eq. 48 yields inverse logarithmic kinetics:

$$\frac{X_1}{X} = -\ln\left(\frac{D_i X_1 t}{a X_1^2}\right) \quad (48)$$

where X_L is the critical thickness defined by the limiting temperature of which the growth rate becomes negligible. Setting this criterion to 10^{-15} m/s yields

$$X_L = \frac{X_1}{\left(\frac{W}{kT} - 39\right)} \quad (49).$$

A temperature upper limit can be estimated by setting $X_L = X_1$; it yields $T=W/40k$. Below the critical temperature, the film growth will be controlled by inverse logarithmic kinetics up to a critical thickness (X_1). Above the critical temperature ($T > W/40k$), the film growth controlled by inverse logarithmic kinetics will stop at X_L , and continue with the parabolic rate law.

Atkinson assumed that the activation energy of the tracer diffusion coefficient of Ni in NiO can be used as an approximation for W [3], in order to estimate a limiting temperature for the validity of the Cabrera-Mott theory. Atkinson [3] calculated two critical temperatures of ~ 500 °C and ~ 250 °C for Ni oxidation, by using two different activation energies: for the bulk diffusion coefficient $E_a=2.56$ eV [34] and for the grain boundary diffusion coefficient $E_a=1.78$ eV [34], respectively. In this work (see section 4.1.3), using tracer diffusion coefficient activation energy 1.7 ± 0.1 eV would yield similar temperatures (220 ± 30 °C) to Atkinson's second estimation. However, E_a (of D^*) contains the defect formation and migration enthalpies. Here, it is considered that the activation energy of the vacancy diffusion coefficient can give a more reasonable estimation (migration barrier only). In the frame of the present work, *i.e.*, for Ni oxidation, the activation energy of Ni-vacancy diffusion coefficient is considered as a value for W which is $E_a=1.34$ eV in Morlotti's study [35]. This activation energy of 1.34 eV yields a critical temperature of 116 °C for the validity of Cabrera-Mott theory.

The limiting thicknesses of about 4.5 nm considering the activation energy of vacancy diffusion coefficient, and 3.6 ± 0.2 nm considering the activation energy of tracer diffusion coefficient are calculated from Eq. 49 by using the critical temperature limits (116 °C and 220 ± 30 °C, respectively), a potential drop of 1 V at the gas-oxide interface and an atomic jump distance of 3 Å. The estimated limiting thickness and the temperature in this work are

much lower than general assumptions in the literature for the validity of Cabrera Mott-theory (~ 20 nm and ~ 250 °C).

2.2.3. Surface Reaction Controlled Oxidation

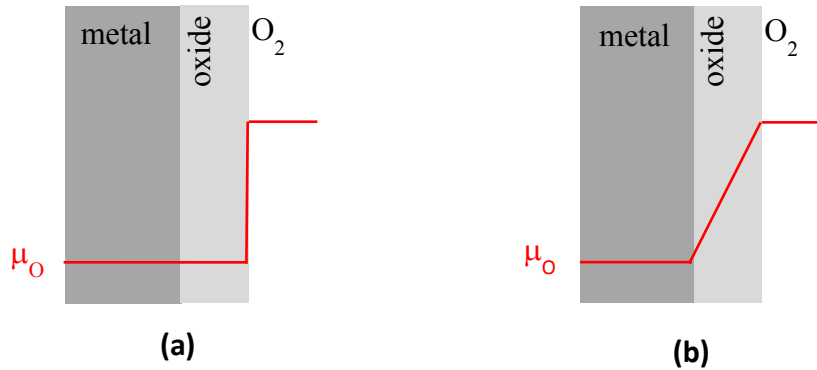


Figure 2.4: (a) surface reaction controlled oxidation (b) chemical diffusion controlled oxidation process.

If the oxidation reaction is controlled by diffusion, the driving force for the oxidation is the chemical potential gradient over the growing oxide film, as indicated in Figure 2.4b (Wagner theory). If the reaction is surface controlled, the oxygen concentration is always homogeneous through the growing oxide film and there is a chemical potential step at the surface which is the driving force in surface reaction controlled oxidation processes (Figure 2.4a). The flux of oxygen is given by

$$j_o = -k^\delta \delta c_o \quad (50)$$

where k^δ is the effective surface rate constant and δc_o the oxygen concentration variation at the oxide-gas surface. Since the oxygen concentration is invariant during the oxide film growth, δc_o remains constant as long as there is still metal beneath the oxide film. As a consequence, Eq. 50 gives a constant j_o which yields the linear relation of oxide thickness growth rate and the oxide film thickness.

3. Experimental Methods

3.1. *In-situ* Oxidation Measurements of Metal Films

3.1.1. Sample preparation

3.1.1.1. *Electron Gun Beam Evaporation of Metals*

Cr, Al, Ti, V, Zn, Ni, and Co metal films for oxidation measurements were prepared in a thickness range between 10 and 150 nm by electron beam evaporation at $\sim 10^{-6}$ Torr at room temperature on polycrystalline (*KERAFOL*, 0.25 mm thick) and single crystalline Al_2O_3 (sapphire, *CrysTec*, 0.25 mm thick) substrates. Thickness measurements were performed with a surface profilometer ($\text{Ø} = 2 \mu\text{m}$, *Dektak XT*, *Bruker*) with a representative sample on a silicon substrate which is half covered with positive photoresist to form a step on the sample surface. The metals as a source material for e-beam evaporation were provided commercially from different companies (Alfa Aesar, Umicore, LH, etc.) with minimum 99.5% purity. E-beam evaporation of the metals and the thickness measurements of the samples were performed in the Technology Scientific Service Group.

After the metal film growth by e-beam evaporation, platinum electrodes of a thickness of ~ 400 nm were sputter-deposited (*Edwards Auto 306* at 5×10^{-2} mbar, Ar, 60 W) close to the edges (see Figure 3.1) of the sample using a shadow mask.

3.1.1.2. Cr-doped Ni Alloy and Film Preparation

Cr-doped Ni alloy was prepared by alloying the required amounts of Cr and Ni metal. The mixtures of Cr and Ni were melted in an aluminum oxide crucible with 11 kW power in an induction furnace in Ar atmosphere at 500 mbar. The produced alloy was heat treated in a tube furnace together with a zirconium bar (to take up the residual oxygen in the oven) in an aluminum oxide crucible at 1200 °C for 24 hours in Ar atmosphere for homogenization. The targeted Cr concentration in the Ni was 0.1 and 1 %. After the homogenization process, chemical analysis was performed by inductively coupled plasma optical emission spectroscopy (ICP-OES) and the results are presented in Table 3.1, for details see section 3.3.1.

Table 3.1: Chemical analysis of the casted alloy by ICP-OES

desired sample	Cr (mol %)
1 % Cr-doped Ni	1.030±0.020
0.1 % Cr-doped Ni	0.138±0.002

The thin films from these alloys are prepared by two different methods: e-beam evaporation and pulsed laser deposition (PLD). Since e-beam evaporation did not provide a homogeneous Cr distribution through the thickness of sample (see section 4.2.1), pulsed laser deposition was used as an alternative technique to achieve homogeneously distributed Cr in Ni films.

E-beam evaporation was employed for 0.1 and 1 % Cr-doped Ni films for thickness range between 12 nm and 50 nm. The samples are produced with the same technique as described in section 3.1.1.1.

Pulsed Laser Deposition (PLD) was used for the deposition of 1 % Cr-doped Ni films of about 100 nm thickness. The metal films were deposited on sapphire substrates at substrate temperatures of -180 °C and 25 °C for 4 hours. The deposition was performed

with a femtosecond laser (516 nm, 30-50 mW, 1 kHz) at 3×10^{-8} mbar from a rotating alloy target.

3.1.1.3. Magnetron Sputtering

DC Magnetron sputtering (*ATC 1500-F Sputtering System, Aja International Inc.*) was used in the Thin Film Laboratory of Max Planck Institute for Intelligent Systems for deposition of 100 nm thick 1 % Cr-doped Ni films. Two different substrate temperatures (25 °C and 400 °C) were tried in order to prepare homogenous samples. As a source material, Ni (Lesker, #VPU 100682, 99.995%) and Cr (Lesker, #588483, 99.95%) metals were used. The deposition was completed in 10 minutes operating the Ni target (250 W) and the Cr target (3 W) simultaneously while the substrate was rotating with 10 rpm at 10^{-3} mbar in Ar atmosphere (see Figure 4.16 for XPS depth profile of the metal film).

3.1.2. Electrochemical Impedance Spectroscopy (EIS)

During the oxidation of metal films on Al_2O_3 substrates in a tube furnace, the resistance changes were measured by electrical impedance spectroscopy laterally across the sample by 2-point EIS and fitted with an equivalent circuit model. Impedance measurements were performed by using computer controlled *Newton PSM1700 Phase Sensitive Multimeter* and *Novocontrol Alpha-A High Performance Frequency Analyzer* in the frequency range between 100 Hz to 1 MHz at 100 mV AC amplitude. The data were analyzed, by fitting, using the *ZView* software (*Scribner Associates, Inc.*). The conductivity of the metals is much higher than the conductivity of the metal oxides, therefore the conductance measured during the oxidation refers to the remaining metallic film. The oxide thickness was calculated from the resistance values ($R = \rho l / A$) of the remaining metallic part of the film. The molar volume difference between the metal and the oxide was considered in the calculations (see Table 4.1).

3.1.3. Experimental Conditions

50 nm thick Cr, Al, Ti, V, Zn, Ni, and Co metal films were evaporated on polycrystalline Al₂O₃ substrates and the resistance changes of the films were measured *in-situ* during thermal oxidation by electrochemical impedance spectroscopy at a temperature range between 200 and 500 °C in a tube furnace in air. Additional measurements under diverse experimental conditions were performed for some of the metals to further investigate the oxidation kinetics. First, the thickness range of the metal films was reduced from 50 nm to 10-20 nm and increased to 150 nm to observe the effect of thickness change on the oxidation rate constant of Cr, Ni and Co. Second, the effect of UV light exposure on the oxidation kinetics of the 50 nm Ni samples was investigated. UV light was irradiated on the Ni samples using a 200 W high-pressure mercury arc lamp as a light source (*Oriel Instruments*) during the oxidation in air (see Figure 3.3). Two filters and one lens were placed between the sample holder and the UV light source. While the UG5 filter eliminates the wavelength in the visible range to reduce the additional heat by the light source on the sample, the WG 280 filter excludes the wavelengths below 280 nm, which could generate ozone (O₃). The lens was used to collimate the UV light on the sample. The intensity of the UV light was measured by a bolometer and found to be 144 mW/cm². Third, the oxidation measurements of the Ni films were performed not only in air but also at a reduced oxygen partial pressure of 10⁻³ bar, achieved by using a closed sample holder with 25 ml/min gas flow. Finally, a 45±5 ml/min gas flow of O₂ was passed through an ozone generator (*Anseros Ozone Generator Com*) and was introduced in the closed sample holder to enhance the concentration of O₂ molecules on the sample surface.

3.1.4. Experimental Set-Up

In-situ oxidation measurements on thin metallic films were performed in a tube furnace with a *Eurotherm* temperature controller. The typical sample geometry with the sputtered Pt electrodes is shown in Figure 3.1.

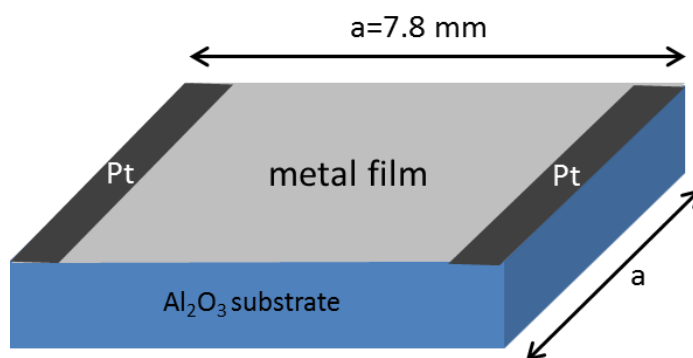


Figure 3.1: The typical geometry of the thin metallic films (10-150 nm) with Pt electrodes for *in-situ* oxidation measurements on an Al_2O_3 substrate.

The temperature of the sample was checked with a thermocouple which was attached to the sample holder very close to the sample. Figure 3.2 illustrates the sample holder for the *in-situ* oxidation measurements, the front view of the sample holder where the sample is located and the representative oxidation steps of the Ni sample.

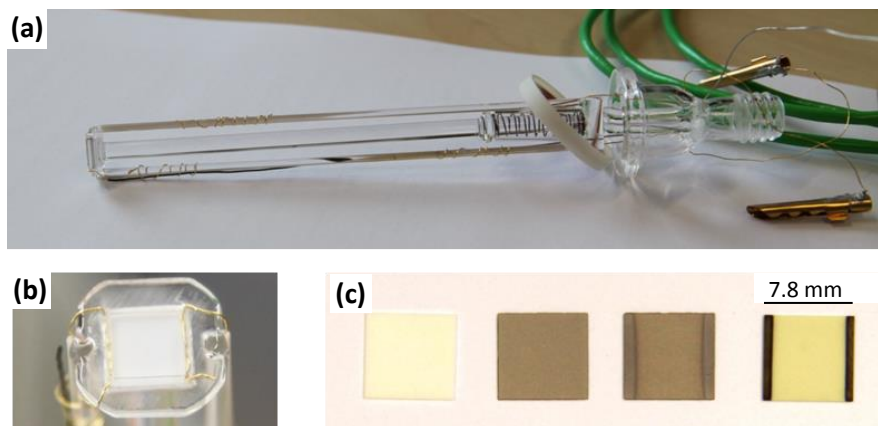


Figure 3.2: Experimental set-up for *in-situ* oxidation measurement. (a) Quartz sample holder for a tube furnace with gold wires and thermocouple [36], (b) front view of the sample holder where sample is located and can be irradiated by UV light [36], (c) representative steps of a sample (Ni); bare polycrystalline Al_2O_3 substrate / metal film evaporated on the substrate / Pt electron sputtered on the metal film / oxidized sample).

The set-up for UV illumination on the sample surface is presented in Figure 3.3. During UV illumination, the sample is being oxidized in a tube furnace in air.

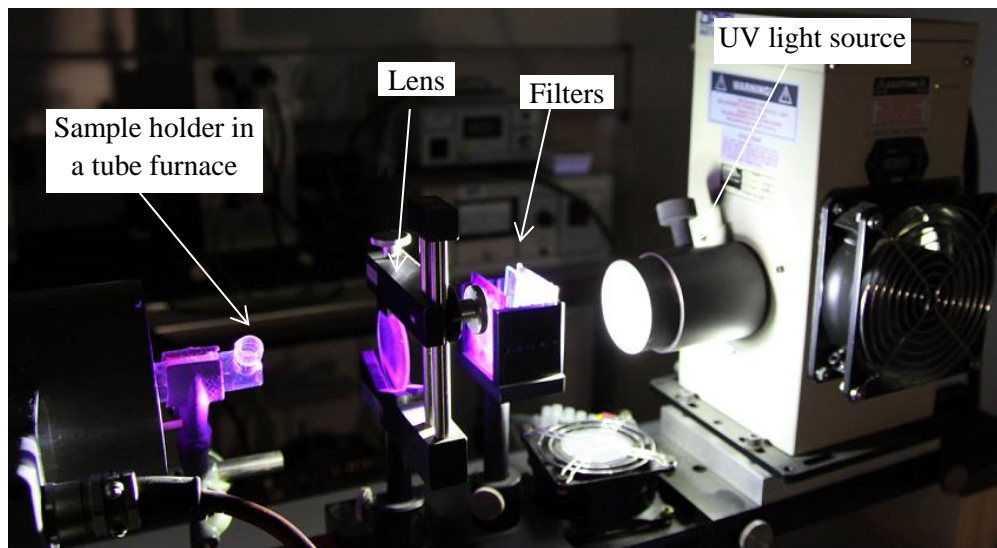


Figure 3.3: Experimental set-up for UV illumination on the sample surface for *in-situ* oxidation measurement under UV light to accelerate the surface reaction [36].

The morphology of the sample was investigated by AFM (Atomic Force Microscopy, *Cypher, Asylum*). In Figure 3.4, AFM images of the polycrystalline substrate, the 50 nm Ni film and the oxidized Ni film are presented.

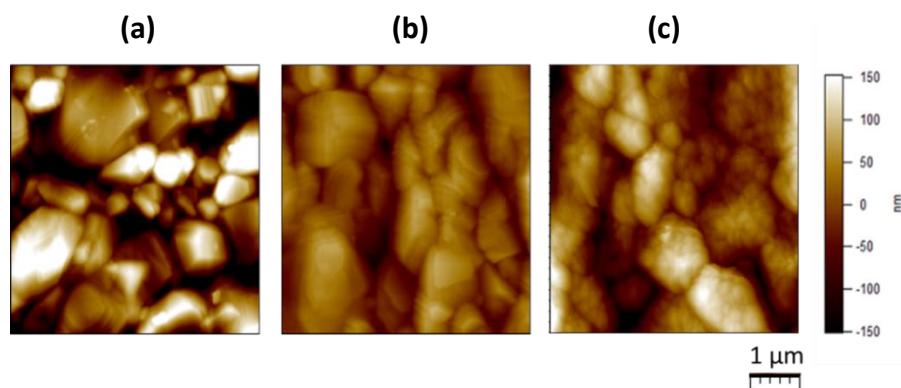


Figure 3.4: Tapping mode AFM images: (a) The bare polycrystalline Al_2O_3 substrate, (b) the 50 nm thick e-beam evaporated Ni film on the Al_2O_3 substrate and (c) the film after oxidation (cauliflower-like NiO film).

3.2. Conductivity Relaxation Measurements (ECR)

Due to the difficulties of modifying the grain size and obtaining homogeneously distributed donor doping in an oxide film, undoped and donor-doped NiO ceramic samples were investigated by conductivity relaxation measurements after stepwise pO_2 changes. The aim of the conductivity relaxation measurements of undoped and Cr-doped NiO ceramics is to understand the Cr doping effect on transport properties (conductivity and chemical diffusion coefficient) of the ceramic samples as a function of temperature, oxygen partial pressure, Cr concentration, and grain size.

3.2.1. Sample Preparation

3.2.1.1. Powder Synthesis

Undoped and Cr-doped NiO powders were synthesized by the nitrate-glycine synthesis method modified from literature [37-41]. For NiO, 0.1 mol $Ni(NO_3)_2 \cdot 6H_2O$ (99.9985 % purity, Alfa Aesar) was dissolved in 25 ml distilled water at ambient temperature. To this, 0.1 mol glycine (≥ 99 % (NT), Fluka) was added and dissolved with a magnetic stirrer for 10 min in a large beaker in a fume hood. Then, the mixture was heated on a hot plate to 105 °C to evaporate the water for 30 minutes, and the gelation process started by evaporation of most of the water until a dark-green gel formed. Then, the beaker was covered with a glass lid to keep the synthesized product in the beaker because vigorous combustion occurs during the synthesis. The temperature was slowly increased up to 300 °C in 15 min when the combustion occurred. After the combustion, dark-green fine powders with a 60-70 nm crystallite size were obtained. The nanopowders were calcined for 1 h at 750 °C in air with 10 °C/min heating and cooling rate. XRD analyses of NiO powders were performed and the results are shown in Figure 3.5. All the peak positions belong to NiO, but there is a very small additional peak at 44° (2theta) for 3 % Cr-doped NiO which belongs to metallic Ni.

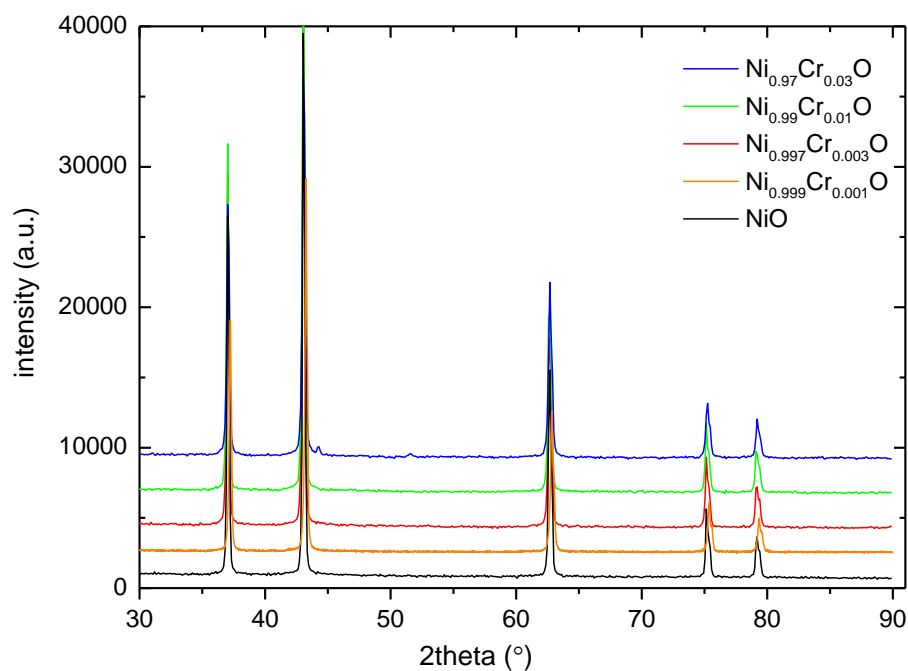


Figure 3.5: X-Ray diffraction patterns of the synthesized NiO powders after calcination at 750 °C for 1 h.

Cr-doped NiO powders were synthesized with the same technique by adding the required amount of $\text{Cr}(\text{NO}_3)_3 \cdot 9\text{H}_2\text{O}$ (99 % purity, Sigma-Aldrich), and the chemical analysis results of the powders are listed in Table 3.2.

Table 3.2: Results of the chemical analysis of synthesized powders by ICP-OES

nominal formula	Cr	impurities (at.%)	
	(at.%)	K	Fe
NiO	0.00	0.06	0.03
$\text{Ni}_{0.999}\text{Cr}_{0.001}\text{O}$	0.13	0.08	0.01
$\text{Ni}_{0.997}\text{Cr}_{0.003}\text{O}$	0.36	0.08	0.01
$\text{Ni}_{0.99}\text{Cr}_{0.01}\text{O}$	1.19	0.04	0.01
$\text{Ni}_{0.97}\text{Cr}_{0.03}\text{O}$	3.59	0.12	0.03

3.2.1.2. Spark Plasma Sintering (SPS)

Undoped and Cr-doped NiO polycrystalline ceramic pellets were compacted by spark plasma sintering (SPS system, HP D 5/2, FCT-Systeme GmbH, Germany) to obtain high-density pellets. About 1 g powder was put into the graphite mold (10 mm diameter) with a platinum foil to avoid NiO reduction to metallic Ni and sintered for 5 min at desired sintering temperature with 100 K/min heating rate and 9.2 kN pressure (see Table 3.3). Pellet densities above 95 % are required to obtain a well-defined diffusion length. Typical geometry of the cylindrical samples (pellets) was 1 mm thickness and 10 mm diameter. The density of pellets was derived from the geometry and the weight of the samples.

Table 3.3: The parameters of temperature, time and pressure for pellet preparation by SPS

nominal formula	sintering temperature (°C)	time (min)	pressure (MPa)	density (%)
NiO	1000	5	117	100
Ni _{0.999} Cr _{0.001} O	1000	5	117	99
Ni _{0.997} Cr _{0.003} O	1000	5	117	99
Ni _{0.99} Cr _{0.01} O	1150	5	117	95
Ni _{0.97} Cr _{0.03} O	1150	5	117	96

3.2.1.3. Grain Size Modification by Annealing

The pellets were cut into four equal pieces with a diamond wire saw and each quarter of the pellets was used for different heat treatments (annealing). The pellets obtained directly from SPS are in the following termed “as-prepared pellets”. Some pieces of these pellets were post-annealed at 1500 °C for 8 h and they are referred to as “annealed samples” (see Table 3.4). Additional annealing conditions were applied for several samples to investigate the effect of conditions such as shorter annealing time (5 min at 1500 °C) or lower annealing temperature (8 h at 1300 °C) on the grain size of the samples. Further details about annealing conditions are summarized in Table 3.4. The grain size of the ceramic

samples could be controlled by annealing. The effect of these different annealing conditions on the grain size of 0.1 % Cr-doped NiO is shown in the SEM images in Figure 3.6 and listed in Table 3.5. The average grain sizes are 400 nm for the as-prepared sample, 2-4 μm for the annealed sample at 1300 $^{\circ}\text{C}$ for 8 h, 2-4 μm for the annealed sample at 1300 $^{\circ}\text{C}$ for 5 min, and 4-10 μm for the annealed sample at 1500 $^{\circ}\text{C}$ for 8 h.

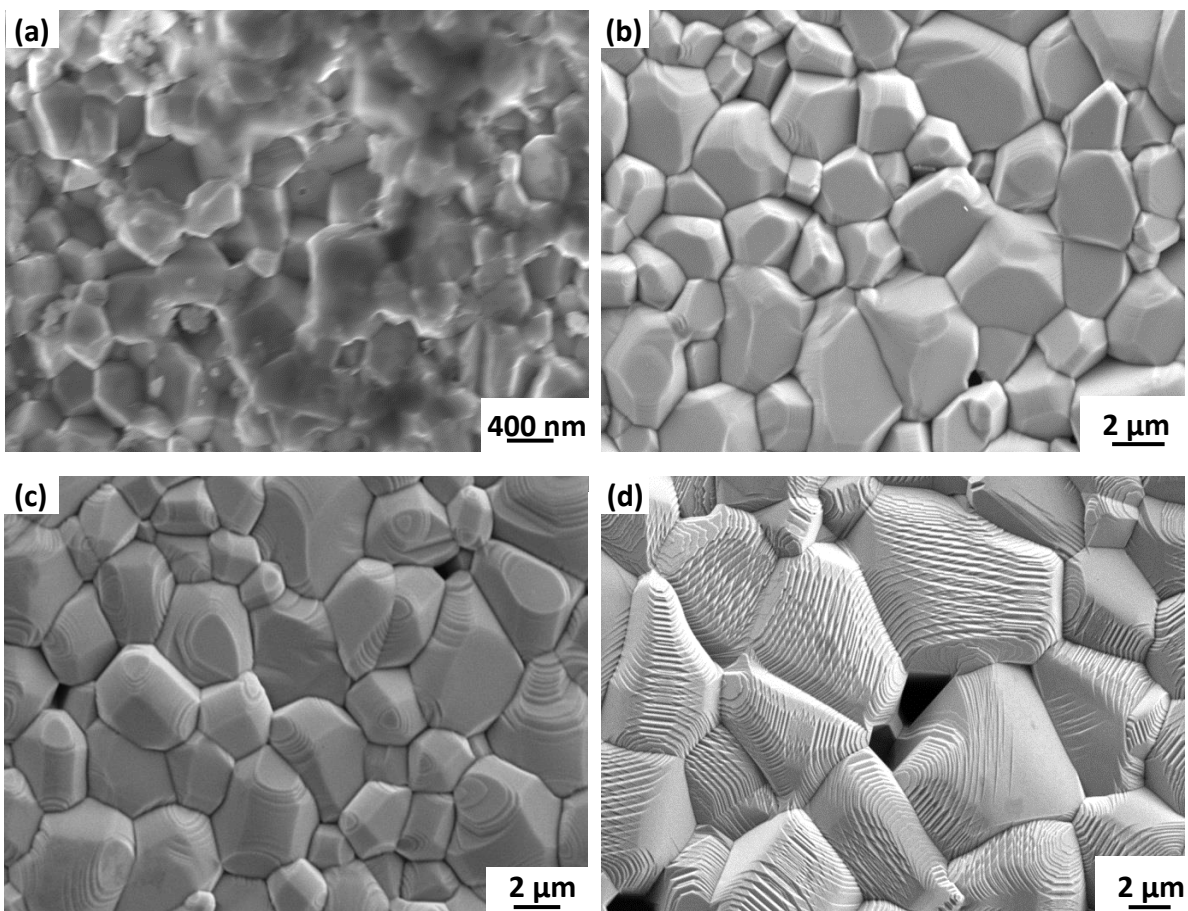


Figure 3.6: SEM images of 0.1 % Cr-doped NiO pellets: (a) the as-prepared, (b) the annealed at 1300 $^{\circ}\text{C}$ for 8 h, (c) the annealed at 1500 $^{\circ}\text{C}$ for 5 min, and (d) the annealed at 1500 $^{\circ}\text{C}$ for 8 h.

Table 3.4: Annealing conditions of the samples

samples	annealing conditions	abbreviation used in the text
all pellets	no annealing	as-prepared
all pellets	1500 °C / 8 h	annealed
0.1 % Cr-doped NiO	1300 °C / 8 h	-
0.1 and 1 % Cr-doped NiO	1500 °C / 5 min	-

Table 3.5: Grain size of the samples prepared under different annealing conditions

concentration of Cr (at.%)	as-prepared (μm)	annealed at 1500 °C for 8 h (μm)
0	1	2 to 10
0.1	0.2 to 0.4	4 to 12
0.3	0.4 to 1	4 to 12
1	0.4 to 1	4 to 15
3	0.5 to 1	5 to 20

After the annealing of the quarters of the pellets, platinum electrodes of a thickness of about 400 nm were sputtered on the surface of the pellets for conductivity measurements.

3.2.2. Conductivity Measurements

3.2.2.1. Conductivity Measurements by EIS

Electrochemical impedance spectroscopy (*Solartron SI 1260 Impedance/Gain Phase Analyzer, Schlumberger*) was used for conductivity relaxation measurements for undoped and Cr-doped NiO in the frequency range between 1 kHz to 1 MHz. The measurements were performed in a temperature range between 500 and 800 °C. Oxygen partial pressure dependences of the conductivity were measured between 10^{-3} to 1 bar with one order of magnitude steps in oxygen partial pressure mostly at 700 °C. A possible grain boundary blocking effect was investigated with measurements at 200 °C and 300 °C (to be able to see the low-frequency semicircle expected for blocking grain boundaries) in the frequency range between 10 MHz and 0.3 mHz.

3.2.2.2. Conductivity Relaxation Experiments

For the time dependence of the overall conductivity as a long time solution can be derived for the case of a plate-shaped sample (1-dimensional diffusion) [28]:

$$M_\sigma = \frac{\sigma(t) - \sigma_2}{\sigma_1 - \sigma_2} \approx \frac{8}{\pi^2} \exp\left(-\frac{t}{\tau^\delta}\right) \quad (51)$$

$$\tau^\delta = \frac{L^2}{\pi^2 D^\delta} \quad (52)$$

where σ_1 and σ_2 are the initial and final conductivities, respectively, and $\sigma(t)$ is the time-dependent conductivity. The parameter L is the (full) sample thickness and τ^δ is the time constant. First, the sample was equilibrated at a given pressure and fixed temperature. When the sample reached equilibrium at the initial conductivity, the partial pressure was abruptly changed to a new pressure and the conductivity was measured as a function of time until the new equilibrium was reached.

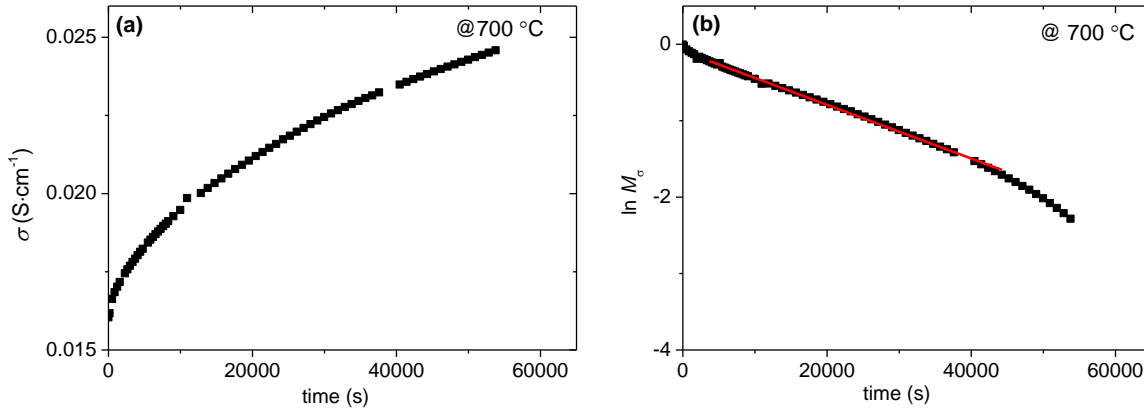


Figure 3.7: Results of conductivity relaxation measurement of as-prepared 0.1 % Cr-doped NiO sample: (a) Conductivity vs. time after stepwise oxygen partial pressure increase, (b) calculated value of M_σ (red line=fit to Eq. 51).

The conductivity values are presented in Figure 3.7a, and the $\ln M_\sigma$ vs. *time* graph is plotted using Eq. 51 in Figure 3.7b. From this plot τ^δ could be obtained by the slope ($-1/\tau^\delta$), yielding the chemical diffusion coefficient (D^δ) from Eq. 52. In the present work, the sample thickness (L) was around 1 mm.

In addition to oxidizing conditions (from low to high pO_2 range), reducing conditions (from high to low pO_2 range) were used for annealed 0.3 % Cr-doped NiO in conductivity relaxation measurements. The measured data points and the measurement time for the reduction experiments were almost the same as for the oxidation experiments.

3.3. Sample Characterization

3.3.1. Inductively Coupled Plasma-Optical Emission Spectroscopy (ICP-OES)

The concentration of metal impurities was measured by inductively coupled plasma-optical emission spectroscopy (ICP-OES) with a Spectro Ciros CCD (*SPECTRO Analytical Instruments GmbH, Kleve*) in the analytical chemistry laboratory of Max Planck Institute for Intelligent Systems. The samples were dissolved in a mixture of HCl (37 %) and HNO₃ (65 %) with a ratio of 4:1 (HCl:HNO₃) at 175 °C for 3 hours or more for the analysis.

3.3.2. X-Ray Diffraction (XRD)

X-ray diffraction (XRD) using a *Panalytical Empyrean, Philips Diffractometer*, Cu $K_{\alpha}=1.54056 \text{ \AA}$ was applied for the thin films, powders and pellets in order to (i) identify the phases, (ii) obtain the crystallite size of the powders, (iii) check the homogeneity of the samples, (iv) determine the lattice constants. The diffractometer was operated in Bragg-Brentano geometry and the lattice parameters were obtained using the Topas-Software.

3.3.3. X-Ray Photoelectron Spectroscopy (XPS)

X-ray photoelectron spectroscopy (XPS) was used to determine the native oxide layer thickness of the metal films, and the Cr dopant concentration depth profile of the metallic and oxide films by argon ion sputtering (4 kV), assuming the same sputtering rate as for the thermally oxidized SiO₂ of 2 nm/min. XPS measurements were performed with the instrument *AXIS ULTRA* from *Kratos Analytical Ltd.* and peak positions are compared to the *NIST XPS* database.

3.3.4. SEM-FIB-TEM/EDX

Scanning electron microscopy (SEM) was used to (i) observe the surface of the thin metal films and the oxide films, (ii) determine the grain size of the metal and the oxide films, (iii) determine the grain size of the pellets. SEM analyses were performed with a *Zeiss Merlin* microscope in secondary electron detection mode. Transmission electron microscopy (TEM), high-resolution transmission electron microscopy (HR-TEM), and energy dispersive X-ray spectroscopy (EDX) analysis were performed to analyze the samples (the metal films, the partly and the fully oxidized films, and the pellets). TEM samples of the thin films were prepared by focused ion beam (FIB) under vision of a scanning electron microscope (*Zeiss Crossbeam 1540 ESB*), and the pellets were prepared with conventional sample preparation techniques (tripod polishing followed by Ar ion milling) for TEM/EDX analysis. Transmission electron microscopes, their characteristic properties and the purpose of the use are listed below.

Philips CM 200 microscope was used to observe the microstructure of the Ni metallic films, partially and fully oxidized Ni films on Al₂O₃ substrates. The microscope has a large tilting capability along A axis ($\pm 60^\circ$) and B axis ($\pm 30^\circ$). It was operated at 200 kV (LaB₆ as an electron gun) with a point to point resolution of 2.7 Å.

ZEISS 912 Omega and ZEISS SESAM microscopes were used to characterize Cr-doped NiO films and to see Cr segregation in the films. While the operating voltage was 120 kV (LaB₆) and the spatial resolution was 20 nm for the ZEISS 912 Omega, it was 200 kV (FEG Schottky Field Emission) for the ZEISS SESAM with a spatial resolution of 1 nm.

JEOL ARM200F – Probe Corrected (S)TEM with an EDX system was used to characterize Cr segregations in the oxide films and Cr distribution in the grains and grain boundaries of Cr-doped NiO pellets. The microscope was operated at 200 kV (Cold Field Emission) and chemical analysis of the samples was obtained by JEOL EDX system.

3.3.5. Raman Spectroscopy

Raman Spectroscopy was used to determine possible impurity phases and to check the dopant segregation in Cr-doped NiO ceramic samples. Raman spectra were obtained with a Labram V 010 single grating spectrometer (*Horiba Jobin Yvon GmbH, Bensheim*) in quasi-backscattering geometry using the linearly polarized 532 nm line of a diode laser with a 10 μm spot through a 50X microscope objective. The resolution of the spectrometer was about 1 cm^{-1} .

4. Results and Discussion

4.1. Oxidation Kinetics of Metal Films

During the oxidation of metal films on Al_2O_3 substrates in a tube furnace, the resistance changes were measured by electrical impedance spectroscopy and analyzed using an equivalent circuit model (see Figure 4.1). The oxide thicknesses which consider the molar volume difference between the metal and the metal oxide (see Table 4.1) were calculated from the resistance values. As a general rule, the Pilling-Bedworth ratio (PBR), which is the ratio of oxide molar volume to metal molar volume divided by the number of metal atoms per molecule of the oxide, should not exceed 2 and it should not be less than 1 in order to have good adhesion and mechanical compatibility between passivating oxide and underlying metal [29, 42]. The protective oxide layer which forms very rapidly on the metal surface and prevents the metal from further oxidation at room temperature is measured by XPS. It is thinner than 3 nm.

Table 4.1: Molar volume of the metals and the oxides, and Pilling-Bedworth ratio

metal	metal oxide	molar volume (cm^3/mol)		Pilling–Bedworth ratio (PBR)
		metal	metal oxide	
Al	Al_2O_3	9.99	24.87	1.24
Cr	Cr_2O_3	7.27	29.12	2.00
Ti	TiO_2	10.61	18.88	1.78
V	V_2O_5	8.49	39.79	2.34
Zn	ZnO	9.95	14.52	1.46
Ni	NiO	6.90	11.20	1.70
Co	CoO	6.62	11.64	1.76

Thin film oxidation as a function of time was measured by *in-situ* resistance measurement using impedance spectroscopy. The results of oxidation measurement of 20 nm Cr film are given as an example in Figure 4.1a which shows the impedance spectra of this film at 506 °C as a function of time. The metal film thickness decreased and the oxide film thickness increased with time because of the thermal oxidation of the film, therefore the resistance values increased. The impedance spectra were fitted with an equivalent circuit model and the resistance values were obtained as shown in Figure 4.1b.

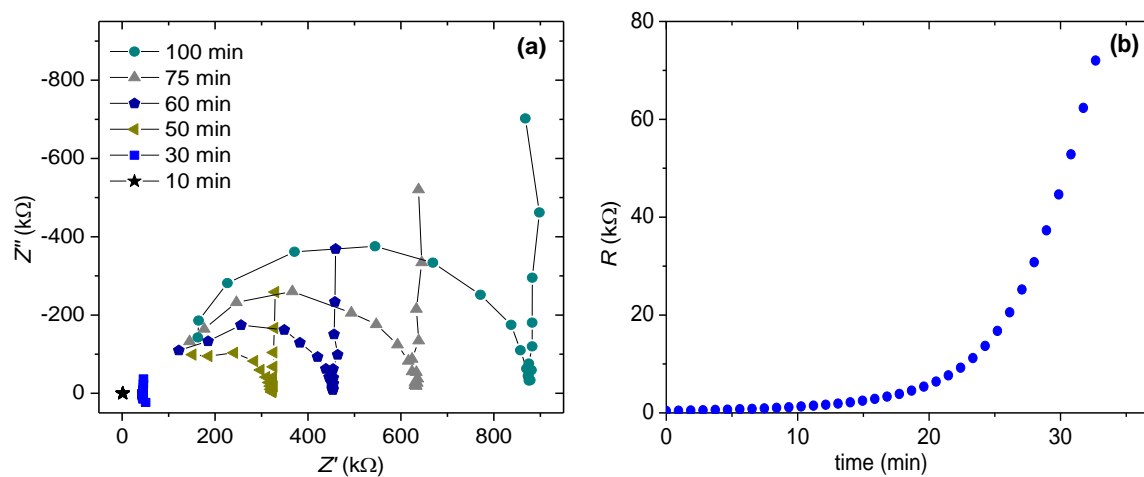


Figure 4.1: Results of impedance measurements of 20 nm Cr at 506 °C in air as a function of oxidation time: (a) Impedance spectra and (b) resistance values fitted from impedance spectra with an equivalent circuit.

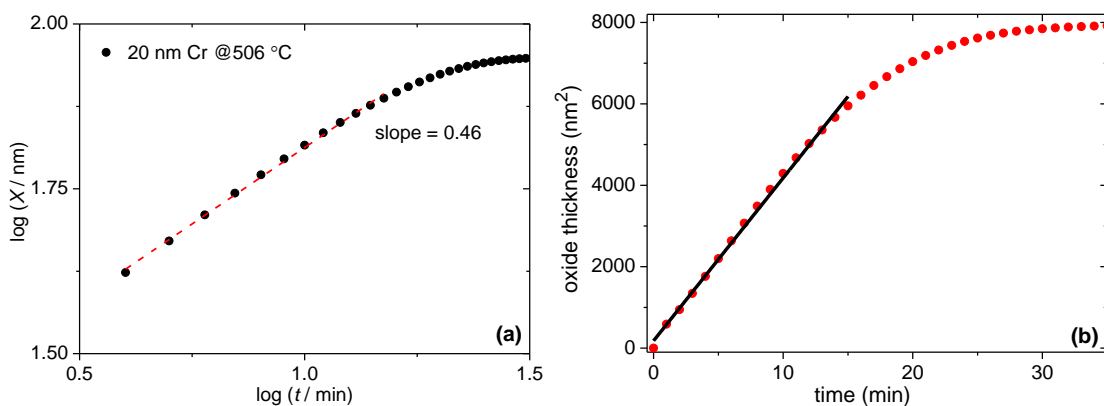


Figure 4.2: 20 nm Cr at 506 °C in air: (a) Oxide thickness plotted as a function of time, both on logarithmic scales, $\log X$ vs. $\log t$ and (b) calculated squared oxide thickness, X^2 vs. time.

The parabolic rate constant (or oxidation/reaction rate constant, k_p) can be fitted from the slope of X^2 vs. *time* according to parabolic rate law of oxidation using Eq. 40. If the reaction was surface controlled, the oxide film thickness would grow linearly in time and the slope of $\log X$ vs. $\log t$ would be 1 (see section 2.2.3). If the reaction was diffusion controlled, the oxide film would grow parabolically and the slope of $\log X$ vs. $\log t$ would be 0.5. The validity of the parabolic rate law for the samples in this work is confirmed by Figure 4.2a, which reveals the slope of 0.5 for $\log X$ vs. $\log t$.

The measurements of the oxidation kinetics showed that oxide growth follows the parabolic rate law for Cr, Al, Ti, V, Zn, Ni, and Co films with a thickness typically ranging from 10-150 nm and a temperature range between 200 and 500 °C. Thus, the rate determining process of the oxidation of these metal films is chemical diffusion through the oxide layer, following the prediction according to the Wagner theory [1, 3]. Details of the metal film oxidation experiments for different metals are presented in the following section.

4.1.1. Oxidation Kinetics of Different Metal Films

The oxidation kinetics of Cr, Al, Ti, V, Zn, Ni, and Co was measured for 50 nm thick polycrystalline metal films on polycrystalline Al_2O_3 substrates and the results are presented in Figure 4.3. Oxidation kinetics of the metals found to be diffusion controlled. The oxidation activation energies of the samples were obtained through the Arrhenius equation and are indicated in the figure. Within the 50 nm thick metal films, Co and Ni have the highest oxidation rate constants.

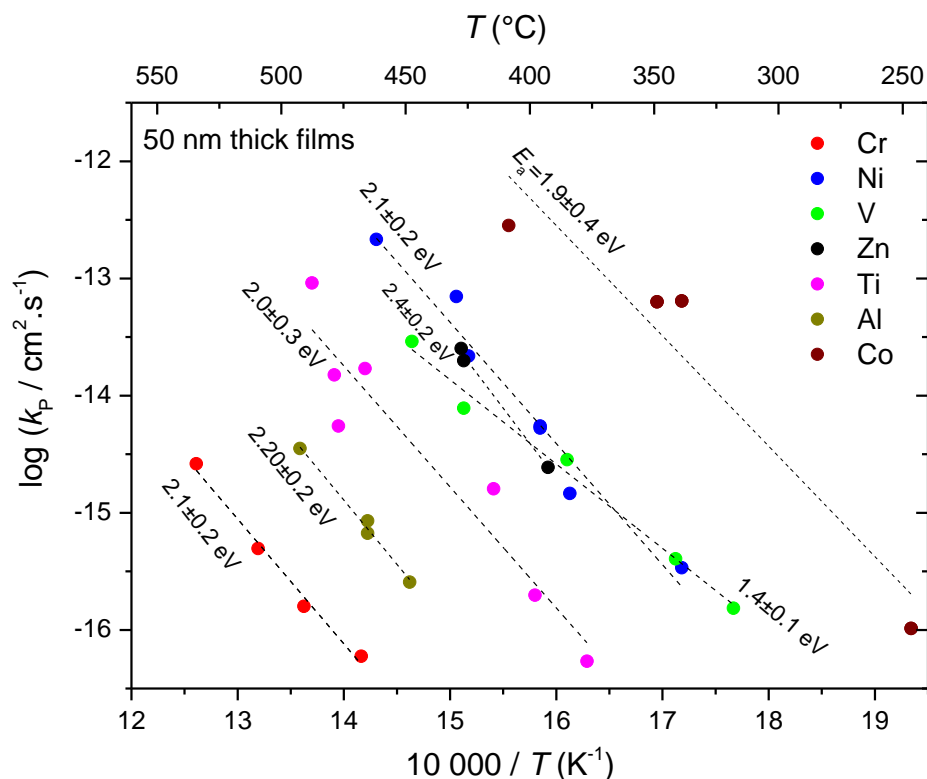


Figure 4.3: Comparison of the oxidation rate constants for different metal films as a function of reciprocal temperature. Oxidation kinetics of Ti is studied in Rastegar's MSc thesis [36].

Interestingly, according to Figure 4.3, the different metal films exhibit very similar activation energies. The literature values of the oxidation activation energies of these metals vary from 1.0 to 2.5 eV [6, 43, 44]. More on the scatter in the activation energies for Ni oxidation will be discussed in section 4.1.3. The activation energies measured in the present work are in the range of the literature values [6, 43, 44]. It is known from the literature that the activation energies for bulk and grain boundary diffusion differ. For instance, in the case of Ni oxidation, the bulk activation energy is 2.6 eV, while the grain boundary activation energy is 1.8 eV [34]. Since fast grain boundary diffusion is typically related to lower activation energies, the variation range of the activation energies is also expected to be lower. All films in this work have similar grain size and predominant cation diffusion. All these binary oxides have a 6-fold oxygen-coordination around the metal ions, and the structure comprises a close-packed or almost close-packed arrangement of oxide ions.

Although other factors cannot be excluded, the similar activation energies for different metal oxides found in this work might be related to the similar coordination of the cations in the bulk in combination with accelerated grain boundary diffusion.

The oxidation kinetics of Cr, Ni, and Co for 10 to 150 nm thick samples obeys the parabolic rate law. The different film thicknesses (metal film thickness limits the oxide film thickness) show essentially the same parabolic rate constant (Figure 4.4). This confirms the validity of the Wagner theory for the films in the 10-150 nm thickness range and for the temperature range shown in Figure 4.4 for each metal.

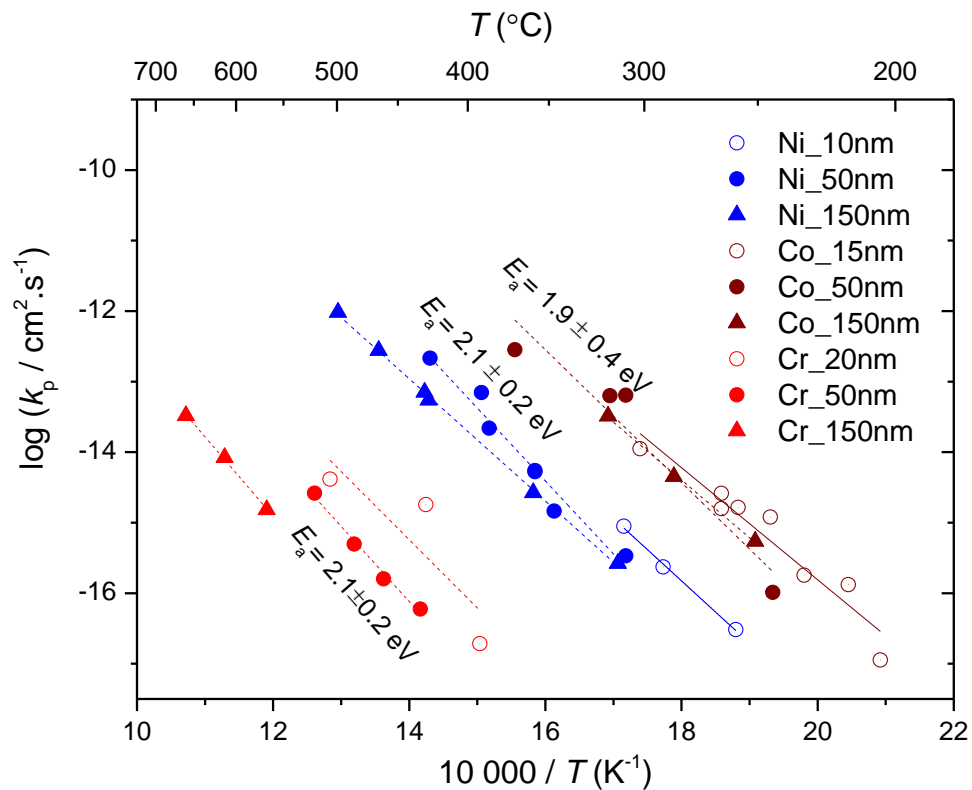


Figure 4.4: Comparison of the parabolic rate constants of Cr, Ni, and Co for sample thickness variations as a function of reciprocal temperature. The indicated values of E_a correspond to 50 nm thick films.

The NiO crystal structure is the same as that of CoO (rocksalt structure). Also, the defect chemistry of the two oxides is very similar [3]. The main difference is that CoO has defect concentrations that exceed the one of NiO by up to two orders of magnitude [3], therefore the cation diffusion is higher in CoO. This can be clearly seen in Figure 4.3 and Figure 4.4: Co films show two orders of magnitude higher oxidation rate constant than Ni films. This also indicates that the oxidation time (and thus the potential data storage speed) can be in the millisecond range for a 10 nm Co film at around 540 °C**. Table 4.2 shows the oxidation rate constants and the tracer diffusion coefficients required for a 10 nm thick metal film to achieve a specific oxidation time for possible data storage applications. The required k_p and D^* values are calculated from Eq. 40 and 44, respectively.

Table 4.2: Oxidation rate constants and tracer diffusion coefficients required for a 10 nm metal film for data storage applications

oxidation time (data writing time)	$\sim k_p$ required for 10 nm film (cm ² /s)	$\sim D_{Me}^*$ required for 10 nm film @500 °C (cm ² /s)
millisecond	10 ⁻⁹	3x10 ⁻¹¹
microsecond	10 ⁻⁶	3x10 ⁻⁸
nanosecond	10 ⁻³	3x10 ⁻⁵

It is noted that the thermal oxidation rate constant of Co at 540 °C yields an oxidation time of milliseconds, the rate at 540 °C being extrapolated from the data at lower temperatures (see Figure 4.4). Nevertheless, there is still a possibility to increase the oxidation rate constant by laser oxidation. The literature on laser oxidation of thin films states that, while thermal oxidation is controlled by diffusion coefficients of the growing oxide film, laser oxidation can involve non-linear heating effects, intensity of the laser beam, absorptivity (metal, oxide, and substrate) etc. as the rate controlling parameters [45, 46]. Although not pursued in this thesis, the literature indicates that laser oxidation could be a path worth investigating to enhance oxidation time below milliseconds.

** If the oxidation rate constants of the 50 nm thick Co film in Figure 4.4 were extrapolated to 540 °C, k_p would be 10⁻⁹ cm²/s, which corresponds to the oxidation time of millisecond as shown in Table 4.2.

4.1.2. Oxidation Kinetics of Nickel at Different Conditions

Ni exhibits one of highest oxidation rate constants (parabolic rate constant) among the studied metals (as shown in Figure 4.3) and NiO is one of the model materials for defect chemistry of binary oxides. Therefore, Ni was investigated in more details for the thin film oxidation, and attempts were made to increase the oxidation rate constant for potential data storage applications.

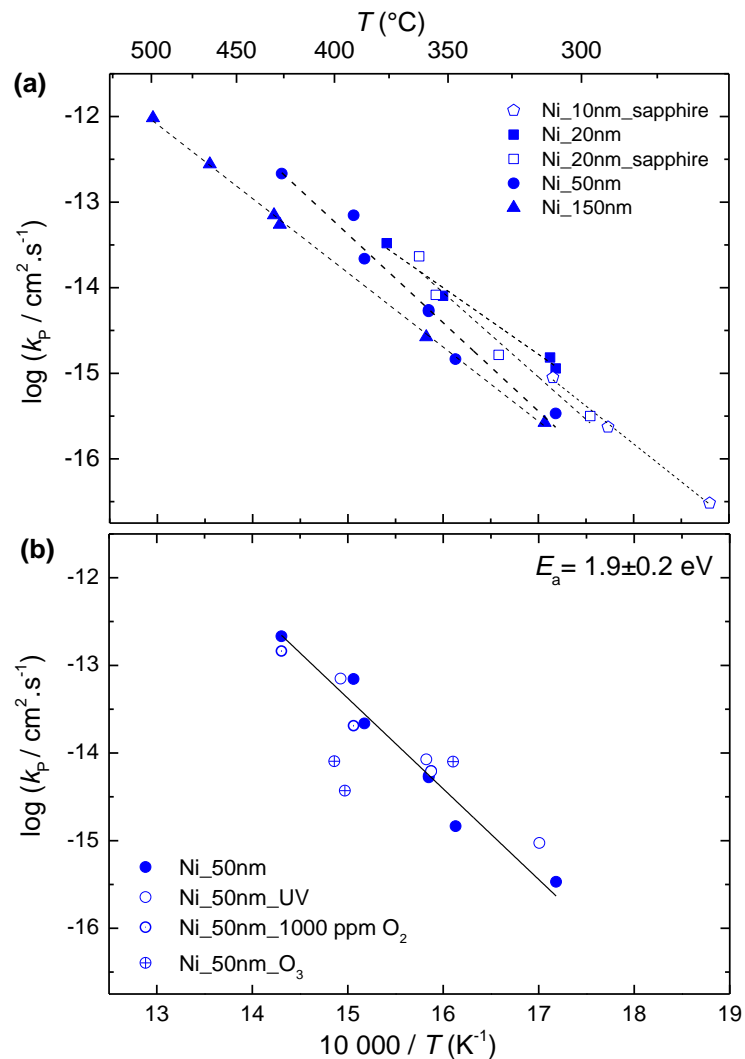


Figure 4.5: (a) Oxidation rate constants for different thicknesses of e-beam evaporated Ni films on polycrystalline Al_2O_3 or sapphire substrates in air, (b) oxidation rate constants for 50 nm Ni films on polycrystalline Al_2O_3 substrates under different experimental conditions (UV exposure, low $p\text{O}_2$, ozone atmosphere).

In order to clarify whether surface reaction plays a major role in the oxidation kinetics of Ni films, the oxidation measurements were performed under different experimental conditions. Ni films were oxidized for different thicknesses of the samples (compared to 50 nm), with different pO_2 , ozone atmosphere, and UV exposure to further confirm that the oxidation follows the parabolic rate law, *i.e.*, that it is diffusion controlled. The oxidation rate constants for films of different thicknesses and different substrates (polycrystalline or single crystalline Al_2O_3) yield almost the same values (Figure 4.5a). This confirms the validity of parabolic rate law of oxidation for the 10-150 nm thick Ni samples in the temperature range of 250-500 °C. Figure 4.5b indicates that the oxidation kinetics of Ni films was not significantly changed by applying 0.1 % oxygen partial pressure, the UV light exposure and the ozone atmosphere. These experiments confirmed that the oxidation kinetics of Ni is diffusion controlled because these diverse experimental conditions which are expected to accelerate (UV, O_3) or decelerate (low pO_2) the surface reaction did not change the overall oxidation rate constant.

The activation energies of oxidation for different film thicknesses and substrates are presented in Table 4.3. Although there is a slight difference in E_a between different sample thicknesses and substrate roughness (polycrystalline or single crystalline) as shown in Table 4.3, the values are in general consistent. As a result of the oxidation measurements, an average $E_a=1.9\pm 0.2$ eV is obtained for 50 nm thick Ni films including the experiments also at different experimental conditions such as different pO_2 , UV exposure, etc.

Table 4.3: Activation energy of the measured Ni films shown in Figure 4.5

activation energy (eV)	sample
1.7±0.1	150 nm Ni on polycrystalline substrate
2.1±0.2	50 nm Ni on polycrystalline substrate
1.5±0.1	20 nm Ni on polycrystalline substrate
2.0±0.3	20 nm Ni on sapphire substrate
1.8±0.1	10 nm Ni on sapphire substrate
1.9±0.2	50 nm Ni on polycrystalline substrate (average value for all 50 nm samples)

4.1.3. Literature on Cation Diffusion in Oxides

Numerous studies on Ni oxidation are reported in the literature [4, 8, 47-57]. The majority of research on Ni oxidation was performed at very high temperatures because of the high corrosion resistance of nickel. The temperature range was 200 to 500 °C in this work, whereas the literature studies were mainly performed at a temperature range between 500 and 1400 °C [52, 54, 58-62]. Some of these results from the literature [43, 52, 54, 57, 59] and the results from this work are illustrated in Figure 4.6. The scattering in the literature k_p reflects the influence of several factors on the oxidation of Ni: different impurities and impurity concentrations, the grain size of the growing oxide [3], the preparation techniques of the metal sample (annealed and cold worked) [63], the crystal orientation [64], etc. When extrapolated to higher temperatures, the oxidation rate constants of 50 nm thick Ni films in the present work show the highest oxidation rate constants as compared to the literature [43, 52, 54, 57, 59].

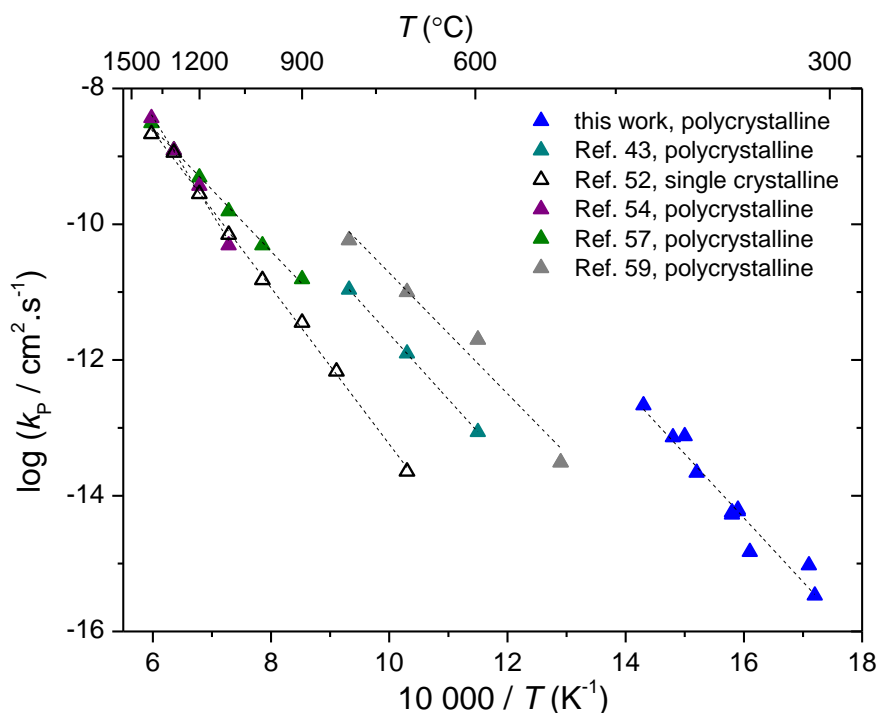


Figure 4.6: Comparison of the literature oxidation rate constant values for Ni [43, 52, 54, 57, 59] to those of in this work.

One has to note that the oxidation rate constant values for single crystalline samples in Atkinson's study were calculated from Eq. 44 using the Ni tracer diffusion coefficients of NiO which were measured by the sectioning technique at 0.21 atm pO_2 [52]. The literature results on the oxidation kinetics of polycrystalline samples presented in Figure 4.6 are measured by weight gain at 1 atm pO_2 [54, 57] and 0.21 atm pO_2 [43]. The oxidation kinetics of Ni is diffusion controlled, therefore it depends on point defect concentrations and pO_2 [28]. Nevertheless, the pO_2 dependence of Ni oxidation is weak (see section 2.1.3, 2.2.1 and Table 2.1) and the pO_2 range is small in the mentioned literature, thus the measurements in the literature and in the present work are comparable.

Polycrystalline samples show higher oxidation rate constants than single crystalline samples as revealed in Figure 4.6 for $T < 1000$ °C. The activation energy of k_p for single crystalline sample [52] is higher than for polycrystalline samples except for the result of Mrowec and Grzesik [54] which shows higher activation energy compared to other polycrystalline samples [52, 57-60], as listed in Table 4.4. The decrease in activation energy for polycrystalline Ni oxidation compared to single crystalline samples indicates the effects that grain boundaries have on oxidation, as they provide fast diffusion paths [3, 34]. For example, the activation energy in the study of Atkinson and Taylor is 2.6 eV for bulk diffusion, 2.0 eV for dislocation diffusion and 1.8 eV for grain boundary diffusion of Ni in NiO [34]. Although the values of the activation energies scatter in the literature, the present results (50 nm Ni) are in a good agreement with the published values (see Table 4.3 and Table 4.4), especially with Atkinson and Taylor's work (1.8 eV for grain boundary diffusion at 500-800 °C) [34]. Since the k_p in the present work is two orders of magnitude higher than for the large-grained polycrystalline samples in the literature [59], it reveals that density of grain boundaries and therefore grain size of the growing oxide are important for the oxidation kinetics.

Table 4.4: Activation energy of k_p for Ni oxidation in the literature and in this work.

activation energy (eV)	reference
1.9±0.2	this work, 50 nm thick films
1.9	[57]
2.5	[54]
2.0	[43]
2.2	[52]
1.6	[58]
1.6	[59]
1.8, 2.0, 2.6	[34]

For a more general picture on cation diffusion in different oxides, tracer diffusion coefficients data from the literature [24] and from the present work (D^* calculated from k_p) are presented in Figure 4.7.

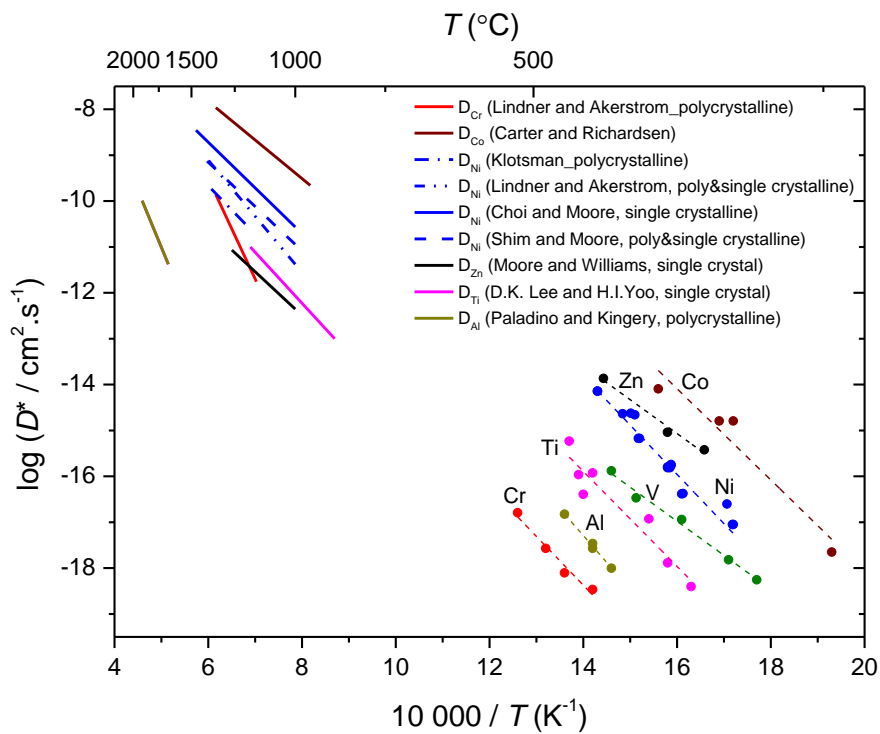


Figure 4.7: Cation tracer diffusion coefficients in binary oxides in the literature [24] and in this work. Symbols represent the present results, and the lines represent the literature results.

Figure 4.7 illustrates the tracer diffusion coefficients from the literature for several metal oxides which were also studied in the present work. For the present results, the tracer diffusion coefficients of cations in the growing oxide layer were calculated from the measured oxidation rate constants in this work using Eq. 44. One has to note that cation vacancies are predominant defects and D_M^* is much higher than D_O^* (tracer diffusion coefficient of oxygen) in most binary oxides. In the literature, the D_O^* values in NiO [65] are reported to be 5 to 7 orders of magnitude lower than the D_{Ni}^* values [52]. Also, the activation energy for D_O^* (5.7 eV) [65] is much higher than the activation energy for D_M^* (2.2 eV) [52] in NiO.

The sequence of D_M^* in the present work is very similar to the results found in the literature, and also the activation energies are in agreement with the literature except for Al and Cr. When the present results were extrapolated to the temperature range of the measurements in the literature, the tracer diffusion coefficient values of the present work are higher than those of in the literature. This can be related to the much smaller grain size of the samples in the present study. In the following section (4.1.4) the effect of the grain size on Ni diffusion in NiO will be explained in detail.

4.1.4. Grain Size Effect on Oxidation Rate & Diffusion

It is reported that Ni oxidation is controlled by bulk diffusion above ~ 1000 °C and by grain boundary diffusion at temperatures below ~ 1000 °C [4, 47]. The grain size of the growing oxide will consequently determine the density of fast diffusion paths for Ni in NiO during oxidation at the low temperatures studied in this work. The grain sizes of the metallic and the oxide layer were investigated by SEM and TEM in a 100 nm thick Ni sample which was partly oxidized. The TEM sample (Figure 4.8) was prepared by the FIB lamellae method. The grain size of the metallic layer is ~ 100 nm, whereas the grain size of the oxide layer is between 10 to 30 nm.

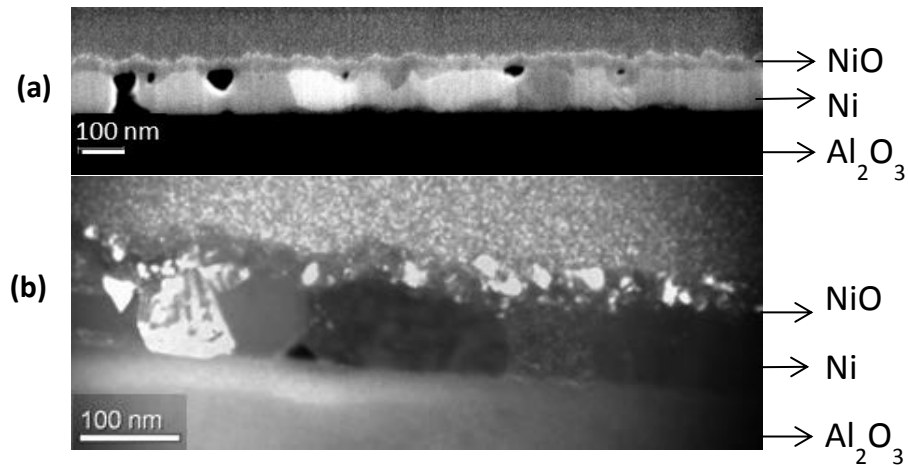


Figure 4.8: Cross-sectional images of the partly oxidized 100 nm Ni film (a) SEM and (b) TEM images.

The SEM image shows pores at the interface of the metallic and oxide layer. Those pores are mostly located at the end of the grain boundaries in the metal. As indicated in Figure 4.9 as a scheme of Ni oxidation, grain boundary diffusion of Ni in NiO is faster than bulk diffusion. The pore formation between the metal and metal oxide film may be viewed as a result of fast grain boundary diffusion of Ni in NiO exceeding the diffusion rate of Ni in Ni as indicated in Figure 4.9. More on the comparison of the diffusion coefficients of Ni in Ni and in NiO can be found in a literature study [66]. Furthermore one should also consider the possible contribution of a faceted shape of the metal grain to pore formation (a faceted instead of columnar shape lowers the free surface energy of the Ni crystallite). Additional reasons could be a volume difference between the metal and the oxide, and the fact that annealing, grain growth and possibly densification of the remaining metal phase occur during the ongoing oxidation process.

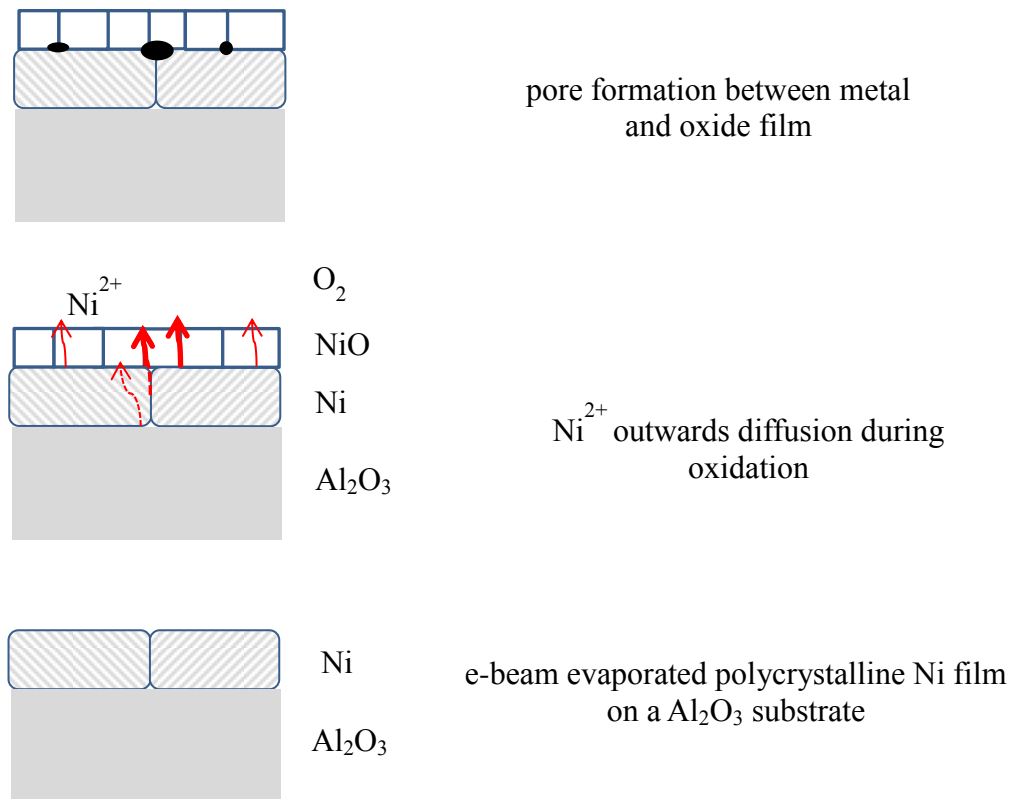


Figure 4.9: Sketch of fast grain boundary diffusion of Ni in Ni metal and in NiO during the oxidation and its effect on pore formation. Thick arrows represent fast Ni diffusion in NiO and dashed lines represent Ni diffusion in Ni.

Figure 4.10 illustrates D_{Ni}^* values for single crystalline NiO [52, 67, 68] and polycrystalline NiO [59] together with the results of this work for polycrystalline NiO with smaller grains. The figure clearly shows that samples with a smaller grain size have higher effective diffusion coefficients. Atkinson and Taylor studied single crystalline NiO samples [52, 68] and Atkinson, Taylor and Hughes studied polycrystalline NiO samples with a grain size of 1.39 μm at 800 $^\circ\text{C}$, 0.55 μm at 700 $^\circ\text{C}$, 0.37 μm at 600 $^\circ\text{C}$ and 0.16 μm at 500 $^\circ\text{C}$ [59]. There is an increase of the diffusion coefficients in the large-grained polycrystalline samples [59] compared to the single crystal samples at the temperature range from 500 to 800 $^\circ\text{C}$ in the literature [52, 68].

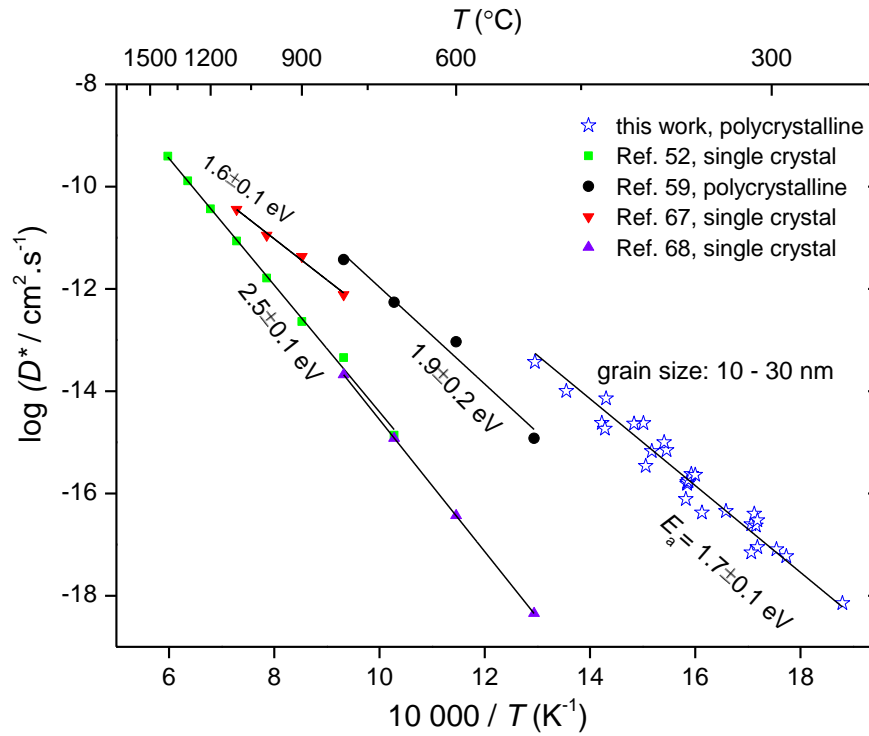


Figure 4.10: Comparison of D_{Ni}^* values of NiO samples: D_{Ni}^* values from the literature for single crystalline [52, 67, 68] and polycrystalline [59] NiO samples compared to those of in this work. D_{Ni}^* values in this work are extracted from k_p measurements using Eq. 44. D_{Ni}^* values were calculated in Ref. 68 from D_{Ni}^δ measurements.

A comparison of the diffusion coefficients in Figure 4.10 shows that polycrystalline samples [59] have higher oxidation rate constant than single crystalline samples [52, 68] and that among the polycrystalline samples those with a smaller grain size of 10-30 nm (this work) exhibit an increased diffusion coefficient. The effective diffusion coefficient in the present work increased from $\sim 10^{-18}$ to 10^{-13} cm^2/s at ~ 500 °C compared to single crystalline samples from literature [52, 68]. The effective diffusion coefficient in this work is also higher relative to the polycrystalline samples (grain size of 0.16 μm) [59] because of the increase in grain boundary density.

The tracer diffusion coefficient values from this work in Figure 4.10 are calculated by Eq. 44 from the measured oxidation rate constants and the $\Delta\mu_{\text{Me}}$ values are obtained by Eq. 45. In the calculations, thermodynamic parameters used from literature [44].

The effective diffusion coefficient is modeled assuming a parallel switching of bulk transport and grain boundary diffusion [69] according to

$$D_{\text{eff}}^* = gD_{\text{gb}}^* + (1-g) D_{\text{g}}^* \quad (53)$$

where D_{eff}^* is the effective diffusion coefficient, D_{gb}^* the grain boundary diffusion coefficient, D_{g}^* the grain (bulk) diffusion coefficient and g the volume fraction of grain boundaries. The thickness of the grain boundary (δ) is assumed to be 1 nm while the average grain size (d) is 20 nm as measured by TEM for the films in this work. g is calculated according to $g=q\delta/d$ using $q=2$ for the thin films (columnar grains; $q=1$ would correspond to a microstructure of vertical lamellae) [70] resulting in $g=0.1$. D_{eff}^* is the diffusion coefficient of the samples in this work. Literature D_{g}^* (Atkinson and Taylor [52]) is used for the calculation of D_{gb}^* , and the values are presented in Figure 4.11.

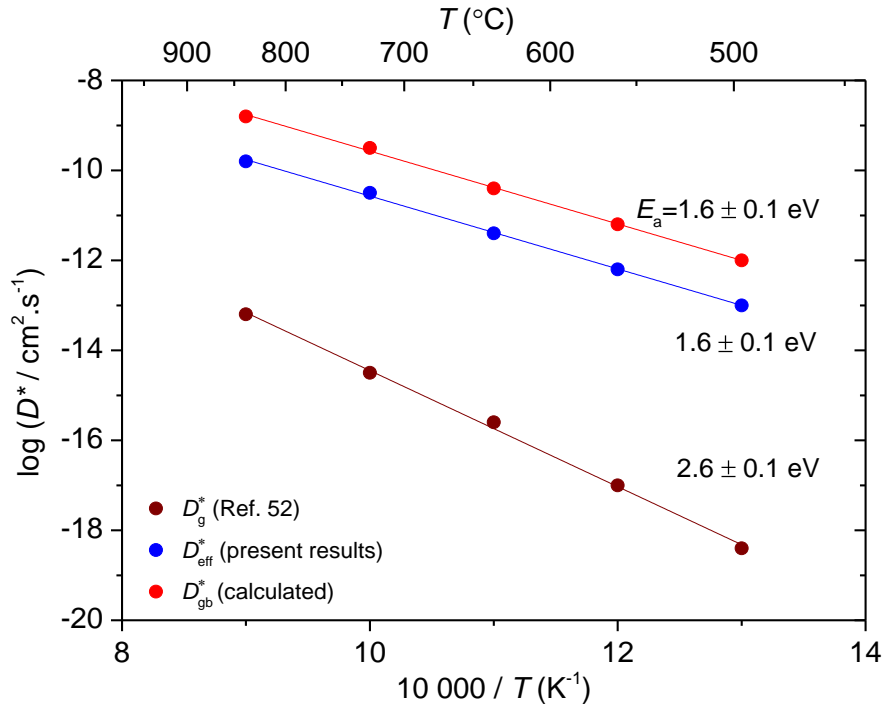


Figure 4.11: Comparison of the calculated grain boundary diffusion coefficients (D_{gb}^*) derived from Eq. 53, present results (D_{eff}^*) obtained using Eq. 44 and the bulk diffusion coefficient (D_{g}^*) extracted from literature [52].

The results of the calculation according to Eq. 53 show that in NiO the grain boundary diffusion coefficient is higher than the bulk diffusion coefficient by six orders of magnitude at 560 °C, as shown in Figure 4.11. The activation energy of the grain boundary diffusion coefficient is the same as for the effective diffusion coefficient. These results confirm that grain boundary diffusion is effective and grain boundaries control the diffusion of Ni in polycrystalline NiO samples. The reason for the increased oxidation rate constant of Ni and of the large diffusion coefficient of NiO in the investigated samples in this work is the smaller grain size of the samples as compared to the samples reported in the literature. The increased number of grains provides more diffusion paths for Ni diffusion.

The value of the calculated grain boundary diffusion coefficient in Figure 4.11 was checked for other polycrystalline samples. Calculated D_{gb}^* and D_g^* values [52] and a grain boundary thickness of 1 nm are used in the calculation of D_{eff}^* for a sample which has 0.16 μm grain size [59]. The obtained D_{eff}^* ($9.4 \times 10^{-14} \text{ cm}^2/\text{s}$ at 560 °C) and the measured diffusion coefficient ($1.8 \times 10^{-14} \text{ cm}^2/\text{s}$ at 560 °C) [59] are reasonably close to each other which shows that grain boundary transport properties of the thin films and the ceramics are very similar.

4.2. Oxidation Kinetics of Cr-doped Ni films

4.2.1. Oxidation Kinetics of e-Beam Evaporated Cr-doped Ni Films

As already mentioned in section 2.1.1.2, donor-doping in NiO (with Al⁺³, Cr⁺³, etc.) is expected to increase the nickel vacancy concentration and therefore to increase the reaction rate constant. NiO shows perceptible grain boundary diffusion at temperatures lower than 1000 °C [4, 71, 72]. In literature [4, 73], it is shown that Al presence leads to an increase of the oxidation rate constant via increased cation vacancy concentration above 1000 °C, but Al leads to a decrease in the oxidation rate constant below 1000 °C because of Al segregation to the grain boundaries. Although there is a similar result for Cr-Ni alloy at temperatures below 1000 °C [74], it is also reported that Cr increases the reaction rate constant of Ni at low temperatures (<1000 °C) if the Cr concentration does not exceed the solubility limit [47, 51, 71]. The solubility limit of Cr in NiO is reported in the literature as being ~1-2 % in the temperature range between 1000 and 1200 °C and lower at lower temperatures [74-77]. Cr was chosen as a donor dopant for NiO to increase the Ni diffusion. Because it is a trivalent cation, Cr³⁺ substituting for Ni²⁺, the Ni vacancy concentration is expected to increase as a result of the electroneutrality requirements in the oxide.

Therefore, the oxidation of Cr-doped Ni samples with low doping concentrations (0.1 and 1 % at.) was investigated with the intention to increase the reaction rate constant. Cr-doped Ni films did not show significant changes in oxidation rate constant compared to 50 nm Ni films as illustrated in Figure 4.12. Furthermore, 0.1 % Cr-doped Ni films were measured on polycrystalline Al₂O₃ and sapphire substrates for 50 and 12 nm film thicknesses and there was no significant change in k_p on changing the thickness or the substrate. As a result, Cr-doped Ni metallic films did not show an increase in the oxidation rate constant, as shown in Figure 4.12.

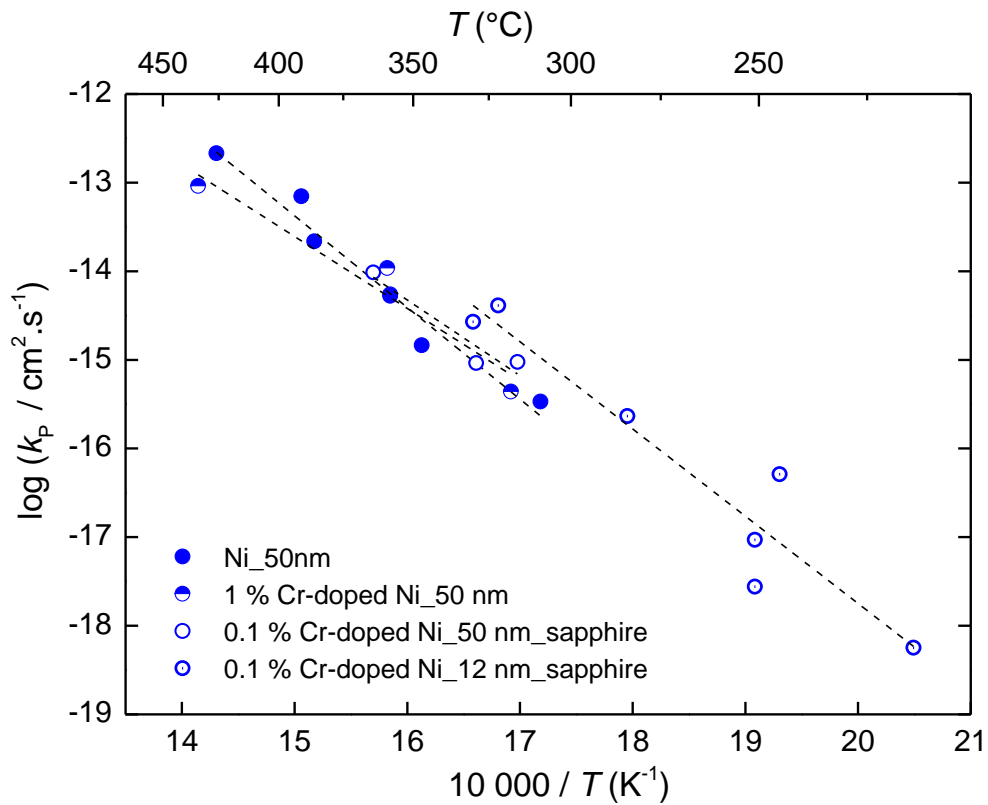


Figure 4.12: Comparison of the oxidation rate constants of 50 nm thick 1 % Cr-doped Ni films, 12 and 50 nm thick 0.1 % Cr-doped Ni films, and 50 nm (undoped) Ni films.

To understand the reason for the Cr dopant inactivity in the samples (in Figure 4.12), XPS and TEM analyses were performed.

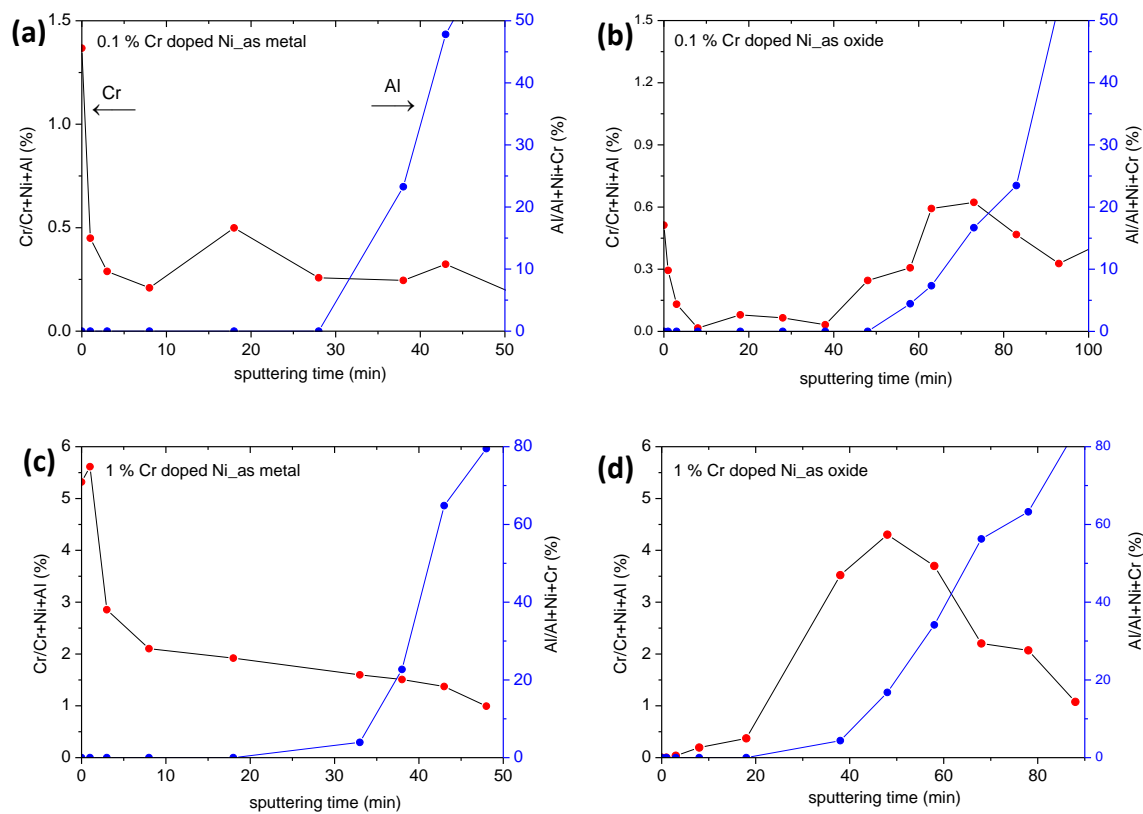


Figure 4.13: Concentration depth profile analysis by XPS: (a) 0.1 % Cr-doped Ni metal film, (b) 0.1 % Cr-doped Ni oxide film, (c) 1 % Cr-doped Ni metal film, and (d) 1 % Cr-doped Ni oxide film.

Concentration depth profiles of 0.1 and 1 % Cr-doped Ni samples before and after oxidation are analyzed by XPS (argon ion sputtering) and illustrated in Figure 4.13. The Al appearance in the figure indicates that in the course of sputtering the depth profile reaches the Al_2O_3 substrate. When Cr-doped Ni alloy is evaporated on the substrate, a Cr-rich surface layer forms on the metallic film. When the metallic film is oxidized, Cr segregates to the bottom of the sample (see also Figure 4.14). Obviously, Cr diffusion is slower than Ni diffusion in NiO which is also observed in the literature [78-80].

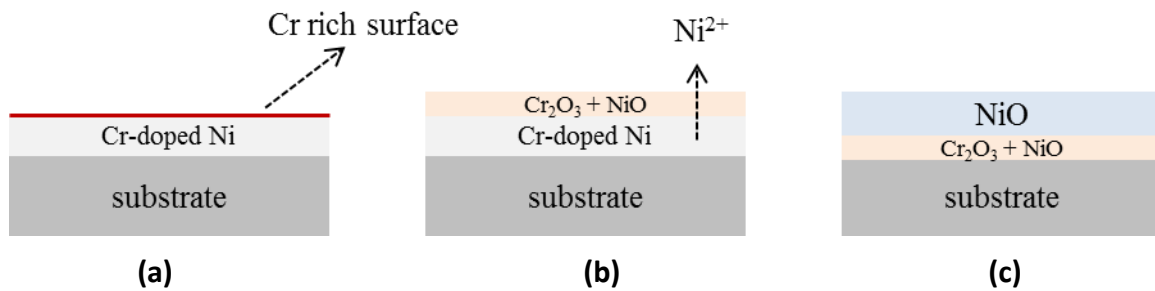


Figure 4.14: Cr-doped Ni film profile steps during oxidation: (a) As-prepared before oxidation, (b) during oxidation, and (c) after oxidation.

Figure 4.14 illustrates the different stages of the present Cr-doped Ni film oxidation. The first stage is characterized by a Cr-rich surface after e-beam evaporation and the second stage by Ni²⁺ outward diffusion through the NiO layer, leaving a Cr-rich oxide layer behind. These two steps lead to the final Cr profile. This result was confirmed by the TEM analysis presented in Figure 4.15. This figure illustrates the morphology of fully oxidized Cr-doped Ni films for 0.1 and 1 % Cr. The thickness of the Cr-rich bottom layer was enhanced by an increase in the Cr concentration. While the bottom layer is not easily visible in Figure 4.15a for 0.1 % Cr, the presence of a Cr-rich bottom layer is clear in Figure 4.15b for 1 % Cr concentration. Since evidently the Cr dopant is strongly depleted in most of the growing oxide layer, the Cr-doped Ni film showed very similar oxidation rate constant values to those of undoped Ni films.

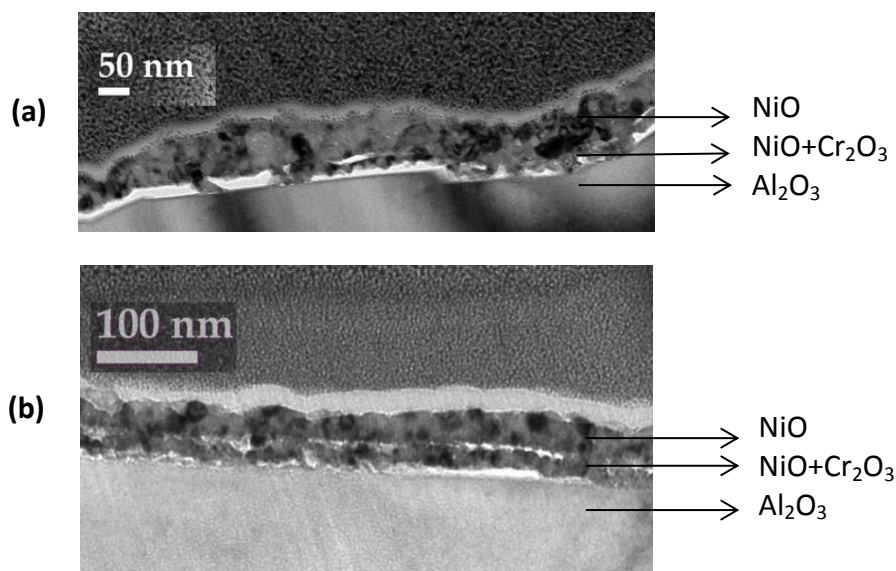


Figure 4.15: Cross-sectional TEM image of (a) 0.1 % Cr-doped NiO and (b) 1 % Cr-doped NiO.

Since Cr₂O₃ has a significantly higher negative standard free energy of formation than NiO, Cr is expected to segregate to the surface of the samples. XPS depth profile showed indeed that there is an enhanced amount of Cr on the sample surface as observed for the first data points. The native oxide layer on 1 % Cr-doped Ni film surface is almost identical to the Cr-rich surface in Figure 4.14a. Most probably Cr₂O₃ and NiO phases separate at the surface because of the solubility limit of Cr in NiO.

4.2.2. Oxidation Kinetics of Magnetron Sputtered Cr-doped Ni films

Magnetron sputtered Cr-doped Ni films were prepared at two different substrate temperatures: 25 °C and 400 °C. The oxidation kinetics of these samples was measured and compared to 50 nm Ni samples prepared by e-beam evaporation. The oxidation rate constant of the magnetron sputtered samples (Figure 4.16a) showed no significant change as compared to that of the e-beam evaporated samples. Different substrate temperatures for magnetron sputtering did not affect the oxidation kinetics.

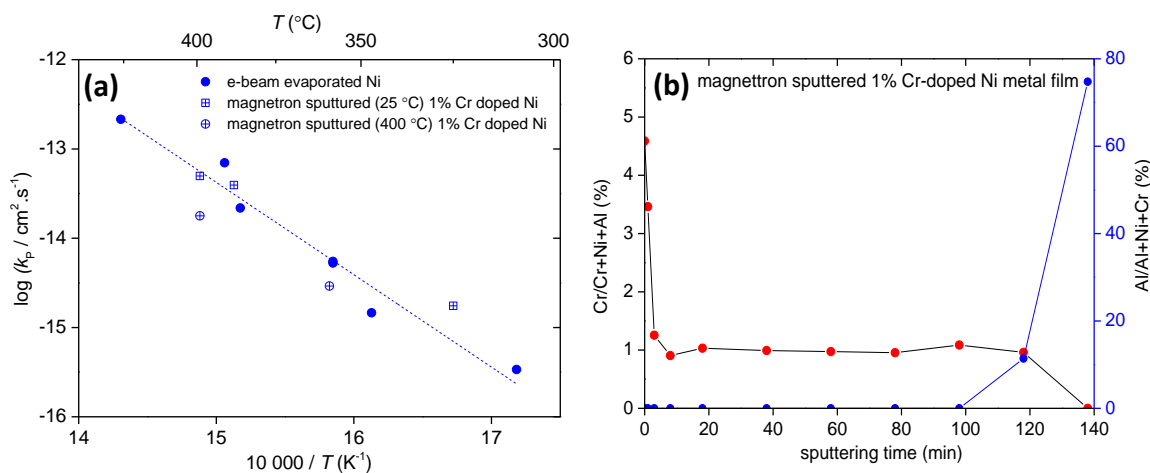


Figure 4.16: (a) Oxidation rate constants of magnetron-sputtered Cr-doped Ni films compared to those of e-beam evaporated Ni films, (b) XPS depth profile of magnetron sputtered film for a metallic form.

The XPS depth profile (Figure 4.16b) of the magnetron sputtered film (at a substrate temperature of 400 °C) showed that Cr was not homogeneously distributed through the sample. Although the Cr concentration stabilizes right after the 3rd data point of the XPS analysis, a high concentration of Cr on the sample surface appears which is very similar to the characteristic of e-beam evaporated samples. These results reveal that similar difficulties as in the e-beam evaporation for preparing doped films with homogeneous Cr distribution also arise for the samples which were grown by magnetron sputtering.

4.2.3. Oxidation Kinetics of PLD Grown Cr-doped Ni films

As an alternative sample growth technique, PLD was used at substrate temperatures of 25 °C and -180 °C to grow 1 % Cr-doped Ni thin film from the same alloy which was used in e-beam evaporation. The difference between the samples which were grown at 25 °C and -180 °C was the amount of Cr accumulation on the film surface. While the sample grown at 25 °C has 3 % Cr accumulation on the sample surface, the sample grown at -180 °C exhibits 2 % Cr accumulation as shown in Figure 4.17b, and already after the 2nd data point, the Cr distribution seems homogeneous and close to the desired dopant concentration (1 % Cr).

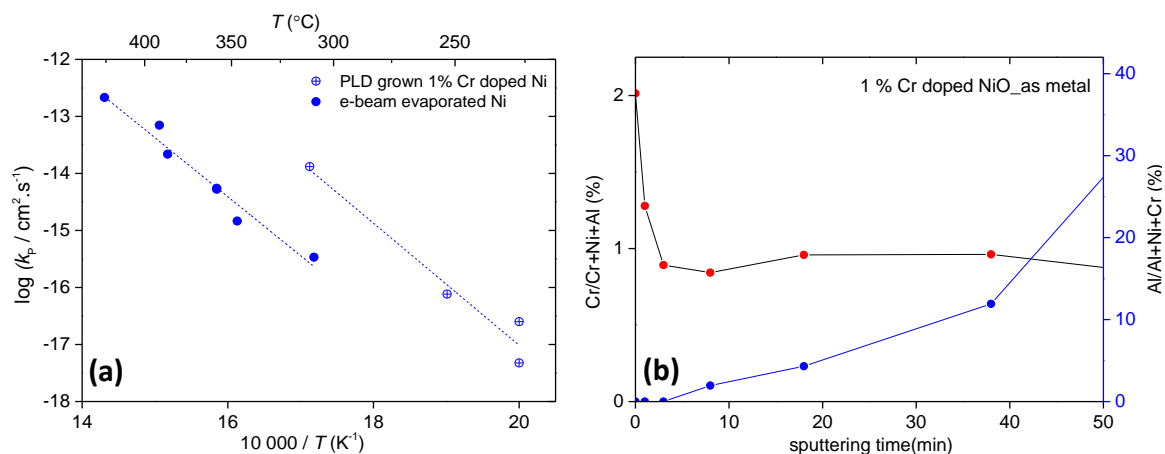


Figure 4.17: a) Oxidation rate constants of PLD grown Cr-doped Ni films at a substrate temperature of -180°C compared to e-beam evaporated (undoped) Ni films, b) XPS analysis of the PLD grown Cr-doped Ni film.

This behavior implies that low-temperature PLD growth provides better samples in terms of homogeneous distribution of Cr-dopant through the sample in comparison to e-beam evaporation of the same alloy. Therefore, the PLD grown samples at a substrate temperature of -180°C were used for the oxidation experiments. The results in Figure 4.17a showed that PLD growth provides an increase of the oxidation rate constant by two orders of magnitude.

From the defect chemical considerations in section 2.1.1, 1 % Cr doping is expected to increase the vacancy concentration by more than two orders of magnitude if really all Cr is active as a dopant. Nevertheless, compared to other growth techniques such as e-beam evaporation and magnetron sputtering, PLD grown samples at low substrate temperature (-180°C) are promising.

One should note, however, that the PLD grown films are not homogeneous in thickness, the thinnest region was measured to be ~ 20 nm by SEM, which was the value used to extract the oxidation rate constants (a larger thickness would lead to higher values of k_p). Therefore, the illustrated oxidation rate constants of PLD grown samples in Figure 4.17 should be considered as preliminary results. A careful control of the PLD-grown sample

thickness would be required to assess the full potential of this growth technique, which is outside of the scope of this work.

4.2.4. Concluding Discussion on the Ni Film Oxidation

The rate determining process for the oxidation of 50 nm Cr, Al, Ti, V, Zn, Ni, and Co films is found to be chemical diffusion through the oxide layer according to the Wagner theory of oxidation. Co and Ni have a higher oxide growth rate than Cr, Al, Ti, V, and Zn. The oxidation rate constant of Cr, Ni, and Co is not changed by applying different experimental conditions, changing thickness and substrates. This confirms the validity of the parabolic rate law of oxidation for the samples thicker than 10 nm at temperatures below 500 °C. The increased diffusion coefficients for samples with much smaller oxide grain size compared to the literature show the importance of fast grain boundary diffusion in this temperature range. There is a possibility to increase the reaction rate constant by doping NiO with Cr at low concentration (less than 1 % at.). But the present results showed that obtaining a homogeneous distribution of Cr through the metal thin films is not an easy task, only PLD grown samples are promising in this respect. Furthermore, Cr is accumulated at the bottom of the grown NiO film, indicating a lower diffusivity of Cr compared to Ni in NiO. Regarding the desired millisecond oxidation speed for a potential data storage application, from the Arrhenius plot of oxidation rate constant, for a 10 nm Co film temperatures of ~540 °C and for a 10 nm Ni film of ~650 °C can be extrapolated.

If, on the other hand, the oxidation of thin metal films was surface reaction controlled, one could increase the reaction rate by using UV illumination, O₃ atmosphere, high pO₂, etc. But since the oxidation is diffusion controlled for the samples in this work (10-150 nm, at 200-500 °C), one can only try doping to increase the relevant defect concentration which was shown to be difficult for thin films in the present work. Additionally, one can try decreasing the grain size in the growing oxide film to increase the contribution from fast grain boundary diffusion, but controlling the grain size in a growing oxide is also not an easy task, in particular, when the samples, as in this work, already have very small grains (10-30 nm).

The kinetics of oxygen stoichiometry change (small modification of oxygen stoichiometry in an oxide or complete oxidation) is expected to change from diffusion controlled to surface reaction controlled below a certain critical thickness. The borderline between diffusion control and surface reaction control is given by $k^\delta \cdot l_c \approx D$ (k^δ : surface reaction rate, l_c : critical sample thickness, D : diffusion coefficient), where l_c is typically between 1 to 100 μm for mixed conducting perovskites [81] (note that this criterion was derived for experiments in which only a small driving force is applied). Although the lowest sample thickness was 10 nm in the present work, a change from diffusion control to surface reaction control was not observed.

Therefore the question arises why the formation of such very thin binary oxide layers is still diffusion controlled. The main reason of this is shown in Figure 4.18. While the diffusivity (D_O^* for perovskites, D_M^* for NiO) is high in perovskites [82, 83], it is low in NiO. The surface reaction rate is not known for NiO, therefore l_c could not be directly calculated. But assuming a roughly comparable k^δ as for the perovskites, l_c would be lower than the typical values by orders of magnitude for NiO because of the much lower D^* . This explains why the parabolic rate law is valid even for 10 nm oxidized Ni film at 250 $^\circ\text{C}$.

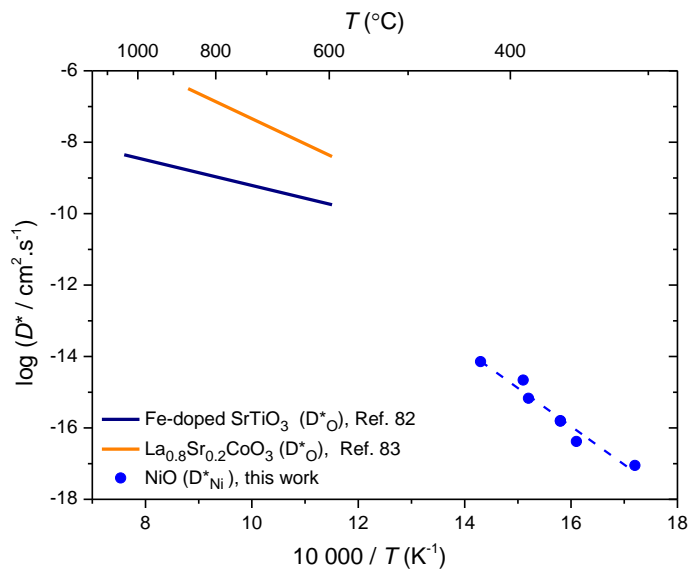


Figure 4.18: Comparison of diffusion coefficients: D_M^* in NiO (present results) vs. D_O^* in perovskites [82, 83].

4.3. Chemical Diffusion Coefficient of Undoped and Cr-doped NiO Ceramics (Conductivity Relaxation Measurements)

The studies of the oxidation kinetics measurements showed that the oxidation rate constants of the metal films are not in the desired range for data storage applications, as specified by the requirements given in Table 4.2 (last two rows of the table). Cr doping in the Ni films aimed at increasing the diffusion coefficient via increasing defect concentrations was not successful largely because Cr was not homogeneously distributed in the growing oxide film. With the objective of achieving a homogeneous Cr distribution and enhanced chemical diffusion, Cr-doped NiO ceramic samples were studied with the variation of grain size. The aim of the conductivity relaxation measurements of undoped and Cr-doped NiO ceramics is to understand the Cr doping effect on transport properties of the ceramic samples as a function of Cr concentration and grain size. Before investigating the transport properties of undoped and Cr-doped NiO, XRD analyses were performed on the ceramic samples to check for the presence of undesired phases after pellet preparation.

4.3.1. XRD Analyses of Undoped and Cr-doped NiO Ceramics

Undoped and Cr-doped NiO powders were synthesized and compacted by SPS (termed “as-prepared”) and some of them were annealed at 1500 °C for 8 hours (termed “annealed”). Figure 4.19 illustrates the XRD diffraction patterns of the as-prepared and annealed ceramic samples for undoped and Cr-doped NiO.

Since the solubility limit of Cr in NiO is around 1 to 2 % at 1000 °C according to the literature [74-77], the presence of NiCr₂O₄ spinel and Cr₂O₃ phases was checked, with special attention given to the 1 and 3 % Cr-doped ceramic samples. Figure 4.19 shows that no XRD peaks of additional phases were found in addition to the NiO peaks for all compositions (0.1, 0.3, 1 and 3 % Cr) and heat treatments. The strongest XRD diffraction peaks should appear at 2θ degrees of 33°, 35.5° and 55.5° for Cr₂O₃ [84] and at 36° for NiCr₂O₄ [85]. They are not observed as shown in Figure 4.19.

Although there is no undesired phase formation according to the XRD results, the peak splitting seen in addition to the K_{a1} , K_{a2} peaks indicates a deviation from perfect cubic symmetry. Antiferromagnetic nickel oxide was first assigned to have a face-centered cubic rocksalt structure [86], but further investigations showed that it is slightly rhombohedrally distorted [87]. The departure from cubic symmetry gradually decreases with increasing temperature and finally disappears above 527 K (Neel temperature of NiO, T_N) [88]. This distortion is related to the atomic size ratio of nickel to oxygen, which is too small to maintain the perfect face centered cubic structure of NiO at room temperature [89]. Besides, it was also observed that FeO (10 wt %) and CoO (5 wt %) dissolution in NiO where the additional ions have a larger atomic radius than nickel, decreased the distortion [89]. Further research on NiO revealed that the lattice deformation is due to spontaneous magnetostriction [90] and the ultimate symmetry of NiO in the antiferromagnetic state is monoclinic [91]. Since the lattice constant change and peak splitting in the present undoped and doped NiO samples are not correlated in a simple way with either the dopant concentration or the heat treatments, the main source of the observed peak splitting cannot be addressed straightforwardly.

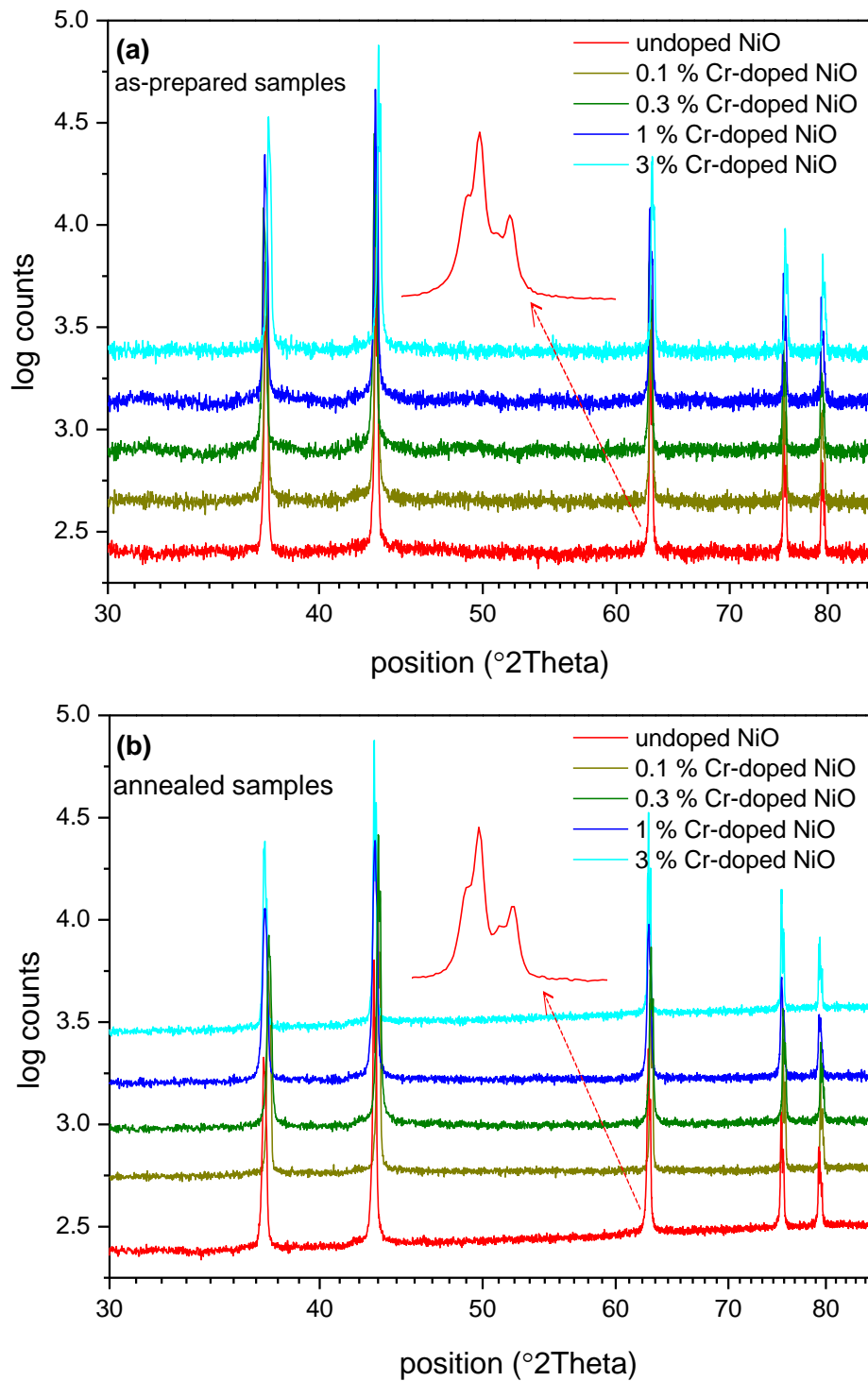


Figure 4.19: XRD analyses of undoped and Cr-doped NiO: (a) As-prepared ceramic samples, (b) annealed ceramic samples at 1500 $^{\circ}\text{C}$ for 8 hours. The diffractograms are shifted vertically and plotted on logarithmic scales for clarity.

4.3.2. Grain Boundary Blocking Effect

Before investigating the stoichiometry relaxation of the ceramic samples, it was checked if the grain boundaries are blocking the conductivity. Typically, additional semicircles in impedance spectra caused by blocking grain boundaries vanish at high temperatures. Therefore, the measurements were performed at lower temperatures than usual measurement temperatures (500 - 800 °C). Figure 4.20 shows representative spectra obtained for an as-prepared 0.1 % Cr-doped NiO (at 200 °C) and an annealed 1 % Cr-doped NiO (at 300 °C) samples. These samples were chosen to represent different annealing conditions and different Cr concentrations.

The measurements were performed in the frequency range of 1×10^7 to 3×10^{-2} Hz. There is only one semicircle for both samples, which represents the bulk conductivity as shown in Figure 4.20. Since there is no second semicircle in the low-frequency range and also the values of the calculated dielectric constant (23 and 26, respectively) correspond to bulk values, it was confirmed that there is no grain boundary blocking effect for Cr-doped NiO ceramic samples. This implies that there is no positive excess charge in the grain boundary core which would decrease the electron-hole conductivity by space charge depletion zones. Correspondingly, there is no accumulation of nickel vacancies in space charge zones adjacent to the grain boundary cores. Still, fast nickel vacancy diffusion is possible in the grain boundary core which is structurally different than from bulk. Furthermore, from the impedance spectra, it is not possible to conclude if there is an increased electronic conductivity parallel to the grain boundaries.

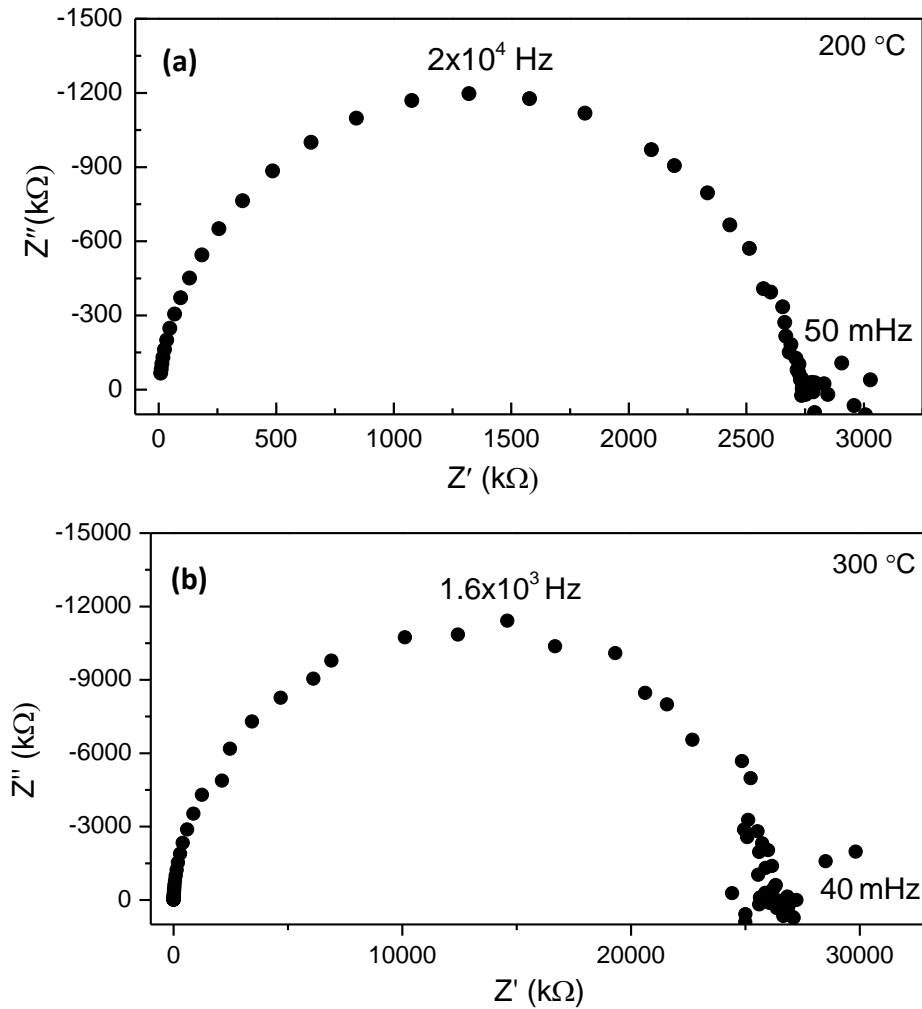


Figure 4.20: Impedance spectra of (a) the as-prepared 0.1 % Cr-doped NiO ceramic sample at 200 °C and (b) the annealed 1 % Cr-doped NiO ceramic sample at 300 °C.

4.3.3. Partial Pressure and Temperature Dependence of σ and D^δ

Conductivity measurements at various T and pO_2 and the corresponding conductivity relaxation experiments were performed for ceramic NiO samples with different Cr doping content and temperature treatment (see section 3.2 for the experimental details). The resulting conductivity (σ) and chemical diffusion coefficient (D^δ) are interpreted in this section in terms of a defect-chemical model. Before the explanation of the results, the summary of the defect-chemical model of NiO is repeated in Table 4.5 for convenience (for details, see section 2.1.1).

Table 4.5: Summary of defect chemical models of undoped and doped NiO (repeated from Table 2.1 to ease reading)

	if $[V''_{Ni}]$ is predominant	if $[V'_{Ni}]$ is predominant
undoped NiO	$2[V''_{Ni}] = [h^\bullet]$	$[V'_{Ni}] = [h^\bullet]$
	$K_1 = [V''_{Ni}][h^\bullet]^2/pO_2^{1/2}$	$K_2 = [V'_{Ni}][h^\bullet]/pO_2^{1/2}$
	$\sigma_{h^\bullet} = 2^{4/3}Fu_p^0T^{-1}\exp\left(-\frac{\Delta H_1^0/3 + \Delta H_p^m}{kT}\right)\exp\left(\frac{\Delta S_1^0}{3k}\right)pO_2^{1/6}$	$\sigma_{h^\bullet} = 2Fu_p^0T^{-1}\exp\left(-\frac{\Delta H_2^0/2 + \Delta H_p^m}{kT}\right)\exp\left(\frac{\Delta S_2^0}{2k}\right)pO_2^{1/4}$
	$E_\sigma = \Delta H_1^0/3 + \Delta H_p^m$	$E_\sigma = \Delta H_2^0/2 + \Delta H_p^m$
	$D_{Ni}^\delta = 3D_{V''_{Ni}}$	$D_{Ni}^\delta = 2D_{V'_{Ni}}$
	$[V''_{Ni}] \propto [h^\bullet] \propto pO_2^{1/6}$	$[V'_{Ni}] = [h^\bullet] \propto pO_2^{1/4}$
donor-doped NiO	$2[V''_{Ni}] = [D_{Ni}^\bullet]$	$[V'_{Ni}] = [D_{Ni}^\bullet]$
	$K_1 = [D_{Ni}^\bullet][h^\bullet]^2/2pO_2^{1/2}$	$K_2 = [D_{Ni}^\bullet][h^\bullet]/pO_2^{1/2}$
	$\sigma_{h^\bullet} = 2^{3/2}Fu_p^0T^{-1}\exp\left(-\frac{\Delta H_1^0/2 + \Delta H_p^m}{kT}\right)\exp\left(\frac{\Delta S_1^0}{2k}\right)\frac{pO_2^{1/4}}{[D_{Ni}^\bullet]^{1/2}}$	$\sigma_{h^\bullet} = 2Fu_p^0T^{-1}\exp\left(-\frac{\Delta H_2^0 + \Delta H_p^m}{kT}\right)\exp\left(\frac{\Delta S_2^0}{k}\right)\frac{pO_2^{1/2}}{[D_{Ni}^\bullet]}$
	$E_\sigma = \Delta H_1^0/2 + \Delta H_p^m$	$E_\sigma = \Delta H_2^0 + \Delta H_p^m$
	$D_{Ni}^\delta = D_{V''_{Ni}} \cdot \left(1 + \frac{2[D_{Ni}^\bullet]}{[h^\bullet]}\right)$	$D_{Ni}^\delta = D_{V'_{Ni}} \cdot \left(1 + \frac{[D_{Ni}^\bullet]}{[h^\bullet]}\right)$
$[h^\bullet] \propto pO_2^{1/4}$ and $D_{Ni}^\delta \propto pO_2^{-1/4}$ *	$[h^\bullet] \propto pO_2^{1/2}$ and $D_{Ni}^\delta \propto pO_2^{-1/2}$ *	
acceptor-doped NiO	$[h^\bullet] = [A'_{Ni}] = \text{constant}$	$[h^\bullet] = [A'_{Ni}] = \text{constant}$
	$K_1 = [A'_{Ni}]^2[V''_{Ni}]/pO_2^{1/2}$	$K_2 = [A'_{Ni}][V'_{Ni}]/pO_2^{1/2}$
	$\sigma_{h^\bullet} = 2Fu_p^0T^{-1}\exp\left(-\frac{\Delta H_p^m}{kT}\right)[h^\bullet]$	$\sigma_{h^\bullet} = 2Fu_p^0T^{-1}\exp\left(-\frac{\Delta H_p^m}{kT}\right)[h^\bullet]$
	$E_\sigma = \Delta H_p^m$	$E_\sigma = \Delta H_p^m$
	$D_{Ni}^\delta = D_{V''_{Ni}}$	$D_{Ni}^\delta = D_{V'_{Ni}}$
	$[V''_{Ni}] \propto pO_2^{1/2}$	$[V'_{Ni}] \propto pO_2^{1/2}$

 *: the relation is only valid for $[D_{Ni}^\bullet] \gg [h^\bullet]$

For as-prepared and annealed samples, the partial pressure and temperature dependences of the conductivity and of the chemical diffusion coefficients are presented in the following sections as a function of Cr dopant concentration. The ionization degree of predominant cation defects in NiO are not clear in the literature [25, 92, 93] and may also vary with T , pO_2 , and doping (see section 2.1.1). For this reason, both singly and doubly ionized nickel vacancies are considered. The slopes of the partial pressure dependence of conductivity and chemical diffusion coefficients provide information about the predominant defect type and the dopant activity in the sample. For example, if it was assumed that doubly ionized nickel vacancies were the dominant defects in undoped NiO, the pO_2 dependence of conductivity would be expected to be $1/6$ and the chemical diffusion coefficient to be pO_2 independent.

Two main temperature treatments were used for NiO ceramic samples; they are referred to as annealed and as-prepared samples. The main purpose of the heat treatment was to change the grain size. As-prepared samples have a smaller grain size (0.2-1 μm) compared to annealed samples (2-20 μm , further information in Table 3.5). Smaller grains provide more diffusion paths for Ni diffusion along the grain boundaries and therefore can enhance the chemical diffusion (coefficient). The results of annealed and as-prepared samples are presented in detail in sections 4.3.6 and 4.3.7. However, as discussed in the following sections, the annealing has additional effects (activation of dopants, influence on Cr segregation), which further complicates the picture.

In the following sections of this chapter the terms “*active*” and “*not active*” will be used to describe the effects of Cr in NiO. Cr dopant referred to as “*active*” (or “*activated*” and similar terms), indicate the case in which the results of σ and D^δ reflect the influence of Cr as a donor dopant. “*Inactive*” (or “*not activated*” and similar terms) are used for the opposite case when no influence of Cr doping is observed. As a matter of fact, the effect of Cr doping was only observed for annealed samples and not in as-prepared samples. There can be two possible reasons for this: (i) Cr could be in the divalent state instead of trivalent state as a result of the reducing atmosphere under which the Cr-doped NiO pellets are

compacted by SPS, (ii) Cr ions could be located in sites other than in Ni substitutional sites in the lattice. The annealing process (1500 °C - 8 h) after the SPS pellet preparation could then help to transform Cr^{2+} to Cr^{3+} and/or provide sufficient mobility for Cr to substitute Ni site as the thermodynamic stable state, in either case making Cr act as a donor dopant.

4.3.3.1. As-prepared samples

The temperature and $p\text{O}_2$ dependence of conductivity and chemical diffusion coefficient for as-prepared undoped and Cr-doped NiO samples are presented in Figure 4.21.

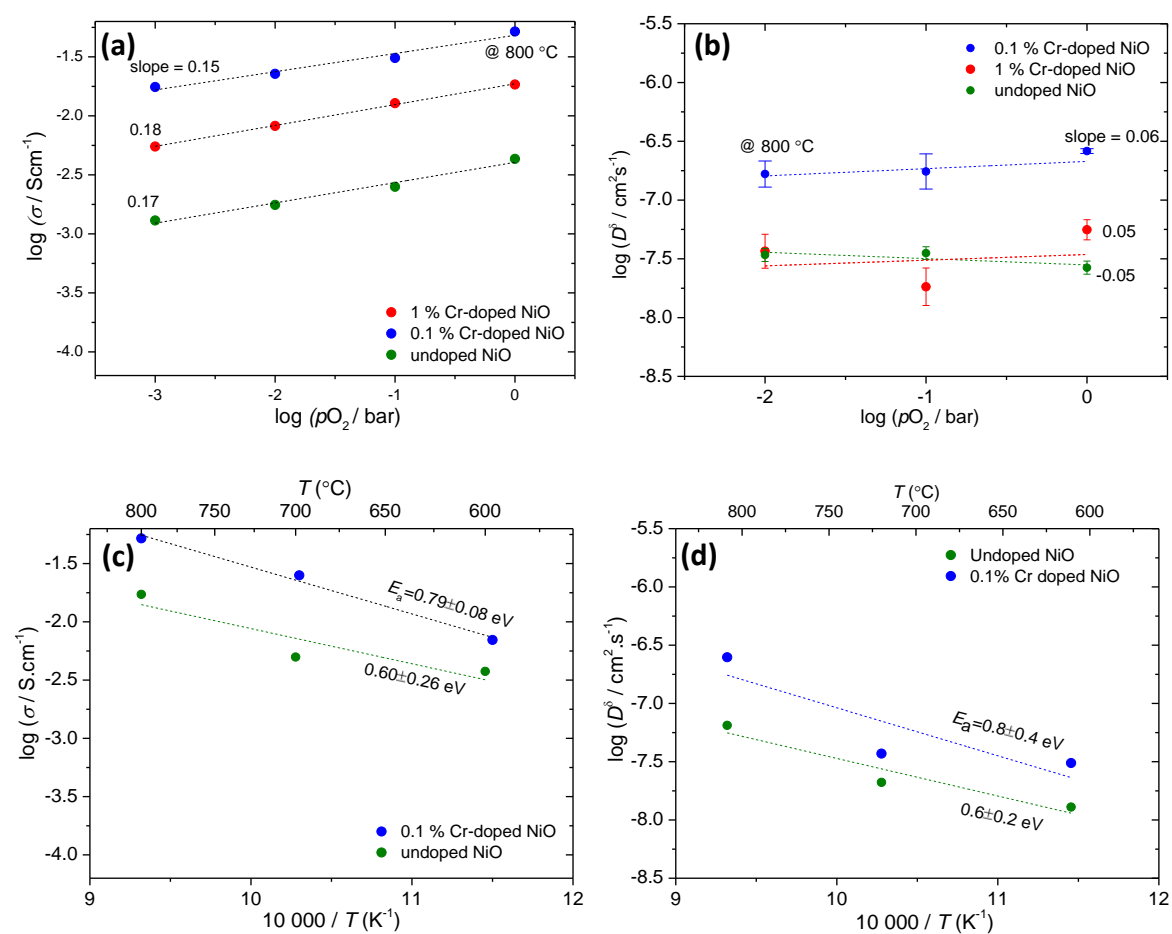


Figure 4.21: As-prepared samples: (a) Oxygen partial pressure dependence of conductivity and (b) oxygen partial pressure dependence of chemical diffusion coefficient at 700 °C (else a different temperature is indicated in the graph), (c) temperature dependence of conductivity and d) temperature dependence of chemical diffusion coefficient at 1 bar $p\text{O}_2$.

The numbers give the slopes of the linear regression lines for (a) and (b), and the activation energies E_a for (c) and (d) are calculated according to the Arrhenius equation.

The expected behavior for the Cr-doped NiO is a decrease in conductivity and an increase in chemical diffusion coefficient relative to undoped NiO because of increased nickel vacancy concentration and decreased hole concentration by donor doping. As explained in section 2.1.1 and summarized in Table 4.5, Cr doping will also change the pO_2 dependence of conductivity and of chemical diffusion coefficient.

Figure 4.21a presents the pO_2 dependence of conductivity for undoped and Cr-doped NiO. The slopes of the pO_2 dependence for 0.1 and 1 % Cr-doped NiO closely follow the expected behavior of undoped NiO ($\sigma_h \propto pO_2^{1/6}$), although the pO_2 dependence of conductivity in Cr-doped NiO should be 1/4 ($\sigma_h \propto pO_2^{1/4}$) in the case that major defects are doubly ionized nickel vacancies (see Table 4.5).

Figure 4.21b reveals the pO_2 dependence of the chemical diffusion coefficient for undoped and Cr-doped NiO samples. While the expected pO_2 dependence for Cr-doped samples is negative ($D_{Ni}^\delta \propto pO_2^{-1/4}$), all of the samples depict a pO_2 independent chemical diffusion coefficient which is a characteristic of undoped NiO.

The temperature dependences of the conductivity and the chemical diffusion coefficient are illustrated in Figure 4.21c and d. Undoped and Cr-doped NiO show similar activation energies for conductivity and chemical diffusion coefficient. The values of the activation energies are in agreement with literature values of NiO, as shown in Table A1-2 in appendix. Further details of the activation energies will be discussed in appendix A1.

The results for the as-prepared undoped and Cr-doped NiO show that Cr-dopant activity is not relevant in as-prepared samples. This is concluded from the following findings: (i) the pO_2 dependences of the Cr-doped samples are the same as undoped NiO for both conductivity and chemical diffusion coefficient, although, donor-doped NiO should exhibit a different pO_2 dependence, (ii) Cr-doping in NiO should decrease the hole concentration,

but the expected decrease in conductivity for doped samples relative to the undoped NiO is not observed, and (iii) the anticipated strong increase in the chemical diffusion coefficient is not achieved. D^δ of undoped and Cr-doped NiO differ by less than a factor of three which the Ni vacancy concentration of Cr-doped NiO is expected to exceed that of undoped NiO by several orders of magnitude. The results in Figure 4.21 are consistent with each other and all show that with respect to the transport properties, the Cr dopant is essentially not active as a donor dopant.

4.3.3.2. Annealed Samples

The pO_2 and the temperature dependence of the conductivity and the chemical diffusion coefficients as a function of Cr concentration for annealed undoped and Cr-doped NiO samples are shown in Figure 4.22.

The measurements of the annealed samples in Figure 4.22 reveal that the annealing at 1500 °C for 8 h activates Cr as a donor dopant in NiO. Furthermore, the results of annealed 0.1 % Cr-doped NiO depict a large decrease in the conductivity and an increase in the chemical diffusion coefficient.

The pO_2 dependences of conductivity for undoped and Cr-doped NiO are illustrated in Figure 4.22a. Undoped NiO shows the highest conductivity and the Cr-doped samples show lower conductivities, as anticipated from donor doping in NiO. The largest decrease in the conductivity and increase in the chemical diffusion coefficient is revealed by 0.1 % Cr-doped NiO. However, the pO_2 independent conductivity of undoped NiO disagrees with Table 4.5 (for undoped NiO: $\sigma_h \propto pO_2^{1/6}$). This is due to K impurities (shown in Table 3.2), which obviously act as acceptor dopant in NiO. The as-prepared samples also contain K impurities. The fact that K impurities and Cr dopants do not affect the values of σ and D^δ in as-prepared samples also confirms that annealing at 1500 °C for 8 hours is important to activate the dopant or the impurities.

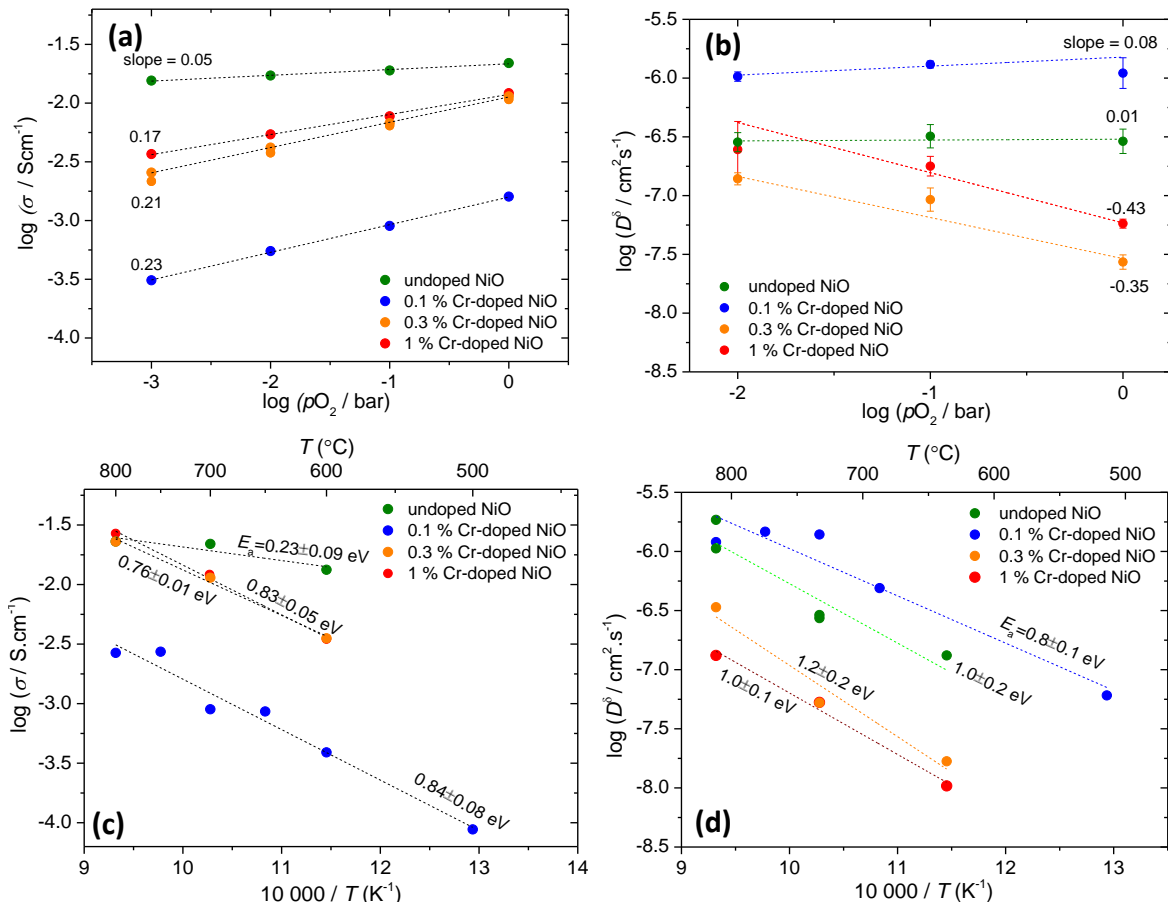


Figure 4.22: Annealed samples (1500 °C for 8 h): (a) Oxygen partial pressure dependence of conductivity and (b) oxygen partial pressure dependence of chemical diffusion coefficient at 700 °C, (c) temperature dependence of conductivity and (d) temperature dependence of chemical diffusion coefficient at 1 bar $p\text{O}_2$. The numbers give the slopes of the linear regression lines for (a) and (b), and the activation energies E_a for (c) and (d) are calculated according to the Arrhenius equation.

Although Cr-doped NiO is supposed to depict a negative $p\text{O}_2$ dependence ($D_{\text{Ni}}^\delta \propto p\text{O}_2^{-1/4}$, Table 4.5), Figure 4.22b shows that the annealed 0.1 % Cr-doped NiO has a $p\text{O}_2$ independent chemical diffusion coefficient which is a characteristic of the undoped NiO. The reason for this unexpected result is that 0.1 % Cr-doped NiO is also influenced by K impurities (0.08 %), largely compensating the Cr dopant. Therefore, 0.1 % Cr-doped NiO reflects the $p\text{O}_2$ dependence of the chemical diffusion coefficient in the same manner as undoped NiO. However, the annealed 0.1 % Cr-doped NiO reveals the highest chemical

diffusion coefficient within the samples in this work that show active Cr presence in NiO. Although the K presence affects the Cr activity in NiO; it is clear that the donor-dopant effect exists in annealed 0.1 % Cr-doped NiO.

The annealed 0.3 and 1 % Cr-doped NiO samples showed a decrease in conductivity (Figure 4.22a), and the conductivity is pO_2 dependent. Also, the chemical diffusion coefficient shows negative pO_2 dependence as expected for donor-doped NiO.

Consequently, the presence of donor-dopant activity is confirmed for all annealed doped samples. Although the pO_2 dependences of 0.3 and 1 % Cr-doped NiO are negative as expected, the chemical diffusion coefficient is not increased, and the decrease in conductivity for these samples was not in the expected range as compared to 0.1 % Cr-doped NiO. The nickel vacancy concentration in NiO is expected to increase with Cr doping and to further increase with the increase in dopant concentration. The results indicate that the Cr solubility limit in NiO is exceeded even for 0.3 % Cr concentration. It is also mentioned in a literature study [94] that formation of a spinel-like structure on Cr-doped NiO sample's surface is observed above 0.3 % Cr concentration. An additional discussion of the dopant activity and the solubility limit for these samples is given in section 4.3.4.

Since there was no pronounced dopant activity in the as-prepared samples, a direct comparison of the grain size effect on the chemical diffusion of NiO between as-prepared and annealed samples is not possible. However, it is clear that different heat treatments can change not only the grain size but also the defect regime in NiO (*i.e.*, by activating the defects). Different annealing conditions were applied for 0.1 and 1 % Cr-doped NiO. The results confirmed that annealing has a strong impact on defect properties of the samples and that not only the annealing temperature but also the annealing time is important. The detailed investigation of different annealing conditions on the transport properties of the doped samples (0.1 and 1 % Cr) is provided in the appendix A2.

4.3.4. Donor Dopant Concentration Effect

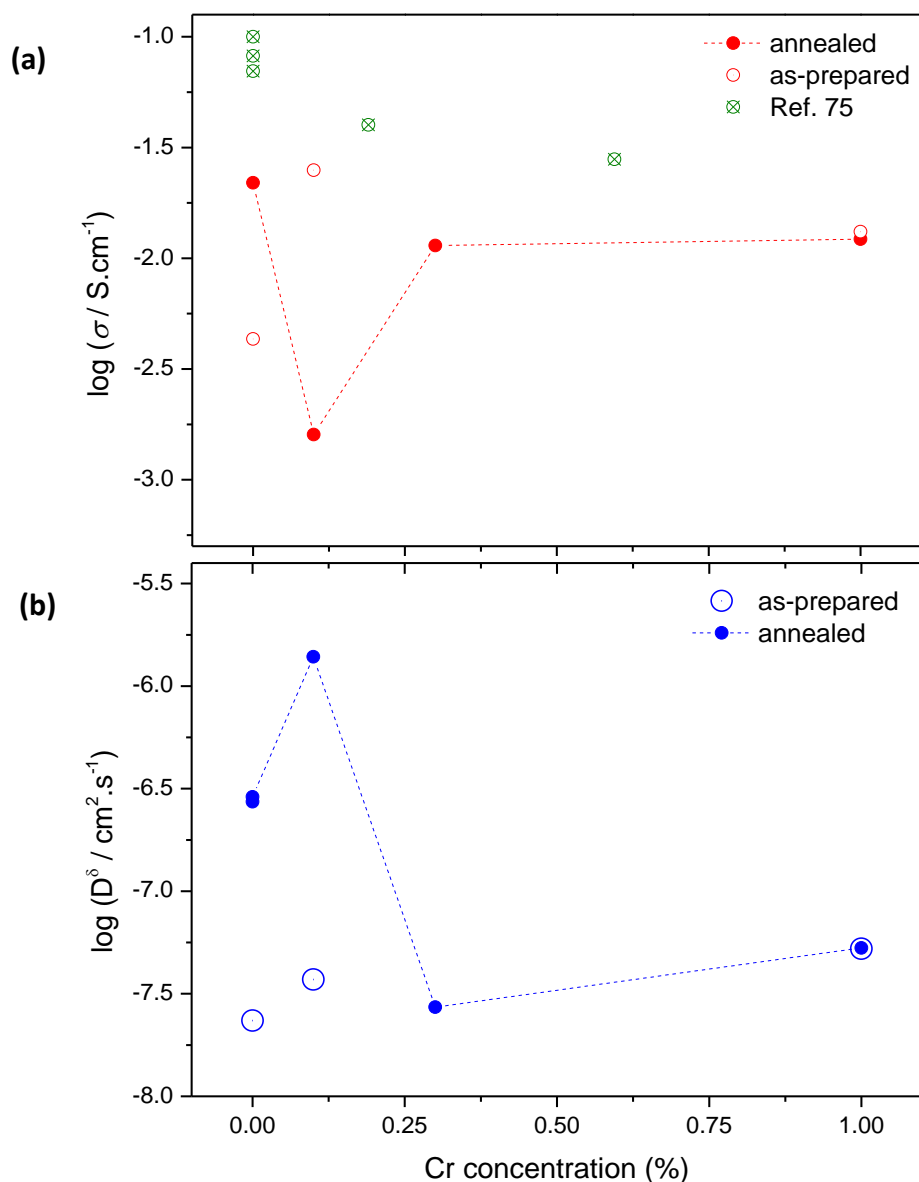


Figure 4.23: Comparison of the annealed and the as-prepared samples in this work as a function of Cr concentration at 700 °C and 1 bar $p\text{O}_2$ (a) for conductivity together with the literature data [75] and (b) for chemical diffusion coefficients.

In Figure 4.23a, conductivity values of undoped and Cr-doped NiO for the annealed and the as-prepared samples are presented and compared to the literature [75]. The figure clearly indicates that Cr dopant activity is not relevant in as-prepared samples because the

expected decrease in conductivity by donor doping is not seen. Also, the chemical diffusion coefficients for the as-prepared samples do not change much in Figure 4.23b. However, annealed 0.1 % Cr-doped NiO reveals a strong decrease in conductivity and an increase in chemical diffusion coefficient as expected from donor doping.

From the previous sections, it is already known that while as-prepared samples do not show a Cr dopant activity, annealed samples reveal Cr activity by a decreased conductivity for all the samples and an increased chemical diffusion coefficient for 0.1 % Cr-doped NiO. On the other hand, annealed 0.3 and 1 % Cr-doped NiO samples show an increased conductivity compared to 0.1 % Cr-doped NiO and the conductivity of these samples is relatively close to the value of the undoped NiO (Figure 4.23a). This may indicate another mechanism which provides the observed increase in conductivity for annealed 0.3 and 1 % Cr-doped samples. Otherwise, after exceeding the Cr solubility limit, the conductivity should saturate. Raman and TEM/EDX analysis showed the presence of a NiCr_2O_4 spinel phase in Cr-doped NiO samples. Also, Raman analysis showed that the amount of the NiCr_2O_4 increases with increased Cr concentration and annealing (see Figure 4.26b), suggesting that annealing increases the Cr consumption by spinel phase formation. This can explain the increased conductivity and the decreased chemical diffusion coefficient for annealed 0.3 and 1 % Cr-doped NiO samples in Figure 4.23. The conductivity of these samples is shifted to the level of undoped NiO, most likely caused by Cr consumption of the spinel phase. The chemical diffusion coefficient for 0.3 and 1 % Cr-doped NiO samples is even lower than for undoped NiO, suggesting that the spinel phase which is located along the grain boundaries destroys the fast Ni diffusion paths by blocking the grain boundaries (as a barrier for Ni diffusion).

4.3.5. Literature on Conductivity & Chemical Diffusion Coefficient

4.3.5.1. Temperature Dependence of Conductivity

In Figure 4.24, the temperature dependence of conductivity for the annealed undoped and Cr-doped NiO is compared with literature data [75, 77, 95, 96]. The activation energies of undoped and Cr-doped samples in literature and in the present work are in agreement. Also, the conductivity values of undoped and Cr-doped samples (except 0.1 % Cr-doped NiO) in this work are similar to the ones in literature. This shows that, in the literature studies, Cr doping did not have a significant effect on defect concentrations in NiO for the concentration range of 0.10 to 3.95 % Cr [75, 77, 95]. This indicates that the solubility limit of Cr in NiO is probably much lower than assumed in literature (*i.e.*, 1 % at 1000 °C [77]). There is only one exception in the literature [96] which shows a much lower conductivity value, which in fact is the same value (with the extrapolation to same temperature range) as the annealed 0.1 % Cr-doped NiO sample's conductivity in this work.

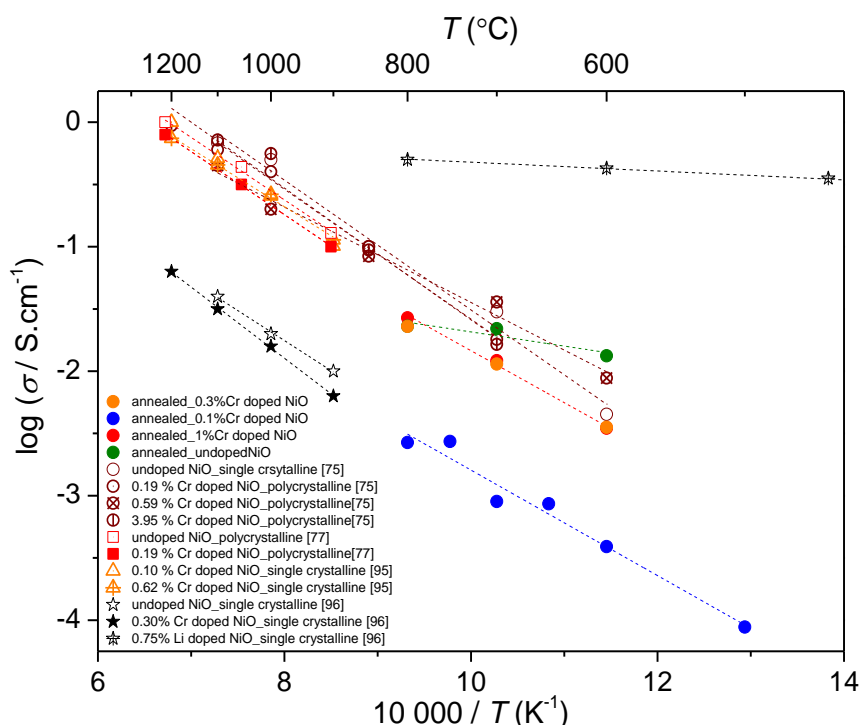


Figure 4.24: Temperature dependence of conductivity for undoped NiO [75, 77, 96] and Cr-doped NiO [75, 77, 95, 96]. The figure shows literature data as well as present results.

The present results show clearly that 0.1 % Cr-doped NiO have a much reduced conductivity as compared to undoped samples. This conductivity value is lower than the literature value for the same and also even for higher dopant concentrations. This confirms that Cr dopant is active for annealed 0.1 % Cr-doped sample and that it reveals a stronger effect than reported in the literature.

The literature study [96] compares the conductivity of single crystalline undoped, 0.3 % Cr-doped and 0.75 % Li-doped NiO samples. These results are illustrated in Figure 4.24 (black symbols). The results in ref. [96] show that strongly acceptor doped NiO exhibits a higher conductivity than undoped and Cr-doped NiO, as also observed in the present work. But in the same study, undoped NiO and 0.3 % Cr-doped NiO (containing also 0.3 % Co impurity) show very similar conductivities. These values are very similar to the 0.1 % Cr-doped NiO in the present work in contrast with other literature results. The similar conductivity values for undoped and 0.3 % Cr-doped NiO in that work [96] can be explained by considering that the solubility limit of Cr was exceeded or/and the dopants were inactive. The reason for the low conductivity value compared to other literature data even for undoped NiO is not clear, however.

4.3.5.2. Temperature Dependence of Chemical Diffusion Coefficient

The chemical diffusion coefficients of undoped NiO [35, 67, 97-102] and of single crystalline Cr-doped NiO [95] are illustrated in Figure 4.25 and compared to results of this work. First, the figure indicates that in literature there is a large scatter in values for the chemical diffusion coefficients of NiO. Rom et al. [102] obtained the highest chemical diffusion coefficient with a polycrystalline NiO sample compared to single-crystalline NiO samples in literature (indicated in the figure with the dashed lines). While present undoped NiO has a slightly lower value than the highest chemical diffusion coefficient of NiO in the literature [102], the value of the annealed 0.1 % Cr-doped NiO is slightly higher. The only chemical diffusion coefficient value of Cr-doped NiO found in the literature [95] is also shown in Figure 4.25. Surprisingly, the value of the chemical diffusion coefficient of single crystalline Cr-doped NiO [95] is lower than for some of the undoped single crystalline NiO

[97, 103] and polycrystalline undoped NiO [102] in literature. Also, the samples in this work show a higher chemical diffusion coefficient than the reported single crystalline Cr-doped NiO [95]. The higher chemical diffusion coefficient for the samples in this work might be caused by two reasons: (i) enhanced diffusion along the grain boundaries, and (ii) activated donor doping (effect) in the samples.

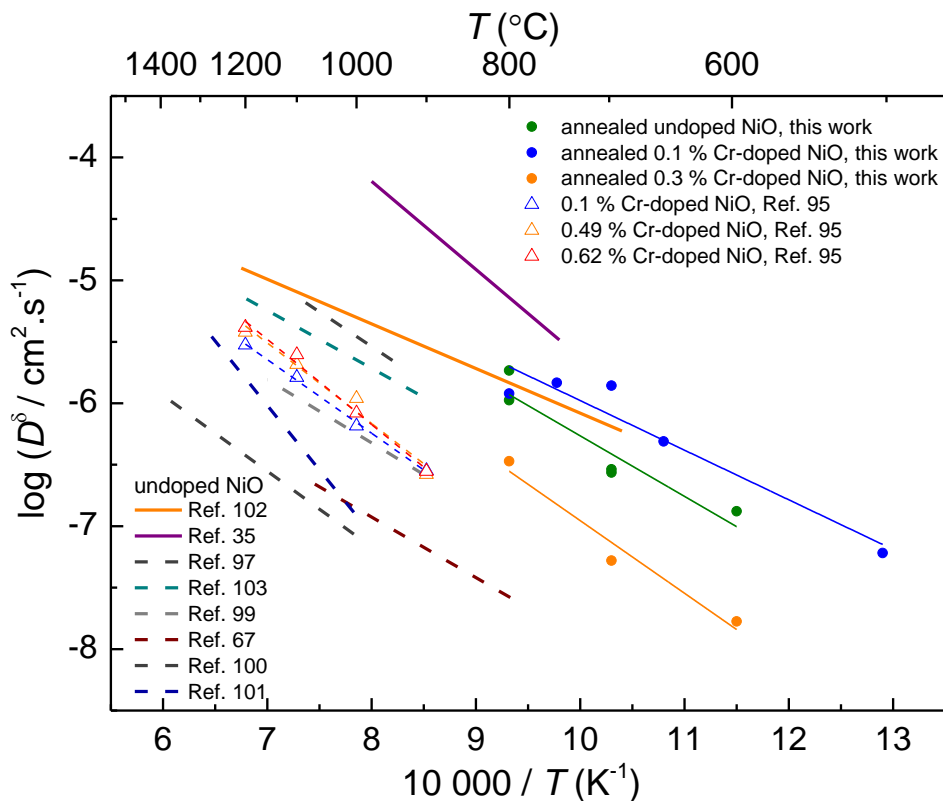


Figure 4.25: Temperature dependence of chemical diffusion coefficient of single-crystalline undoped NiO [67, 97, 99-101, 103], polycrystalline undoped NiO [35, 102], and single crystalline Cr-doped NiO [95] presented with the results of this work (polycrystalline undoped and Cr-doped NiO). The polycrystalline NiO sample in Morlotti's study shows a higher diffusion coefficient than all other data in the figure, but the density of this sample is 92 % which might not provide a proper diffusion length and probably the values have a contribution from open pores [97]. Therefore the data is not considered in the discussion.

The only result in the literature [95] for single crystalline Cr-doped NiO (indicated in the figure with open triangles) shows a slightly lower chemical diffusion coefficient and very similar activation energies to the results of 0.3 % Cr-doped NiO (solid orange

symbols) in this work. This indicates that, in spite of its polycrystallinity, bulk diffusion is dominant for 0.3 % Cr-doped NiO sample because fast grain boundary diffusion of Ni in NiO is apparently inhibited by NiCr₂O₄ spinel formation at grain boundaries. Therefore this formation impedes fast diffusion of Ni along the grain boundaries and a behavior similar to bulk diffusion is observed for 0.3 % Cr-doped NiO sample.

4.3.6. Raman Spectroscopy on Pellets and Powders

Raman spectra were measured to investigate the phase purity of Cr-doped NiO samples. While perfectly cubic NiO does not show the first order Raman peak according to the selection rules of Raman spectroscopy [104-106], NiCr₂O₄ [107] and Cr₂O₃ [85] phases do show first order Raman peaks. Since NiO displays a slight rhombohedral distortion from perfect cubic structure (see XRD results in section 4.3.1), the first order Raman peak is also visible for NiO as shown in Figure 4.26a.

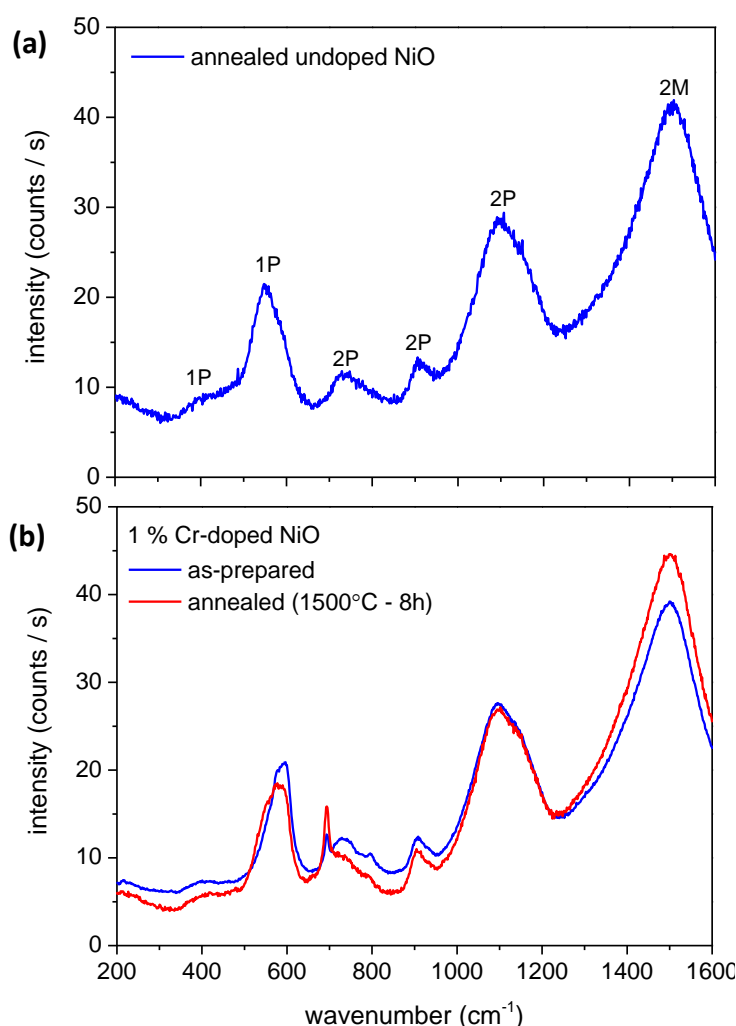


Figure 4.26: Raman spectra of (a) annealed undoped NiO pellet and (b) annealed and as-prepared 1 % Cr-doped NiO pellets.

Annealed undoped NiO was analyzed as a reference sample. In Figure 4.26a, peaks due to one-phonon (1P), two-phonon (2P) and two-magnon (2M) scattering are indicated: 1P peaks at $\sim 400\text{ cm}^{-1}$ [108] and $\sim 560\text{ cm}^{-1}$ [106, 108], 2P at $\sim 740\text{ cm}^{-1}$, $\sim 925\text{ cm}^{-1}$ and at $\sim 1100\text{ cm}^{-1}$ [106, 108]. The peak is at $\sim 1500\text{ cm}^{-1}$ due to 2M scattering [106, 108]. Figure 4.26b shows as-prepared and annealed 1 % Cr-doped NiO samples. A new very sharp peak appears at $\sim 700\text{ cm}^{-1}$, which can be assigned to the NiCr_2O_4 spinel phase [107] (reaction product of NiO and Cr_2O_3) [109]. Its intensity relative to the other NiO peaks increases upon annealing.

In Figure 4.27, annealed undoped and Cr-doped samples are compared. The peak at 700 cm^{-1} appears also for 0.1 % Cr-doped NiO, which indicates that even 0.1 % Cr-doped NiO contains a small amount of the undesired NiCr_2O_4 phase. The peak becomes more intense with increasing Cr content from 0.1 to 1 %.

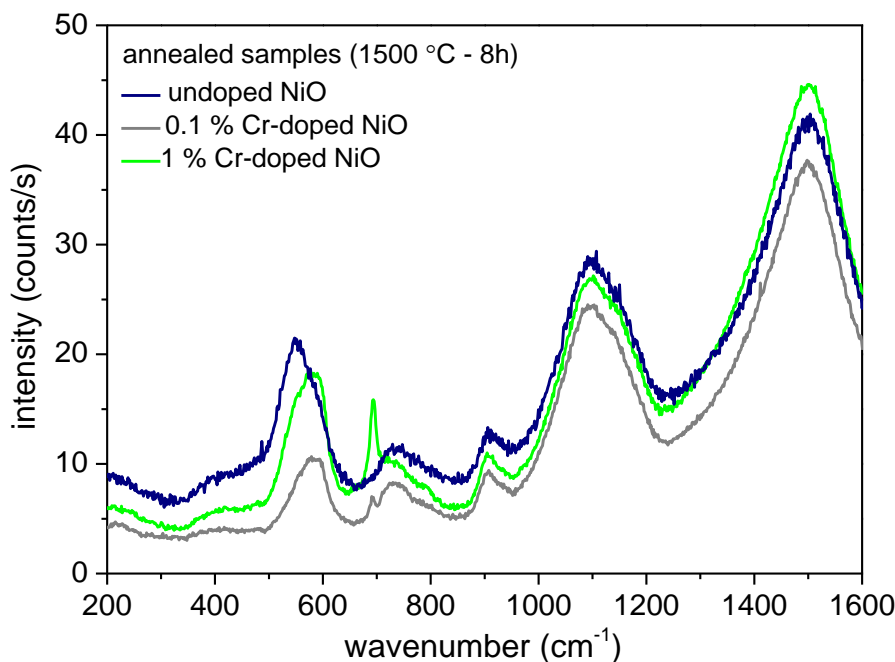


Figure 4.27: Raman spectra of annealed undoped, 0.1 % Cr-doped and 1 % Cr-doped NiO pellets.

Furthermore, Figure 4.27 shows that there is a slight 1P peak shift from $\sim 560\text{ cm}^{-1}$ to $\sim 580\text{ cm}^{-1}$ with increasing the Cr content. This could be either a sign of two overlapping

peaks (NiO and Cr₂O₃) or it could result from the distortion of the NiO lattice induced by the dopant. The spectrum of commercial Cr₂O₃ (Alfa Produkte, 99.8 % purity) is presented in Figure 4.28. The most intense Raman peak of Cr₂O₃ powder is at 550 cm⁻¹ which is close to the position of that of the aforementioned NiO peak. But since it is very sharp, it cannot be the reason for the peak shift in Figure 4.27.

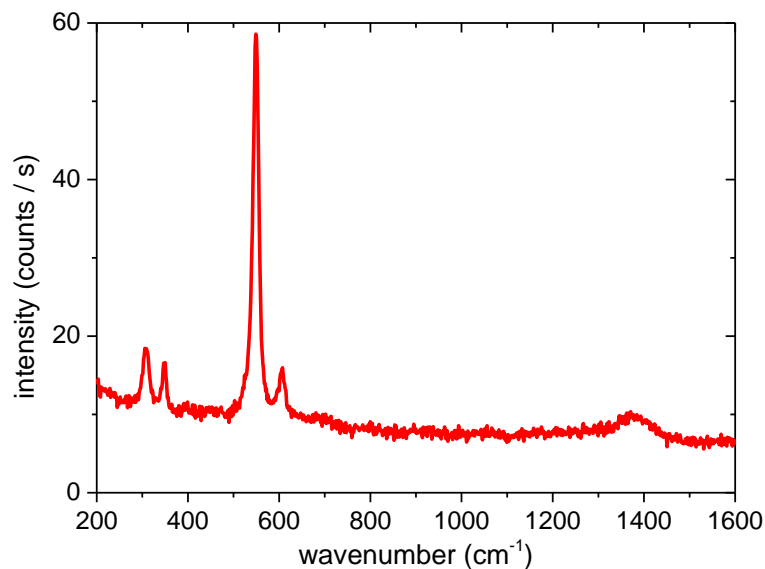


Figure 4.28: Raman spectra of commercial Cr₂O₃ powder.

Additionally, undoped and Cr-doped NiO powders were analyzed by Raman spectroscopy to check the presence of NiCr₂O₄ spinel phase already in the as-synthesized powders (Figure 4.29). While 0.3 and 1 % Cr-doped NiO powders show NiCr₂O₄ peaks, undoped NiO and 0.1 % Cr-doped NiO show only NiO Raman peaks. This indicates that the solubility limit of Cr in NiO at 750 °C (calcination temperature for NiO powder synthesis) is lower than 0.3 % Cr. The fact that XRD (see Figure 4.19) showed only NiO reflections for all Cr-doped NiO powders indicates that the amount of NiCr₂O₄ is too low and/or the NiCr₂O₄ grain size is too small to bring its XRD peaks above the detection limit.

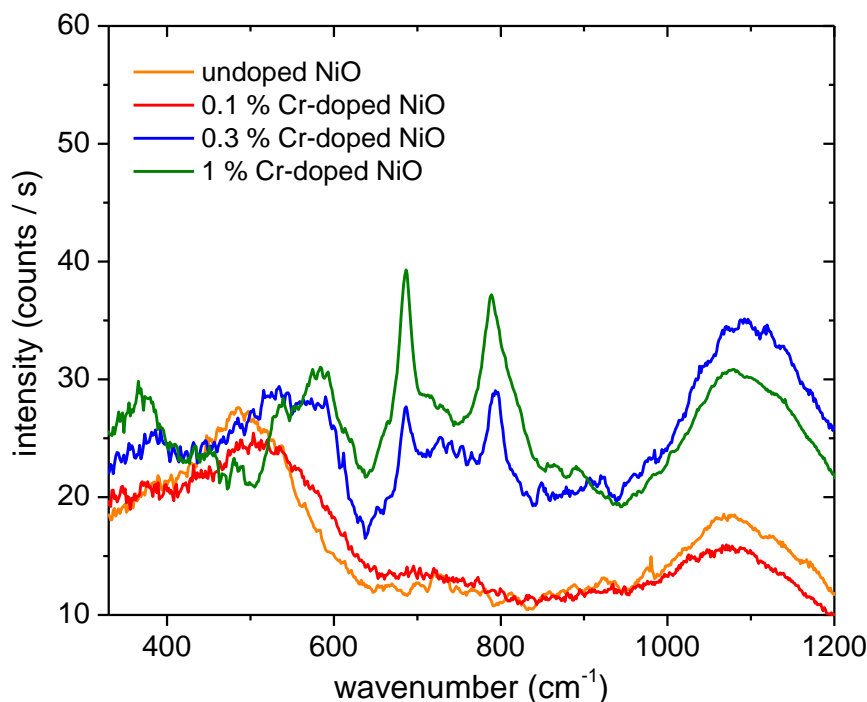


Figure 4.29: Raman spectra of undoped and Cr-doped NiO as-synthesized powders.

In addition to the presence of the NiCr_2O_4 Raman peak at 700 cm^{-1} in Figure 4.29 for 0.3 and 1 % Cr-doped NiO, one more peak appears at 800 cm^{-1} . This unidentified peak at 800 cm^{-1} appears weakly as a shoulder also for the 1 % Cr-doped NiO pellet shown in Figure 4.27. This peak could belong to a Cr-related phase since it appears only upon Cr doping. It raises the possibility that the peak is related to the NiCr_2O_4 spinel phase which was not observed in the previous literature studies [85, 107]. Only one of the studies [107] showed a broad and very weak Raman peak at 800 cm^{-1} for NiCr_2O_4 , but it was assigned to an overtone mode.

According to the results of Raman spectroscopy on the as-synthesized powders, the 0.1 % Cr-doped NiO powder does not contain the NiCr_2O_4 phase, whereas the pellet from the same powder shows a small Raman peak of NiCr_2O_4 . In addition to this, Figure 4.26b shows that for 1 % Cr-doped NiO the peak intensity increases upon annealing. Therefore, the effect of SPS and of annealing on the formation of the undesired spinel phase NiCr_2O_4 is worth being studied in greater detail, which is however out of the scope of this work.

4.3.7. TEM/EDX Analysis on Pellets

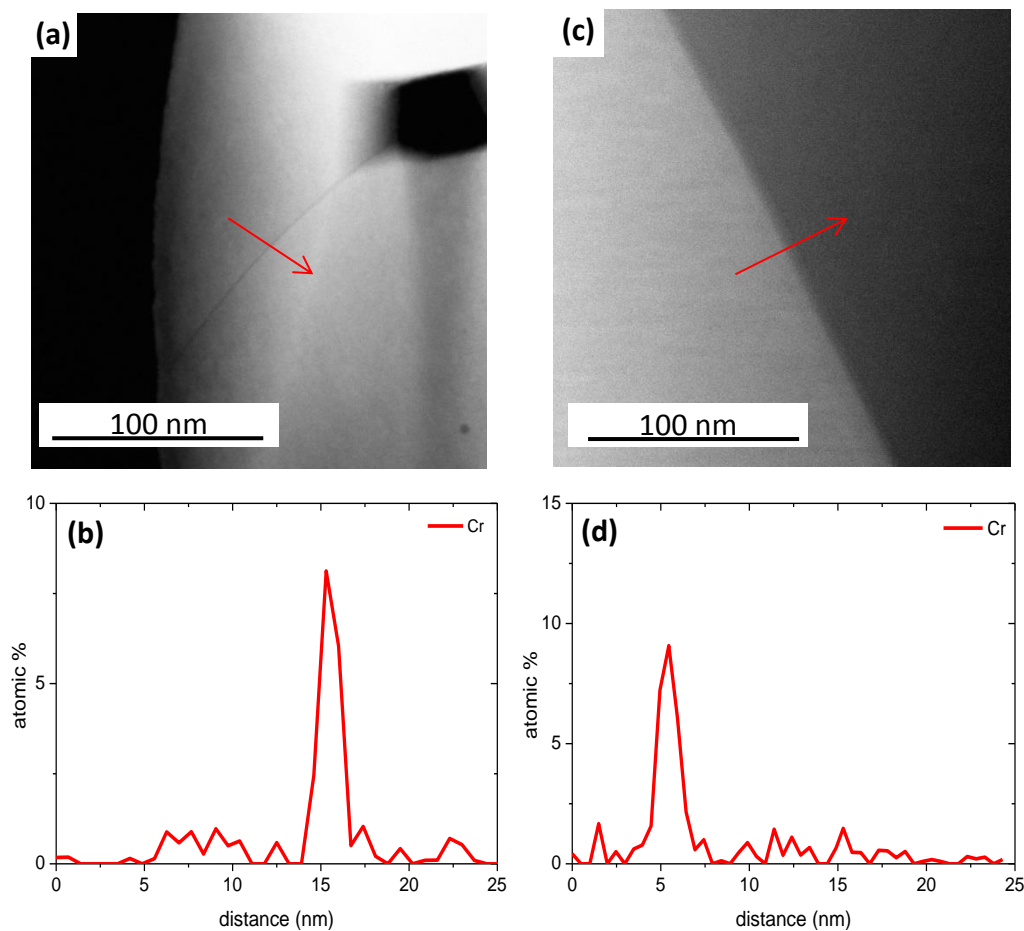


Figure 4.30: 0.1 % Cr-doped NiO: (a) TEM image of the as-prepared pellet, (b) EDX analysis of the as-prepared pellet across the grain boundary, (c) TEM image of the annealed pellet, and (d) EDX analysis of the annealed pellet across the grain boundary. The red arrows indicate the direction along which EDX signal was measured.

Since some of the samples showed an unexpected behavior in the conductivity relaxation measurements (see section 4.3.3), as-prepared and annealed 0.1, 0.3 and 1 % Cr-doped NiO samples were analyzed by TEM and EDX. The 0.1 % Cr-doped samples showed a homogeneous microstructure and there was no precipitation of Cr-related phases or any other impurity phases as seen by TEM images in Figure 4.30. However, EDX analyses across grain boundaries (Figure 4.30b and d) showed a Cr segregation in the grain boundary regions. The same behavior is observed for both the as-prepared and the annealed

samples. It should be noted that the low and scattered Cr signal within the grain does not prove the absence of Cr in the grains, but reflects the fact that the low Cr concentration (0.1 %) is below the EDX detection limit.

Although Cr segregation is present in the 0.1 % Cr-doped NiO grain boundaries, this sample showed the highest increase in chemical diffusion coefficient and the highest drop in conductivity. It is thus possible to conclude that despite some Cr accumulation at the grain boundaries, a donor doping effect is still present in the grain interior. If the sample had a homogeneous Cr content, the chemical diffusion coefficient of the sample would be even higher.

The 0.3 % Cr-doped NiO pellet was also analyzed by TEM/EDX as shown in Figure 4.31. The black features in both Figure 4.30 and Figure 4.31 are pores, characterized by the absence of cation signal in EDX analysis. Cr segregation to the grain boundaries is also observed for this composition in both as-prepared and annealed samples. Similar to 0.1 % Cr-doped NiO, 0.3 % Cr-doped NiO showed no NiCr_2O_4 phase in the grains, however, there is Cr segregation at the grain boundaries. The 0.3 % Cr-doped NiO samples show a broader EDX peak at the grain boundaries for Cr segregation compared to 0.1 % Cr-doped NiO (see Figure 4.31).

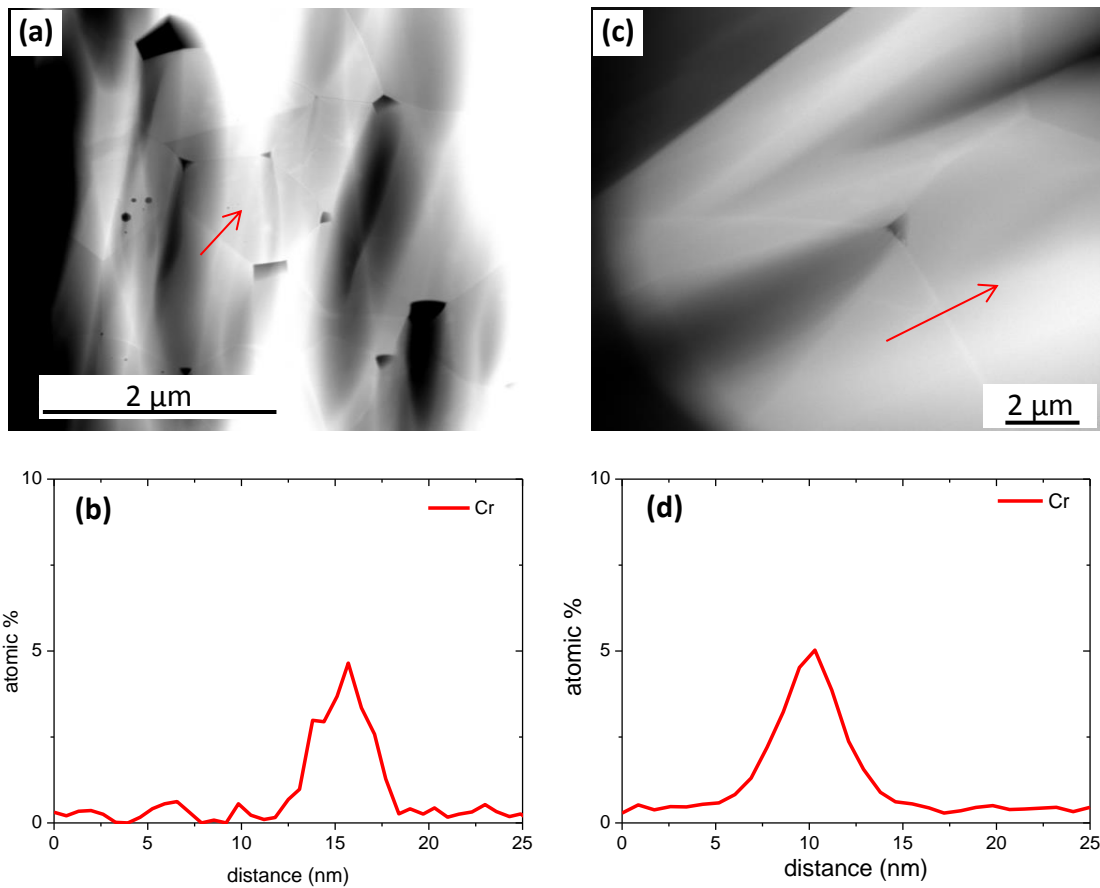


Figure 4.31: 0.3 % Cr-doped NiO: (a) TEM image of the as-prepared pellet, (b) EDX analysis of the as-prepared pellet across the grain boundary, (c) TEM image of the annealed pellet, and (d) EDX analysis of the annealed pellet across the grain boundary. The red arrows indicate the direction along which EDX signal was measured.

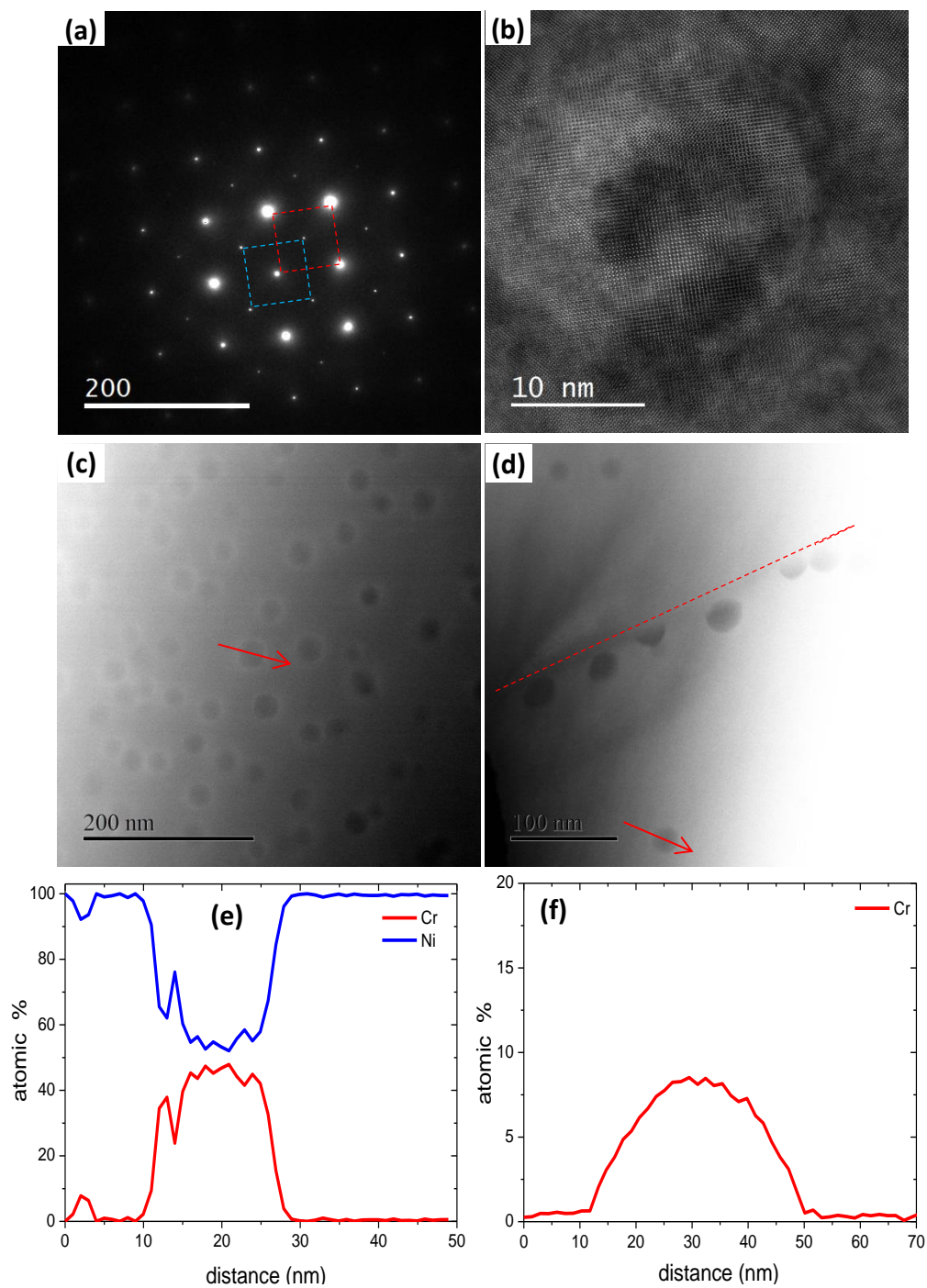


Figure 4.32: Annealed 1 % Cr-doped NiO pellet: (a) Electron diffraction pattern (blue square: NiCr₂O₄ and red square: NiO), (b) high resolution TEM image, (c) TEM image of NiCr₂O₄ particles in NiO matrix, (d) TEM image of NiCr₂O₄ particles within the NiO matrix and along the grain boundary (dashed red line indicates the grain boundary), (e) and (f) EDX analysis of a NiCr₂O₄ particle. The red arrows indicate the direction along which EDX signal was measured.

Figure 4.32 shows the TEM/EDX analysis of the annealed 1 % Cr-doped NiO sample. Such a high Cr concentration in NiO is already reported in the literature [74-77, 110] to be at or beyond the solubility limit at 1000 °C. The brighter spots in the electron diffraction pattern in Figure 4.32a belong to NiO (indicated with a red dashed square) whereas the weaker spots belong to NiCr₂O₄ (indicated by a blue dashed square). Also, the spinel phase may contribute to the brighter spots. The high-resolution image in Figure 4.32b shows ~20 nm diameter NiCr₂O₄ spinel phase precipitates within the NiO matrix. The two phases can be recognized from characteristic lattice plane spacing: 2.88 Å for NiCr₂O₄ and 2.09 Å for NiO. EDX analysis also confirms this assignment, however, it did not yield the exact ratio (2:1) of Cr to Ni. The main reason for this deviation (from 2:1 to 1:1, Figure 4.32e) is the sample thickness. Because, when the sample is not enough thin, the spectrum also contains signals from the NiO matrix.

With these analyses, it is possible to conclude that NiCr₂O₄ formation in NiO starts between 0.3 and 1 % at 1000 °C (pellet preparation temperature). Raman spectroscopy and TEM/EDX results confirmed that there is an inhomogeneity (Cr accumulation at grain boundaries and/or NiCr₂O₄ formation) in all ceramic samples.

4.3.8. Concluding Discussion on the Chemical Diffusion Coefficient of NiO

Chemical diffusion coefficient measurements were performed for undoped and Cr-doped NiO for as-prepared and annealed samples. The annealed and as-prepared samples are expected to yield different results because of the different grain size. The results are shown here reveal that the Cr dopant is not active in the as-prepared samples: (i) the hole concentration is not decreased by donor doping, (ii) Cr-doped samples show the same pO_2 dependence of the conductivity and of the chemical diffusion coefficient as undoped NiO. Therefore, observing the grain size effect on the transport properties of NiO without a change in the defect chemistry was not possible.

The annealed samples demonstrate that the Cr doping is active as donor dopant, most pronounced by the 0.1 % Cr-doped NiO. Although 0.3 and 1 % Cr-doped NiO showed the

characteristic negative pO_2 dependence of donor doping for the chemical diffusion coefficient, only the 0.1 % Cr-doped NiO displayed a significant increase in the chemical diffusion coefficient with strongly decreased conductivity relative to undoped NiO (see Figure 4.22 and Figure 4.23). The reason for the doping effect to be most pronounced for the annealed 0.1 % Cr-doped NiO sample is the low solubility limit of Cr in NiO. In this work, it is found that the solubility limit of Cr in NiO is much lower (< 0.3 % at 750 °C) than assumed in the literature (*i.e.*, 0.85 % at 850 °C [75], 1 % at 1000 °C [77]). At higher nominal Cr concentrations most of the Cr forms a segregated $NiCr_2O_4$ spinel phase and consequently no increase in the chemical diffusion coefficient and no decrease in the conductivity is observed.

Although the annealed 0.1 % Cr-doped NiO exhibits a small presence of $NiCr_2O_4$, the Cr is not entirely consumed by the spinel phase. It reveals a most pronounced donor doping effect within the samples as far as the conductivity and the chemical diffusion coefficient are concerned. The 0.3 and 1 % Cr-doped NiO samples display lower chemical diffusion coefficients than nominally undoped NiO. A likely explanation for this behavior is that doping and the spinel phase have a competing effect on transport in NiO. While the Cr dopant activity leads to the expected pO_2 dependence of the chemical diffusion coefficient of Cr-doped samples, the $NiCr_2O_4$ phase at the grain boundaries might block fast diffusion paths parallel to the grain boundaries.

The $NiCr_2O_4$ spinel phase was not detected by XRD even for 3 % Cr-doped NiO pellets, however, Raman spectroscopy clearly showed the presence of the spinel phase even for very low Cr concentration (0.1 and 0.3 % Cr) for annealed and as-prepared samples. The amount of the spinel phase increases upon annealing and with larger Cr concentration. Additionally, TEM/EDX analysis depicted a strong Cr segregation at the grain boundaries already for 0.1 and 0.3 % Cr in NiO for as-prepared and annealed samples. The annealed 1 % Cr-doped NiO exhibited spherical $NiCr_2O_4$ crystallites both inside the grains and at the grain boundaries. One has to note that Raman analysis of as-synthesized Cr-doped NiO powders reveal that 0.1 % Cr-doped NiO powder does not exhibit $NiCr_2O_4$ phase, meaning

that further temperature treatments for pellet preparation (*e.g.*, SPS) cause the spinel phase formation in 0.1 % Cr-doped NiO pellets.

As compared to the literature (Figure 4.24), the annealed 0.1 % Cr-doped NiO is found to exhibit the highest drop in conductivity relative to undoped NiO. This indicates that the donor doping effect is present for annealed 0.1 % Cr-doped NiO. When the chemical diffusion coefficient is compared to the literature, the annealed 0.1 % Cr-doped NiO shows the highest chemical diffusion coefficient, although the annealed undoped NiO and the results of Rom et al. on polycrystalline undoped NiO [102] show similar values. This indicates that fast grain boundary diffusion is predominant even for Cr-doped NiO sample, especially at temperatures below 1000 °C. The difference in chemical diffusion coefficient between undoped and Cr-doped NiO is not in the range of orders of magnitude when polycrystalline samples are compared. There is only one available chemical diffusion coefficient measurement on single crystalline Cr-doped NiO by Nowotny et al. [95] which shows much lower values than the current work.

In summary, annealed 0.1 % Cr-doped NiO reveals the highest chemical diffusion coefficient in literature, but the values are very close to polycrystalline undoped NiO (this work and reference [102]). This comparison highlights the importance of fast grain boundary diffusion in NiO. Because of the low solubility of Cr in NiO, the contribution of the grain boundaries to enhanced diffusion is stronger than that of the Cr dopant.

5. Summary and Conclusions

Irreversible generation of structures in solids is of great importance for a variety of basic and applied aspects. One specific example is long-term data storage. If such structures could be quickly fabricated at high temperatures but be essentially frozen at room temperature, such a procedure would be extremely adequate for such archiving purposes. This, however, sets harsh constraints on the kinetics. The main research interest in the present work was to understand and to control the growth of dense oxide layers under various experimental conditions. This involved the investigation of growth rates of thin metal films as a function of thickness, temperature, oxygen partial pressure, UV light and doping to identify the rate-determining process (diffusion or surface reaction) and increase the reaction rate constant for applications such as data archiving systems.

Oxidation kinetics of thin metal films (Cr, Al, Ti, V, Zn, Ni, and Co) were investigated in this thesis for a thickness range of 10-150 nm at temperatures between 200 and 500 °C, which is lower than the typical temperatures (> 500 °C) for oxidation studies in the literature. Kinetics of all the thin metal films was controlled by diffusion, following Wagner's oxidation theory (parabolic rate law). Accordingly, different experimental conditions applied for *in-situ* oxidation measurements such as different thicknesses, UV illumination, and different oxygen partial pressures did not change the oxidation kinetics of the films. This confirms that the oxidation of the films is controlled by diffusion. Co and Ni showed the fastest reaction rate constants, but still the reaction rate is not in the desired range for data storage applications. Millisecond oxidation time is expected to be obtained for 10 nm thick Co films at 540 °C.

In this project, however, much faster oxidation rate constants were found compared to the literature studies (single crystalline and polycrystalline samples) when the films of small grain size (10-30 nm) were investigated. This indicates that fast Ni diffusion along the grain boundaries contributes to diffusion significantly in the studied temperature range.

The motivation of this study is to identify metals which have the fast oxidation at elevated temperatures and at the same time are sufficiently oxidation-resistant at room temperature. Since the reaction rate constants of pure metal films were not high enough for the potential application, donor-doping was used for Ni films in order to increase the Ni vacancy concentration and thus the reaction rate constant. However, Ni films and Cr-doped Ni films (0.1 and 1 % Cr) showed no significant difference in the reaction rate constants. XPS depth profiling of Cr-doped Ni films (metal and oxidized forms) indicated that during the oxidation a Cr-rich layer remains close to the substrate-oxide interface. This inhomogeneous distribution of Cr in the film inhibits faster oxidation. Magnetron sputtering and low-temperature PLD (-180 °C) were used as alternative techniques to grow Cr-doped films. PLD grown samples are promising for obtaining higher oxidation rate constants, but further investigations are necessary.

In contrast to the literature, which generally assumed that the lower bound of applicability of Wagner's theory is roughly 300 °C and 20 nm film thickness, *in-situ* oxidation measurements in this work indicated that even for 10 nm Ni and Co films at relatively low temperatures such as 200-250 °C, the parabolic rate law is still valid. Even when the sample thickness was decreased to 10 nm, a change to surface reaction control was not seen, in contrast to the behavior of perovskite samples in the literature. The reason for this difference is that the cation diffusion coefficient in binary oxides is typically much lower than the oxygen diffusion coefficient in perovskites.

In addition to film oxidation, the transport properties of undoped and Cr-doped NiO ceramic samples was studied for the following purposes: (i) to obtain a homogeneous Cr distribution in the bulk samples, to better investigate the Cr effect on transport properties of NiO, and (ii) to understand the grain size effect on diffusion by systematically changing the

grain size of the ceramics by annealing. Even though the grain size of the ceramics could be controlled by annealing at different temperatures, it was not possible to quantify the grain size effect on diffusion, because the annealing process had a complex impact on the dopant activity in the samples.

In as-prepared samples (spark plasma sintered for 5 min at 1000 °C) Cr was not active as a donor dopant and the transport results of Cr-doped NiO were almost identical to undoped NiO.

Annealed samples (8 h at 1500 °C) showed a dopant activity, and it was possible to increase the chemical diffusion coefficient of NiO with 0.1 % Cr doping by more than one order of magnitude at 700 °C. The pO_2 dependence of the chemical diffusion coefficient revealed a Cr doping effect also for 0.3 and 1 % Cr-doped NiO samples. However, these samples did not show a significant increase in chemical diffusion because of Cr segregation at the grain boundaries. For all the Cr-doped NiO samples, $NiCr_2O_4$ spinel was detected by TEM/EDX analysis and Raman spectroscopy. Raman analysis revealed that the amount of $NiCr_2O_4$ spinel phase increases with increasing Cr concentration. These careful investigations indicate a lower Cr solubility in NiO than assumed in the literature. Even though the 0.1 % Cr-doped NiO also showed some spinel phase formation, the donor-doping was most pronounced as not all the Cr was consumed by the spinel phase. For higher Cr concentrations, the $NiCr_2O_4$ spinel phase at the grain boundaries inhibits the fast diffusion of Ni along the grain boundaries by counteracting the doping effect.

In summary, Co and Ni thin films showed the highest oxidation rate constants of all metals investigated here. Thin Co films are expected to allow a millisecond oxidation time for possible applications. A change of the rate determining process from diffusion to surface reaction was not observed for film thicknesses down to 10 nm. Although it was not possible to increase the reaction rate constant by Cr doping in thin films, annealed 0.1 % Cr-doped NiO ceramic samples showed an increased chemical diffusion coefficient and decreased conductivity as expected from the defect chemical model. This sample revealed the highest chemical diffusion coefficient reported so far for NiO, which is much higher

than for single crystalline Cr-doped NiO. This emphasizes the importance of grain size for Ni diffusion in NiO, not only for thin films but also for bulk samples. While a decrease of the oxide grain size has the potential to further accelerate Ni film oxidation kinetics, it is challenging to decrease the grain size below the range of 10-30 nm that is a characteristic of the films in the present investigation.

During this work, metal films were mostly prepared by e-beam evaporation technique (substrates at room temperature) which does not provide uniform film thickness for less than 10 nm. Should one want to exploit the regime of extremely thin films, alternative film growth techniques (*e.g.*, PLD, magnetron sputtering or e-beam evaporation on a heated substrate) may be used. This would give a possibility to observe the lower bound of validity of the classic oxidation theory. In this work, the highest oxidation rate constant was found for 10 nm Co films, with an extrapolated millisecond oxidation time at 540 °C. Since faster oxidation is required for the desired long-term data storage applications, Co may still be an option. During the local oxidation by laser irradiation, non-linear effects are expected to further increase the oxidation rate constants in the range of orders of magnitude. Another way to increase the reaction rate would be changing the route from oxidation to sulfidation of metal films, *e.g.*, it is known in the literature that the rate of Ni sulfidation is five orders of magnitude higher than that of Ni oxidation at 900 °C. It appears, however, unlikely to fulfill the technological requirements for routine data storage processes. This refers to the speed at which the data can be written; the durability of the data, however, can indeed be very high. As a consequence, oxidation processes of thin Co films applied in the above sense could be suitable for particular purposes.

Appendix

A1-Activation Energies for Conductivity and Chemical Diffusion Coefficient

Activation energies of the conductivity and the chemical diffusion coefficient for the as-prepared and the annealed samples are summarized in Table A1-1. The calculated ΔH^0 from Eq. 34 for Cr-doped samples is around 1.2 eV (average) when the major ionic defect is considered to be V''_{Ni} , and 0.6 eV when the major defect is V'_{Ni} . This is in agreement with the literature results for Cr-doped NiO samples [75, 77], as shown in Table A1-2.

As-prepared samples:

The conductivity activation energy for as-prepared samples (0.60 ± 0.26 eV) in the present work is consistent with the literature values for single crystalline and polycrystalline undoped NiO which is in the range of 0.81 to 1.04 eV [75, 77, 100, 101, 103, 111, 112]. The literature results are summarized and compared to the present results in Table A1-2. There is no significant difference in the activation energy of conductivity between single- and polycrystalline undoped, and Cr-doped NiO samples in the literature.

Also, the present activation energy of the chemical diffusion of 0.6 ± 0.2 eV is in agreement with literature values for polycrystalline samples. It is, however, noteworthy that the literature values scatter strongly (see Table A1-2), *e.g.*, between 0.94 to 1.59 eV for single-crystalline NiO [67, 97, 99-101, 103]. The only available two data for polycrystalline NiO differ as well, while Rom et al. gives 0.7 eV [102], Morlotti reports 1.34 eV [35]. It should

be noted that the density of the sample in Morlotti's study is 92 % and it might have some contribution from open pores [97].

It is shown in literature [4, 47] and in the present work that grain boundaries provide fast diffusion paths for Ni diffusion in NiO (see section 4.1.4.), therefore the oxidation rate constant and the diffusion coefficient are expected to be higher for polycrystalline materials than for single crystalline materials, and for smaller grain size compared to larger grains (see section 4.1.4.). Therefore, the activation energy for chemical diffusion coefficient along grain boundaries is expected to be lower for polycrystalline samples which is in agreement with the literature [102], and the activation energies for the samples in this work.

Annealed samples:

The conductivity activation energies of annealed Cr-doped NiO samples yield of about 0.8 eV. Very few data is available for Cr-doped NiO in literature, with values of 0.87 eV [75] and 0.95eV [77] for polycrystalline samples. The activation energies of the present Cr-doped samples are also consistent with literature for single crystalline [111] and polycrystalline undoped NiO [100, 112].

The activation energy for undoped NiO in this work is much lower which rather corresponds to ΔH_p^m (see Table), the hole migration activation energy, reported in literature as 0.238 eV [111] and 0.253 eV [103]. The very low activation energy of undoped NiO (behaving as acceptor-doped because of K impurities) is consistent with the literature value of 0.234 eV for Li-doped NiO [96].

Table A1-1: Activation energies for chemical diffusion coefficient and conductivity for annealed and as-prepared samples. ΔH^0 values are calculated according to the related formulas in Table 4.5.

	samples	ΔH_{D^δ} (eV)	ΔH_σ (eV)	ΔH^0 (eV) for V''_{Ni}	ΔH^0 (eV) for V'_{Ni}
annealed	Undoped NiO	1.0±0.2	0.23±0.09	-	-
	0.1%Cr-doped NiO	0.8±0.1	0.84±0.08	1.20±0.16	0.60±0.08
	0.3%Cr-doped NiO	1.2±0.2	0.76±0.01	1.04±0.02	0.52±0.01
	1%Cr-doped NiO	1.0±0.1	0.83±0.05	1.18±0.10	0.59±0.05
as-prepared	Undoped NiO	0.6±0.2	0.60±0.26	1.09±0.78	0.72±0.52
	0.1%Cr-doped NiO	0.8±0.4	0.79±0.08	1.10±0.16	0.55±0.08

ΔH_p^m of holes is taken as 0.238 eV from literature [111].

According to the defect model, as summarized in Table 4.5, the activation energy of conductivity should slightly increase by donor doping in NiO relative to undoped NiO. However, for the samples in this work as well as in the literature, this expected difference is not clearly seen and both types of samples show almost the same activation energy [75, 77], as shown in Table A1-1 and Table A2-1. One should note that the expected difference between the activation energy for conductivity of undoped ($\Delta H^0/3 + \Delta H_p^m$) and donor-doped ($\Delta H^0/2 + \Delta H_p^m$) NiO is around 0.2 eV for the case of doubly ionized vacancies are majority defects, if ΔH^0 is around a value of 1.0 eV like in this work. Since the error bar for the activation energy is generally around 0.1 eV in the present work, it is difficult to conclude about a difference of 0.2 eV.

The activation energy of the chemical diffusion coefficient for undoped and acceptor doped NiO is the same as the activation energy of the cation vacancy diffusion coefficient (Table 4.5). For donor doped NiO, the activation energy deviates from the activation energy of cation vacancy diffusion coefficient. This is not unexpected because the temperature-dependent hole concentration also appears in the equation for D^δ (see Table 4.5). Nowotny et. al. [95] studied the Ni chemical diffusion of Cr-doped

NiO for single crystalline samples and reported activation energy values of 1.18 eV (0.1 % Cr), 1.30 eV (0.49 % Cr), 1.37 eV (0.62 % Cr). The present values for annealed Cr-doped NiO samples (1.0 ± 0.2 eV) are in good agreement with the literature. Although the activation energies of undoped and donor doped NiO is expected to be different, there are studies on undoped NiO [67, 99, 103] which show very similar activation energies to Cr-doped NiO in Nowotny 's study [95] and to the results in this work as well.

Table A1-2: Literature summary of activation energy for chemical diffusion coefficient and conductivity of NiO and Cr-doped NiO

reference	year	sample	$\Delta H_{D\delta}$ (eV)	ΔH_{σ} (eV)	ΔH^0 (eV) for V''_{Ni}	ΔH^0 (eV) for V'_{Ni}	n in $\sigma \propto (pO_2)^{1/n}$	temperature range (°C)
[102]	2000	NiO_ polycrystalline	0.70	-			0.16	700-1200
[103]	1979	NiO_ single crystalline	0.97	1.04	2.17*	1.44	0.19 to 0.17	900-1200
[99]	1973	NiO_ single crystalline	0.94	-	-	-	-	900-1200
[95]	1980	0.1 %Cr-doped NiO_ single crystalline	1.18	-	-	-	-	900-1200
[95]	1980	0.49 %Cr-doped NiO_ single crystalline	1.30	-	-	-	-	900-1200
[95]	1980	0.62 % Cr-doped NiO_ single crystalline	1.37	-	-	-	-	900-1200
[67]	1966	NiO_ single crystalline	0.95	-	-	-	-	800-1100
[101]	1978	NiO_ single crystalline	1.59	0.97	2.21	1.47	0.24 to 0.23	1000-1400
[35]	1969	NiO_ polycrystalline	1.34***	-	-	-	-	750-1000
[100]	1973	NiO_ single crystalline	1.46	0.86	1.866	1.244	-	900-1300
[100]	1973	NiO_ polycrystalline	-	0.86	1.866	1.244	0.21 to 0.20	900-1300
[111]	1961	NiO_ single crystalline	-	1.01	2.316	1.544	0.17	600-1350
[112]	1971	NiO_ polycrystalline and single crystalline	-	0.81	1.716	1.144	0.17	900-1400
[75]	1971	NiO_ single crystalline	-	0.90	1.99	1.32	0.17	700-1200
		Cr-doped NiO_ polycrystalline	-	0.87	1.26	0.63	0.25	
[77] **	1973	NiO_ polycrystalline	-	0.95	2.14	1.42	0.17	900-1200
		Cr-doped NiO_ polycrystalline	-	0.95	1.42	0.71	0.25	
[96]	1973	NiO_ single crystalline	-	0.85	1.84	1.23	-	900-1200
		Cr-doped NiO_ single crystalline	-	1.01	1.54	0.77	-	
this work		Cr-doped NiO_ polycrystalline	0.98	0.82	1.16	0.58	0.23 to 0.17	600-800

ΔH_p^m of holes is considered as 0.238 eV from literature [111].

ΔH^0 values are calculated by equations in Table 4.5.

*: The value is given in the reference.

** : The sample has 8-10 μm grain size, which is very similar to present annealed samples.

***: The value is the activation energy of the measured cation vacancy diffusion coefficient.

A2-Effect of Different Annealing Conditions

The grain size control was possible by annealing, and the different microstructures of the samples obtained by annealing at different conditions are illustrated in Figure A2. The effect of different annealing conditions on the samples in terms of conductivity and chemical diffusion coefficient values are presented in Figure A2.

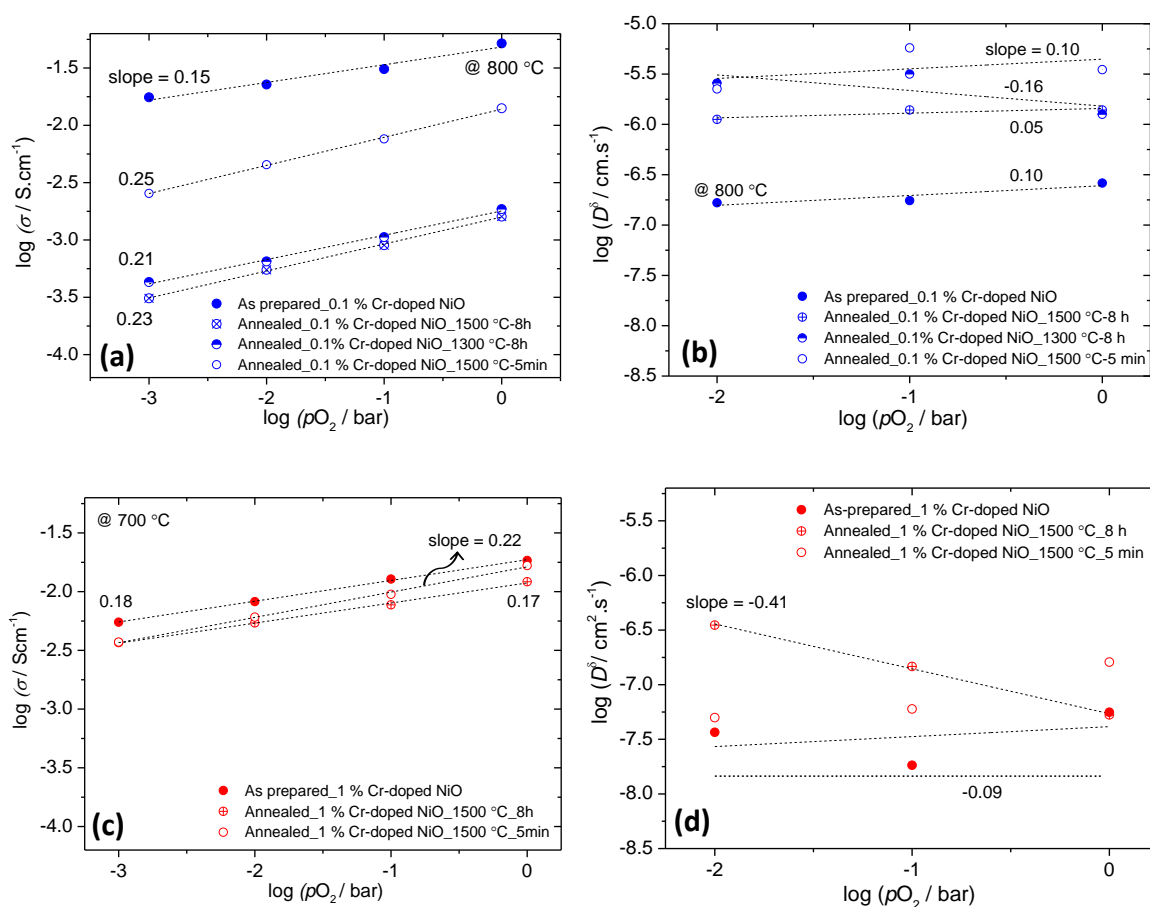


Figure A2: (a) Oxygen partial pressure dependence of conductivity and (b) oxygen partial pressure dependence of chemical diffusion coefficient for 0.1 % Cr-doped NiO, (c) oxygen partial pressure dependence of conductivity and (d) oxygen partial pressure dependence of chemical diffusion coefficient for 1 % Cr-doped NiO as a function of annealing conditions.

Figure A2a shows the pO_2 dependence of conductivity for 0.1 % Cr-doped NiO for different annealing temperatures highlighting the effect of annealing and of grain size on transport. As-prepared, annealed at 1300 °C for 8 hours, annealed at 1500 °C for 5 minutes and annealed at 1500 °C for 8 hours samples (0.1 % Cr-doped NiO) have a grain size of 400 nm, 2-4 μm , 2-4 μm and 4-10 μm , respectively (see Table 3.5).

Figure A2 shows that annealing time is important because the samples that were annealed at 1300 °C and 1500 °C for the same duration (8 hours) show almost the same conductivity and very similar pO_2 dependence. On the other hand, another 0.1 % Cr-doped NiO sample was annealed at 1500 °C for 5 min and it did not show a significant difference in conductivity compared to as-prepared sample. But it showed the same pO_2 dependence as annealed sample although the conductivity value is not same (1500 °C - 8 h). Figure A2b shows all the annealed samples have higher chemical diffusion coefficients than the as-prepared sample which confirms the importance of annealing in terms of activating the dopants. However, all annealed samples reveal pO_2 independent behavior like undoped NiO because of K impurity presence. One has to note that as-prepared samples are not influenced from Cr doping and K impurity (see more details in section 4.3.3.1).

In Figure A2c, the conductivity behavior of 1 % Cr-doped NiO sample is illustrated for the samples treated at different annealing conditions. Although 1 % Cr-doped NiO samples for as-prepared, annealed at 1500 °C for 8 hours and annealed at 1500 °C for 5 minutes reveal very similar conductivity, pO_2 dependence of the annealed sample (1500 °C for 8 hours) ($\sim 1/4.5$) differs to the values of the as-prepared and shortly annealed samples (1500 °C for 5 min) ($\sim 1/6$). This difference indicates that long time annealing activates the dopant since long time annealed sample shows the pO_2 dependence of donor doped NiO ($\sigma_h \propto pO_2^{1/4}$, see Table 4.5) and while the other two samples (as-prepared and shortly annealed) show the pO_2 dependence of undoped NiO. The pO_2 dependence of conductivity and chemical diffusion coefficient are consistent. pO_2 dependence of the chemical diffusion coefficient reveals a negative pO_2 dependence for a long time annealed sample, and a higher chemical diffusion coefficient as expected from donor doping (Figure A2d). As-

prepared and shortly annealed 1 % Cr-doped NiO samples show pO_2 independent chemical diffusion coefficient like undoped NiO since Cr is not active yet as a donor dopant because of inadequate annealing conditions.

Symbols and Abbreviations

List of Most Frequently Used Symbols

- T : temperature
- p_{O_2} : oxygen partial pressure
- h^\bullet : electron holes
- α : ionization degree of a cation
- $V_{Ni}^{\prime\alpha}$: nickel vacancy on a nickel site (singly or doubly ionized)
- O_o^x : oxygen atom on a regular lattice site
- K : mass action constant
- ΔG° : standard molar Gibbs energy
- ΔH° : standard reaction enthalpy
- ΔS° : standard reaction entropy
- k : Boltzmann constant
- [...]: square brackets represent the concentration of the species (molar fraction)
- D_{Ni}^\bullet : donor dopant
- A'_{Ni} : acceptor dopant
- j_i : flux of species
- σ^δ : ambipolar conductivity
- σ_{ion} : ionic conductivity
- σ_{eon} : electronic conductivity
- σ_i : electrical conductivity of species
- F : Faraday constant
- μ_i : chemical potential of species
- c_i : the concentration of charged species
- D_{Ni}^δ : chemical diffusion coefficient of Ni ions in NiO
- $D_{V_{Ni}}''$: diffusion coefficient of Ni vacancies

- z_i : valence number
- u_i : the mobility of species
- ΔH_i^m : activation enthalpy for defect migration
- E_σ : conductivity activation energy
- D_{Ni}^* : tracer diffusion coefficient
- k_p : parabolic rate constant
- X : film thickness
- t : time
- $\Delta\mu_{Me}$: chemical potential difference of the metal
- σ_{Me} : total electronic conductivity
- D_{Me}^* : tracer diffusion coefficient of a metal ion
- D_O^* : tracer diffusion coefficient of an oxygen ion
- \bar{D}_{Me}^* : average tracer diffusion coefficient of metal over an oxide film
- \bar{D}_O^* : average tracer diffusion coefficient of oxygen over an oxide film
- $\Delta H_{D\delta}$: activation energy of chemical diffusion coefficient
- k^δ : effective surface rate constant
- E_a : activation energy
- D_{eff} : the effective diffusion coefficient
- D_{gb} : grain boundary diffusion coefficient
- D_g : grain (bulk) diffusion coefficient

List of Abbreviations

ICP-OES : inductively coupled plasma-optical emission spectroscopy

PLD : pulsed laser deposition

XPS : X-Ray photoelectron spectroscopy

EIS: electrochemical impedance spectroscopy

SPS: spark plasma sintering

SEM: scanning electron microscopy

XRD : X-ray diffraction

TEM : transmission electron microscopy

HR-TEM : high-resolution transmission electron microscopy

EDX : energy dispersive X-ray spectroscopy

FIB: focused ion beam

PBR : Pilling-Bedworth ratio

References

- [1] C. Wagner, Beitrag zur Theorie des Anlaufvorgangs, *Z. Phys. Chem. B*, 21 (1933) 25-41.
- [2] N. Cabrera, N. Mott, Theory of the oxidation of metals, *Reports on Progress in Physics*, 12 (1949) 163-184.
- [3] A. Atkinson, Transport processes during the growth of oxide films at elevated temperature, *Reviews of Modern Physics*, 57 (1985) 437-470.
- [4] N. Halem, M. Abrudeanu, G. Petot-Ervas, Al effect in transport properties of nickel oxide and its relevance to the oxidation of nickel, *Materials Science and Engineering: B*, 176 (2011) 1002-1009.
- [5] M. Tsuchiya, S. K. R. S. Sankaranarayanan, S. Ramanathan, Photon-assisted oxidation and oxide thin film synthesis: A review, *Progress in Materials Science*, 54 (2009) 981-1057.
- [6] W. Smeltzer, D. Young, Oxidation properties of transition metals, *Progress in Solid State Chemistry*, 10 (1975) 17-54.
- [7] R. Haugsrud, On the high-temperature oxidation of Fe, Co, Ni and Cu-based alloys with addition of a less noble element, *Materials Science and Engineering: A*, 298 (2001) 216-226.
- [8] K. R. Lawless, The oxidation of metals, *Reports on Progress in Physics*, 37 (1974) 231.
- [9] A. Galerie, *Shreir's Corrosion: High Temperature Corrosion of Chromia-forming Iron, Nickel and Cobalt-base Alloys*, Elsevier Ltd., Amsterdam, Netherland, 2010.
- [10] M. Graham, M. Cohen, On the mechanism of low-temperature oxidation (23-450 °C) of polycrystalline nickel, *Journal of the Electrochemical Society*, 119 (1972) 879-882.
- [11] F. P. Fehlner, Low temperature oxidation of metals and semiconductors, *Journal of The Electrochemical Society*, 131 (1984) 1645.
- [12] B. M. Lunt, How long is long-term data storage?, *Archiving Conference, Society for Imaging Science and Technology*, 2011, pp. 29-33.
- [13] B. M. Lunt, M. R. Linford, R. Davis, H. Wang, D. Hansen, and J. Dredge, *Permenant digital data storage: A materials approach*, 10th International Conference on Preservation of Digital Objects, Biblioteca Nacional de Portugal, 2013.

- [14] V. Navale, Predicting the life expectancy of modern tape and optical media, RLG DigiNews, 9 (2005).
- [15] S. Manglik, Role of acid-free paper in libraries: A survey, International Journal of Library and Information Science, 6 (2014) 19-21.
- [16] <http://www.delkindevices.com/archival-gold-storage-media/>, accessed on March 2016.
- [17] <http://www.mdisc.com/>, accessed on March 2016.
- [18] <http://www.hitachi.com/New/cnews/120924.html>, accessed on March 2016.
- [19] T. Watanabe, T. Shintani, K. Ono, T. Mine, A digital-data-preservation system featuring LED-light computer tomography, IEICE Electronics Express, 6 (2009) 1569-1575
- [20] R. Imai, M. Shiozawa, T. Shintani, T. Watanabe, S. Mori, Y. Shimotsuma, M. Sakakura, K. Miura, K. Watanabe, 100-Layer recording in fused silica for semi permanent data storage, Japanese Journal of Applied Physics, 54 (2015) 09MC02.
- [21] J. Qiu, K. Miura, K. Hirao, Femtosecond laser-induced microfeatures in glasses and their applications, Journal of Non-Crystalline Solids, 354 (2008) 1100-1111.
- [22] Y. Shimotsuma, K. Hirao, J. Qiu, K. Miura, Nanofabrication in transparent materials with a femtosecond pulse laser, Journal of Non-Crystalline Solids, 352 (2006) 646-656.
- [23] http://www.mdisc.com/wp-content/uploads/2015/08/M-DISC_1sheet_Rock_Like_vF.pdf, accessed on March 2016.
- [24] P. Kofstad, Nonstoichiometry, Diffusion, and Electrical Conductivity in Binary Metal Oxides, Wiley-Interscience, New York, 1972.
- [25] R. Farhi, G. Petot-Ervas, Thermodynamic study of point defects in single crystalline nickel oxide: Analysis of experimental results, Journal of Physics and Chemistry of Solids, 39 (1978) 1175-1179.
- [26] F. Kröger, H. Vink, Relations between the concentrations of imperfections in crystalline solids, Solid State Physics, 3 (1956) 307-435.
- [27] G. Koel, P. Gellings, The contribution of different types of point defects to diffusion in CoO and NiO during oxidation of the metals, Oxidation of Metals, 5 (1972) 185-203.
- [28] J. Maier, Physical Chemistry of Ionic Materials: Ions and Electrons in Solids, John Wiley & Sons, 2004.
- [29] A. S. Khanna, Introduction to High Temperature Oxidation and Corrosion, ASM International, 2002.
- [30] G. Tammann, Über Anlauffarben von Metallen, Zeitschrift für Anorganische und allgemeine Chemie, 111 (1920) 78-89.

- [31] R. Bedworth, N. Pilling, The oxidation of metals at high temperatures, *Journal of the Institute of Metals*, 29 (1923) 529-582.
- [32] H. Schmalzried, *Solid State Reactions*, Vch Pub, 1981.
- [33] H. Schmalzried, *Chemical Kinetics of Solids*, John Wiley & Sons, 2008.
- [34] A. Atkinson, R. Taylor, The diffusion of ^{63}Ni along grain boundaries in nickel oxide, *Philosophical Magazine A*, 43 (1981) 979-998.
- [35] R. Morlotti, Determination of Diffusion Coefficient of Cation Vacancies in Nickel Oxide, *Zeitschrift für Naturforschung A*, 24 (1969) 441-443.
- [36] I. Rastegar, Investigation of titanium thin films for future memory devices, MSc Thesis, University of Stuttgart (2013).
- [37] A. K. Alves, C. P. Bergmann, F. A. Berutti, *Novel Synthesis and Characterization of Nanostructured Materials*, Springer, 2013.
- [38] J. Toniolo, M. Lima, A. Takimi, C. Bergmann, Synthesis of alumina powders by the glycine-nitrate combustion process, *Materials Research Bulletin*, 40 (2005) 561-571.
- [39] L. A. Chick, L. Pederson, G. Maupin, J. Bates, L. Thomas, G. Exarhos, Glycine-nitrate combustion synthesis of oxide ceramic powders, *Materials Letters*, 10 (1990) 6-12.
- [40] C.-C. Hwang, J.-S. Tsai, T.-H. Huang, Combustion synthesis of Ni-Zn ferrite by using glycine and metal nitrates-investigations of precursor homogeneity, product reproducibility, and reaction mechanism, *Materials Chemistry and Physics*, 93 (2005) 330-336.
- [41] F. S. Baumann, Oxygen reduction kinetics on mixed conducting SOFC model cathodes, PhD Thesis, University of Stuttgart (2006).
- [42] E. McCafferty, *Introduction to Corrosion Science*, Springer New York, 2010.
- [43] O. Kubaschewski, B. E. Hopkins, *Oxidation of Metals and Alloys*, Butterworths, 1967.
- [44] G. Samsonov, *The Oxide Handbook*, IET, Plenum, New York/London, 1973.
- [45] J. Lian, Q. Dong, Z. Guo, Q. Xu, J. Yang, J. Hu, Q. Guan, B. Chen, Surface oxidation kinetics of Cr film by Nd-YAG laser, *Materials Science and Engineering: A*, 391 (2005) 210-220.
- [46] L. Nánai, R. Vajtai, T. F. George, Laser-induced oxidation of metals: state of the art, *Thin Solid Films*, 298 (1997) 160-164.
- [47] A. Atkinson, D. Smart, Transport of nickel and oxygen during the oxidation of nickel and dilute nickel/chromium alloy, *Journal of the Electrochemical Society*, 135 (1988) 2886-2893.

- [48] D. J. Young, High Temperature Oxidation and Corrosion of Metals: Oxidation of Pure Metals, 1 (2008) 81-137.
- [49] R. Haugsrud, On the high-temperature oxidation of nickel, Corrosion Science, 45 (2003) 211-235.
- [50] L. Courtade, C. Turquat, C. Muller, J.G. Lisoni, L. Goux, D.J. Wouters, D. Goguenheim, P. Roussel, L. Ortega, Oxidation kinetics of Ni metallic films: Formation of NiO-based resistive switching structures, Thin Solid Films, 516 (2008) 4083-4092.
- [51] A. Atkinson, D. Smart, R. Taylor, Grain boundary diffusion in Cr-doped NiO and the oxidation of Ni-Cr alloy, Materials and Corrosion, 38 (1987) 704-709.
- [52] A. Atkinson, R. Taylor, The self-diffusion of Ni in NiO and its relevance to the oxidation of Ni, Journal of Materials Science, 13 (1978) 427-432.
- [53] F. Gesmundo, F. Viani, The parabolic rate constant for the high-temperature oxidation of pure or slightly alloyed nickel and the defect structure of nickel oxide, Solid State Ionics, 6 (1982) 33-42.
- [54] S. Mrowec, Z. Grzesik, Oxidation of nickel and transport properties of nickel oxide, Journal of Physics and Chemistry of Solids, 65 (2004) 1651-1657.
- [55] S. Chevalier, F. Desserrey, J. P. Larpin, Oxygen transport during the high temperature oxidation of pure nickel, Oxidation of Metals, 64 (2005) 219-234.
- [56] F. Stott, G. Wood, D. Whittle, B. Bastow, Y. Shida, A. Martinez-Villafane, The transport of oxygen to the advancing internal oxide front during internal oxidation of nickel-base alloys at high temperature, Solid State Ionics, 12 (1984) 365-374.
- [57] K. Fueki, J. B. Wagner, Studies of the oxidation of nickel in the temperature range of 900 to 1400 °C, Journal of the Electrochemical Society, 112 (1965) 384-388.
- [58] A. Hughes, A. Atkinson, A. Chadwick, Short-circuit diffusion processes in oxidation films, MRS Proceedings, Cambridge Univ Press, 1983, pp. 27.
- [59] A. Atkinson, R. Taylor, A. Hughes, A quantitative demonstration of the grain boundary diffusion mechanism for the oxidation of metals, Philosophical Magazine A, 45 (1982) 823-833.
- [60] S. Song, P. Xiao, Electrical properties of the oxide film formed on nickel during high-temperature oxidation, Materials Science and Engineering: A, 323 (2002) 27-31.
- [61] S. Mrowec, Z. Grzesik, B. Rajchel, A. Gil, J. Dabek, The influence of aliovalent impurities on the oxidation kinetics of nickel at high temperatures, Journal of Physics and Chemistry of Solids, 66 (2005) 115-120.

- [62] S. Mrowec, K. Przybylski, Transport properties of sulfide scales and sulfidation of metals and alloys, *Oxidation of Metals*, 23 (1985) 107-139.
- [63] D. Caplan, M. Graham, M. Cohen, Effect of cold work on the oxidation of nickel at high temperature, *Journal of the Electrochemical Society*, 119 (1972) 1205-1215.
- [64] N. Khoi, W. Smeltzer, J. Embury, Growth and structure of nickel oxide on nickel crystal faces, *Journal of the Electrochemical Society*, 122 (1975) 1495-1503.
- [65] C. Dubois, C. Monty, J. Philibert, Oxygen self-diffusion in NiO single crystals, *philosophical magazine A*, 46 (1982) 419-433.
- [66] R. Nakamura, J.-G. Lee, H. Mori, H. Nakajima, Oxidation behaviour of Ni nanoparticles and formation process of hollow NiO, *Philosophical Magazine*, 88 (2008) 257-264.
- [67] J. Price, J. Wagner, Determination of the chemical diffusion coefficients in single crystals of CoO and NiO, *Zeitschrift für Physikalische Chemie*, 49 (1966) 257-270.
- [68] A. Atkinson, R. I. Taylor, The diffusion of Ni in the bulk and along dislocations in NiO single crystals, *Philosophical Magazine A*, 39 (1979) 581-595.
- [69] E. Hart, On the role of dislocations in bulk diffusion, *Acta Metallurgica*, 5 (1957) 597.
- [70] H. Mehrer, *Diffusion in Solids: Fundamentals, Methods, Materials, Diffusion-Controlled Processes*, Springer Science & Business Media, 2007.
- [71] H. Atkinson, A review of the role of short-circuit diffusion in the oxidation of nickel, chromium, and nickel-chromium alloys, *Oxidation of Metals*, 24 (1985) 177-197.
- [72] A. Atkinson, J. Corish, *Corrosion: Mass Transport in Solids*, Springer, 1983, pp. 477-504.
- [73] F. Stott, G. Wood, The mechanism of oxidation of dilute Ni-Al alloys at 800-1200 °C, *Corrosion Science*, 17 (1977) 647-670.
- [74] G. Petot-Ervas, C. Petot, The influence of impurities segregation phenomena on the oxido-reduction kinetics of oxides, *Journal of Physics and Chemistry of Solids*, 51 (1990) 901-906.
- [75] H. Meier, R. Rapp, Electrical conductivities of pure NiO and chromium-doped NiO, *Zeitschrift für Physikalische Chemie*, 54 (1971) 168-189.
- [76] C. H. Chen, M. R. Notis, D. B. Williams, Precipitation and solid solubility in the system NiO-Cr₂O₃, *Journal of the American Ceramic Society*, 66 (1983) 566-571.

- [77] S. Mrowec, J. Nowotny, T. Walec, T. Wojcikiewicz,, Electrical conductivity of chromium doped nickel-oxide, *Bulletin de L'Academie Polonaise des Sciences-Serie des Sciences Chimiques*, 21 (1973) 829-837.
- [78] W. Chen, N. Peterson, L. Robinson, Chromium tracer diffusion in NiO crystals, *Journal of Physics and Chemistry of Solids*, 34 (1973) 705-709.
- [79] M. Seltzer, Diffusion of ^{51}Cr in NiO single crystals, *Journal of The Electrochemical Society*, 118 (1971) 802-805.
- [80] A. Atkinson, R. Taylor, Impurity diffusion in NiO grain boundaries, *Journal of Physics and Chemistry of Solids*, 47 (1986) 315-323.
- [81] H. Bouwmeester, H. Kruidhof, A. Burggraaf, Importance of the surface exchange kinetics as rate limiting step in oxygen permeation through mixed-conducting oxides, *Solid State Ionics*, 72 (1994) 185-194.
- [82] J. Claus, M. Leonhardt, J. Maier, Tracer diffusion and chemical diffusion of oxygen in acceptor doped SrTiO_3 , *Journal of Physics and Chemistry of Solids*, 61 (2000) 1199-1207.
- [83] R. De Souza, J. Kilner, Oxygen transport in $\text{La}_{1-x}\text{Sr}_x\text{Mn}_{1-y}\text{Co}_y\text{O}_{3\pm\delta}$ perovskites: Part I. Oxygen tracer diffusion, *Solid State Ionics*, 106 (1998) 175-187.
- [84] P. Gibot, L. Vidal, Original synthesis of chromium (III) oxide nanoparticles, *Journal of the European Ceramic Society*, 30 (2010) 911-915.
- [85] B. D. Hosterman, Raman spectroscopic study of solid solution spinel oxides, PhD Thesis, University of Nevada (2011).
- [86] R. Cairns, E. Ott, X-ray studies of the system nickel-oxygen-water. I. Nickelous oxide and hydroxide, *Journal of the American Chemical Society*, 55 (1933) 527-533.
- [87] H. Rooksby, Structure of nickel oxide, *Nature*, 152 (1943) 304.
- [88] W. Roth, Magnetic structures of MnO, FeO, CoO, and NiO, *Physical Review*, 110 (1958) 1333.
- [89] H. Rooksby, A note on the structure of nickel oxide at subnormal and elevated temperatures, *Acta Crystallographica*, 1 (1948) 226-226.
- [90] T. Yamada, Magnetic Anisotropy, Magnetostriction, and magnetic domain walls in NiO. I. Theory, *Journal of the Physical Society of Japan*, 21 (1966) 664-671.
- [91] K. Nakahigashi, N. Fukuoka, Y. Shimomura, Crystal structure of antiferromagnetic NiO determined by X-ray topography, *Journal of the Physical Society of Japan*, 38 (1975) 1634-1640.

- [92] Z. Jarzebski, S. Mrowec, Defect structure model for nickel oxide, *Oxidation of Metals*, 1 (1969) 267-277.
- [93] A. Stokłosa, Point defect diagrams for pure and doped nickel oxide $\text{Ni}_{1-\delta}\text{O}$ in the temperature range of 1,173–1,673 K (II), *Ionics*, 17(3), (2011) 271-285.
- [94] J. Nowotny, M. Rękas, Seebeck effect of undoped and Cr-doped NiO, *Solid State Ionics*, 12 (1984) 253-261.
- [95] J. Nowotny, J. Obłakowski, A. Sadowski, J. Wagner Jr, Reequilibrium kinetics of NiO-Cr₂O₃ solid solutions, *Oxidation of Metals*, 14 (1980) 437-448.
- [96] J. Nowotny, J. Wagner, Electrical conductivity of undoped, lithium and chromium doped nickel-oxide single crystals, *Bulletin de L'Academie Polonaise des Sciences-Serie des Sciences Chimiques*, 21 (1973) 931-936.
- [97] Y. Ikeda, K. Nii, Cation vacancy diffusion coefficient in NiO, *Transactions of the Japan Institute of Metals*, 17 (1976) 419-425.
- [98] J. Nowotny, T. Bak, M. K. Nowotny, L. R. Sheppard, Chemical diffusion in metal oxides. Example of TiO₂, *Ionics*, 12 (2006) 227-243.
- [99] J. Nowotny, J. Wagner, Reequilibration kinetics for undoped and lithium-doped single crystal nickel oxide, *Journal of the American Ceramic Society*, 56 (1973) 397-398.
- [100] J. Dereń, S. Mrowec, Semiconducting and transport properties of mono-and polycrystalline nickel oxide, *Journal of Materials Science*, 8 (1973) 545-558.
- [101] R. Farhi, G. Petot-Ervas, Electrical conductivity and chemical diffusion coefficient measurements in single crystalline nickel oxide at high temperatures, *Journal of Physics and Chemistry of Solids*, 39 (1978) 1169-1173.
- [102] I. Rom, W. Jantscher, W. Sitte, Conductivity relaxation experiments on $\text{Ni}_{1-\delta}\text{O}$, *Solid State Ionics*, 135 (2000) 731-736.
- [103] J. Nowotny, A. Sadowski, Chemical diffusion in nickel oxide, *Journal of the American Ceramic Society*, 62 (1979) 24-28.
- [104] J. G. Grasselli, M. K. Snavely, B. J. Bulkin, *Chemical Applications of Raman Spectroscopy*, John Wiley & Sons Inc, 1981.
- [105] J. R. Ferraro, *Introductory Raman Spectroscopy*, Academic Press, 2003.
- [106] N. Mironova-Ulmane, A. Kuzmin, I. Steins, J. Grabis, I. Sildos, M. Pärs, Raman scattering in nanosized nickel oxide NiO, *Journal of Physics: Conference Series*, IOP Publishing, 2007, pp. 012039.

- [107] Z. Wang, S. Saxena, P. Lazor, H. O'Neill, An in situ Raman spectroscopic study of pressure induced dissociation of spinel NiCr_2O_4 , *Journal of Physics and Chemistry of Solids*, 64 (2003) 425-431.
- [108] N. Mironova-Ulmane, A. Kuzmin, I. Sildos, M. Pärs, Polarisation dependent Raman study of single-crystal nickel oxide, *Central European Journal of Physics*, 9 (2011) 1096-1099.
- [109] C. Greskovich, Kinetics of NiCr_2O_4 formation and diffusion of Cr^{3+} ions in NiO, *Journal of The American Ceramic Society*, 53 (1970) 498-502.
- [110] R. A. Perkins, R. A. Rapp, The concentration-dependent diffusion of chromium in nickel oxide, *Metallurgical Transactions*, 4 (1973) 193-205.
- [111] S. P. Mitoff, Electrical conductivity and thermodynamic equilibrium in nickel oxide, *The Journal of Chemical Physics*, 35 (1961) 882.
- [112] C. Osburn, R. Vest, Defect structure and electrical properties of NiO: I. High temperature, *Journal of Physics and Chemistry of Solids*, 32 (1971) 1331-1342.

Acknowledgements

First of all, I would like to express my deep gratitude to Prof. Joachim Maier and Prof. Jochen Mannhart for giving me the possibility to work between two excellent departments in a supportive environment. I deeply appreciate the time devoted to valuable discussions and many important pieces of advice that have helped me to improve my research. They encouraged and supported me during my research, it was a privilege for me to work with them.

I acknowledge Prof. Anke Weidenkaff and Prof. Rainer Niewa for accepting being part of my PhD exam committee and for reviewing my thesis.

During my PhD, I was very lucky to have the chance to work with Dr. Rotraut Merkle as my daily advisor. This thesis, in its present form, has tremendously benefited from her input and from many scientific discussions that we have had. I have learned a lot from her, she had always time to discuss and to answer my questions. I am deeply thankful for her great contribution not only to my research but also to my understanding of many difficult scientific concepts.

I would like to thank Dr. Giuliano Gregori for useful scientific discussions, for helping me preparing some samples, encouraging me in my research and being a very good friend. I acknowledge Iman Rastegar for his help in the lab when I arrived, for sharing his knowledge and for our discussions. I would like to express my deep gratitude to Dr. Jone Zabaleta for reading some parts of my thesis and for valuable suggestions. Special thanks go to Evangelos Fillis-Tsirakis for reading some parts of my thesis and to Lukas Kürten for writing the Zusammenfassung.

I sincerely appreciate all the people who made a contribution to this work. I would like to thank: Yvonne Stuhlhofer for preparing more than 150 thin films, Gabi Götz and Dr. Helga Hoier for XRD measurements, Dr. Mitsuharu Konuma for XPS measurements and for helpful discussions, Bernard Fenk for FIB sample preparation, Kersten Hahn for TEM analysis, Marion Kelsch for TEM sample preparation and analysis, Dr. Fritz Phillipp and

Dr. Wilfred Sigle for TEM/EDX analysis and for discussions, Armin Schulz for Raman analysis, Dr. Dieter Fischer for PLD grown samples, Barbara Baum for sample cut, Reinhart Völker for magnetron sputtered films, Samir Hammoud and Gerhard Werner for ICP-OES measurements, Oliver Gerbig for helping me to use ozone generator, Michael Weissmayer for SPS pellet preparation, Dr. Matej Fonovic for helping me to prepare an alloy, and Maritta Dudek for thin film XRD measurement. A special thank goes to members of Glass Workshop for their kind help and Nanostructuring Lab for the facilities.

Renate Zimmermann and Sofia Weiglein are acknowledged for administrative support and their kindness towards me. I would like to thank Dr. Hans-Georg Libuda for his valuable help to get started in Stuttgart and in IMPRS. Furthermore, I would like to thank Birgit King for handling all my visa procedure and for saving me a lot of time.

All my colleagues in both departments, all the technicians especially Udo Klock, Uwe Traub, Peter Senk and all the scientists are acknowledged for their kind help and for providing a friendly environment.

I thank Scientific and Technological Research Council of Turkey (TUBITAK) for supporting me with Bideb Scholarship Programme during my graduate studies.

My dear officemates (former and current), Konrad, Cyril, Angelos, Lukas and Ali, thanks to all of you for happy mornings, coffee breaks, and our latest tradition “*office wine*”. Many thanks to my dear friends in Stuttgart and The Turkish Mafia at MPI-Stuttgart for all the nice moments we shared together and for the friendship.

I want to thank the Mediterranean club: Jone, Cyril, Angelos, Marco, and Jelena. I enjoyed, laughed, and experienced a lot with you. You made my life easy and joyful in Stuttgart. The distances were not a barrier to keep in touch and share the life with my friends at home and around the world, Feyza, Sinem, Elif, Alperen, Seda, Yusuf and Sevcan. I am very lucky to have you in my life.

I am indebted to my parents, my sisters, and my husband. I dedicate this work to them because it would have been impossible without their constant support, love, and patience. I do not have enough words to express my gratitude to my parents and to my husband Burak.

Curriculum vitae

Name: Yeliz Unutulmazsoy

Date/place of birth: 01.09.1985/Susehri, Turkey

June 2012 – June 2016

Ph.D. in Chemistry

Max Planck Institute for Solid State Research & University of Stuttgart, Stuttgart, Germany

Department of Physical Chemistry of Solids (Prof. Dr. Joachim Maier)

Department of Solid State Quantum Electronics (Prof. Dr. Jochen Mannhart)

Thesis: “*Oxidation kinetics of metal films and diffusion in NiO for data storage.*”

Aug. 2010 – May 2012

Senior R&D Engineer

Kalekim Construction Chemicals
Kale Group, Istanbul, Turkey

Sept. 2009 - Jan. 2011

M.Sc. in Materials Science & Engineering

Istanbul Technical University, Istanbul, Turkey

Thesis: “*Interfacial thermochemistry between LSGM-BSCF and LSGM-SCF in solid oxide fuel cells.*”

Sept. 2008 – Aug. 2010

Research & Teaching Assistant

Sabanci University, Materials Science & Engineering Department, Istanbul, Turkey

Assisted Courses: *Nature of Science, Materials Science*

Sept. 2003 – June 2008

B.Sc. in Materials Science & Engineering

Gebze Technical University, Kocaeli, Turkey